FIRST-PRINCIPLE STUDY ON THE INTERACTION OF LIGANDS WITH GOLD AND EFFECTS ON CATALYTIC ACTIVITIES

A Dissertation

Submitted to the Graduate Faculty of the
Louisiana State University and
Agricultural and Mechanical College
in partial fulfillment of the
requirements for the degree of
Doctor of Philosophy

in

The Department of Chemical Engineering

by
Xun Cheng
B.S., Nankai University, 2012
M.S., Carnegie Mellon University, 2013
May 2020

DEDICATED TO MY PARENTS

Acknowledgements

I would like to express my sincere gratitude to my supervisor, Dr. Ye Xu, for providing me an invaluable opportunity to do research using theoretical methods. I have gained a vast knowledge of surface science and theoretical methodology from him. He offered clear guidance on my research work and presentations with tremendous enthusiasm and patience. He always thoroughly checked my complicated models and calculations. He encouraged me to attend various academic meetings and shared his experiences in meetings with me. I would also like to thank him for caring about my life in addition to professional duties. It is a great honor for me to work and study in his group.

I am grateful to our collaboration scientists from Dr. John C. Flake, Dr. Zhangquan Peng and Dr. Vladimir Matolin research groups, for their innovative and outstanding experimental works. They provided helpful suggestions on constructing reliable theoretical models and reaction mechanisms.

I am also grateful to the wonderful Committee members, Dr. Ye Xu, Dr. John C. Flake, Dr. Bin Chen, Dr. Matthew Chambers, and Dr. Yuanhang Chen, for their continued support which held me to overcome difficulties, and their excellent suggestions on my research work.

I thank my friends from Dr. Ye Xu's research group, Dr. William C. Mckee, Dr. Chuanlin Zhao, Kushal Ghale, Saurin H. Rawal, Suman B. Ranganath, Dr. Shengjie Zhang, and Md. S. Rahman, for their constant camaraderie and assistance.

I am extending my thanks to the faculty and staff from Louisiana State University, the doctors from Louisiana, and my friends and relatives, for offering help and advice to me throughout my study at Louisiana State University.

Finally, I would especially like to thank my parents for raising me to be the man I am. They provide unconditional love to me and encourage me to pursue my interests. I am extremely grateful to be their child.

Table of Contents

Nomenclature, Symbols, Acronyms

DFT	density functional theory
CO_2RR	CO_2 reduction reaction
2-PET	2-phenylethanethiol
2-MPA	2-mercaptopropionic acid
HER	hydrogen evolution reaction
SHE	standard hydrogen electrode
NHE	normal hydrogen electrode
RHE	reversible hydrogen electrode
CV	cyclic voltammetry
SEM	scanning electron microscope
TEM	transmission electron microscope
XPS	X-ray photoelectron spectroscopy
SAM	self assembled monolayer
STM	scanning tunneling microscope
ML	monolayer
SCE	saturated calomel electrode
GGA	generalized gradient approximation
RPBE	revised Perdew-Burke-Ernzerhof
PAW	projector augmented wave
ZPE	zero point energy
DSBD	disulfanediyldibenzenediazonium
SERS	surface-enhanced Raman spectroscopy
NEXAFS	near edge X-ray absorption fine structure
ATR-IR	attenuated total reflectance infrared
FE	faradaic efficiency

Abstract

The extensive use of fossil fuels has increased the atmospheric concentration of CO_2, resulting in global climate change. One way to mitigate the CO_2 challenge is to convert it into useful chemicals electrocatalytically using renewable energies. Recent studies suggest that ligand-modified gold electrodes can enhance the Faradaic efficiency (FE) and selectivity of the electrochemical CO_2 reduction reaction (CO_2RR). This theoretical research, primarily based on density functional theory (DFT), has been carried out to understand the interactions of ligands with Au and possible effects on electrocatalytic activities. We systematically modeled and studied the adsorption of three different types of ligands, which bond through C, N, and S respectively, on Au surfaces in conjunction with various experimental techniques to clarify how the type of ligand, bonding site on Au surfaces, and many environmental factors such as electrode potential and aqueous solution influence the strength of the interaction. In addition, we theoretically investigated the enhancement of catalytic activity of Au electrode induced by the interaction between thiol ligands and Au electrode. We demonstrated that thiol ligands, such as 2-phenylethanethiol (2-PET) and 2-mercaptopropionic acid (2-MPA), modified Au electrodes by reconstructing the electrode surfaces to generate active Au defect sites, which promoted CO and hydrogen evolution reactions (HER). Our studies provide strong theoretical evidence for future research on the synthesis of novel ligand-Au catalysts.

Chapter 1. Introduction

1.1. Excessive atmospheric CO_2 concentration induced climate change

The concentration of CO_2 in the atmosphere exceeded 400 parts per million (ppm) in 2018 according to the National Oceanic and Atmospheric Administration (NOAA).[1] The increase of the atmospheric CO_2 concentration in the past two centuries was due to the continued combustion of fossil fuels for energy.[2] Researchers from the Intergovernmental Panel on Climate Change (IPCC) reported that the safe upper atmospheric CO_2 concentration is 350 ppm.[3] The excessive CO_2 molecules in the atmosphere caused global warming and ocean acidification. The earth emitted heat rays (longwave radiation) are adsorbed by CO_2 molecules in the atmosphere, and the adsorption of heat rays heats the atmosphere which in turn re-radiate longwave radiation back to the surface of the earth, leading to the phenomenon of global warming.[4] The adsorbed CO_2 in the ocean reacts with water molecules to produce hydrogen ion (H^+) and bicarbonate (HCO_3^-), making the ocean more acidic.[5] Thus, scientists have developed various methods to reduce the CO_2 concentration in the atmosphere, such as photoreduction of CO_2 and electrochemical CO_2RR. We focused on the electrochemical CO_2RR in our research works.

1.2. Electroreduction of CO_2

Electrochemical CO_2RR reduces CO_2 to various chemicals and fuels in aqueous solutions under ambient conditions.[6, 7] The electricity needed for electrochemical CO_2RR can be generated from renewable sources, such as wind, water, and the sun.[3] In the simplest setup, electrochemical CO_2RR is conducted on two electrodes separated with a membrane (**Figure 1.1**).[8] H_2O is oxidized to molecular oxygen on the anode, and CO_2 is reduced by electrons on the cathode.[8] The reaction rate of electrochemical CO_2RR can be easily tuned by changing the potential of

electrode.[8] The activity of electrochemical CO_2RR is controlled by catalyst's electronic structure, catalyst nano-structuring, mass transport, the interfacial electric field, pH, and the electrolyte composition.[9] The modularity and scale-up of electrochemical CO_2RR are relative simple.[10]

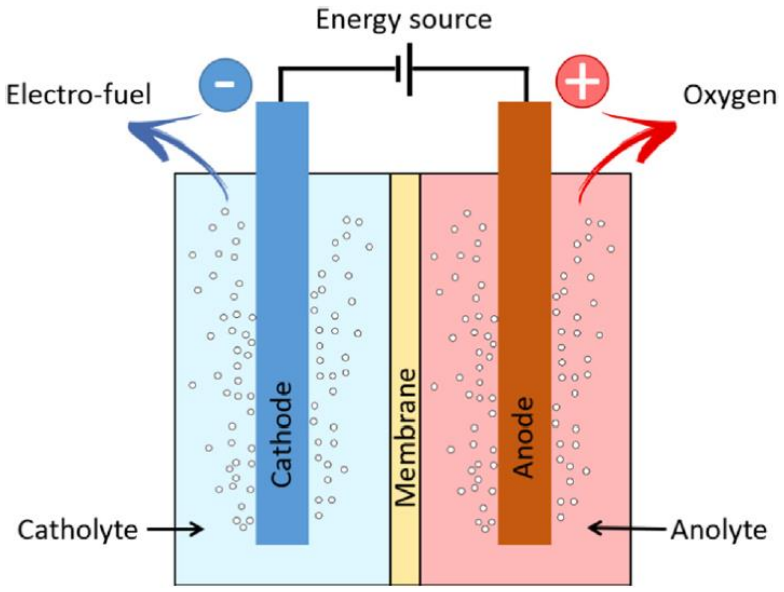

Figure 1.1. Schematic of a typical electrolyzer for electrochemical CO_2RR. Reprinted with permission from Q. Lu and F. Jiao, *Nano Energy* 2016, 29, 439-456. © 2016 Elsevier.

The one-electron reduction of CO_2 to surface-bounded CO_2^{-} at -1.90 V vs. standard hydrogen electrode (SHE) is thermodynamically unfavorable.[8] CO_2 can be reduced to various products, such as HCOOH, CO and HCHO, in pH = 7 aqueous solutions at the potential range of -0.20 to -0.61 V vs. SHE (**Table 1.1**).[8] The selectivity of electrochemical CO_2RRs is usually low because the reduction potentials of CO_2RRs are in a small potential range of 0.4 V, where the HER is a competing reaction. As a result, large amounts of H_2 are generated on electrode in electrochemical CO_2RRs, which suppresses the FE of desirable products of hydrocarbons.

Table 1.1. Possible electrochemical reduction reactions of CO_2 with their standard potentials. Reprinted with permission from Q. Lu and F. Jiao, *Nano Energy*, 2016, 29, 439-456. © 2016 Elsevier.

Reaction	*E* (V) *vs.* SHE
$2H^+ + 2e^- \rightarrow H_2$	−0.41
$CO_2 + 2H^+ + 2e^- \rightarrow HCOOH$	−0.61
$CO_2 + 2H^+ + 2e^- \rightarrow CO + H_2O$	−0.53
$CO_2 + 4H^+ + 4e^- \rightarrow C + 2H_2O$	−0.20
$CO_2 + 4H^+ + 4e^- \rightarrow HCHO + H_2O$	−0.48
$CO_2 + 6H^+ + 6e^- \rightarrow CH_3OH + H_2O$	−0.38
$CO_2 + 8H^+ + 8e^- \rightarrow CH_4 + 2H_2O$	−0.24

In 1985, Hori and co-workers first investigated CO_2RR using bulk metal electrodes, and obtained products of $HCOO^-$, CH_4, CO and H_2.[11] Cd, Sn, Pb and Zn electrodes produced $HCOO^-$ and H_2. In electrode produced $HCOO^-$ selectively at a FE more than 92%, and gave byproducts of CO and H_2. The reproducibility of Zn was poor, the FE of $HCOO^-$ was in the range of 17.6% to 85.0%, whereas the FE of CO was in the range of 63.3% to 3.3%. Cu produced a significant amount of CH_4. Ag and Au predominantly produced CO. H_2 was the exclusive product on Ni and Fe.[11] Formate and CO are the two main products on metal electrodes. The FE and current density of these two products on various metal electrodes are shown in **Table 1.2** and **1.3**.[6]

Table 1.2. The formation of formate on metal electrodes in aqueous solutions. Adapted with permission from J.-P. Jones, G. K. S. Prakash and G. A. Olah, *Isr. J. Chem.* 2014, 54, 1451-1466. © 2014 John Wiley and Sons.

Entry	Electrode	E vs. SHE (V)	$HCOO^-$ FE (%)	Current Density ($mA\,cm^{-2}$)	Electrolyte
1	Pb	−2.76	97	115	0.35 M Na_2SO_4, H_2SO_4, pH 2.0
2	Pb	−1.63	97.4	5.0	0.1 M $KHCO_3$
3	Hg	−1.51	99.5	0.5	0.1 M $KHCO_3$
4	In	−1.55	94.9	5.0	0.1 M $KHCO_3$
5	Sn	−1.48	88.4	5.0	0.1 M $KHCO_3$
6	Cd	−1.63	78.4	5.0	0.1 M $KHCO_3$
7	Tl	−1.60	95.1	5.0	0.1 M $KHCO_3$
8	Pb	−1.56	39	0.5	0.2 M K_2CO_3 Fixed Bed
9	Pb	−1.59	90	2.5	0.5 M NaOH
10	Pb	−1.64	49	10	0.5 M NaOH
11	Sn	−1.60	70	27	0.5 M $NaHCO_3$
12	Sn	−1.76	63.5	26.7	0.5 M $KHCO_3$

Table 1.3. The formation of CO on metal electrodes in aqueous solutions. Adapted with permission from J.-P. Jones, G. K. S. Prakash and G. A. Olah, *Isr. J. Chem.* 2014, 54, 1451-1466. © 2014 John Wiley and Sons.

Entry	Electrode	E vs. SHE (V)	CO FE (%)	Current Density ($mA\,cm^{-2}$)	Electrolyte
1	Au	−1.5	50	20	0.5 M $KHCO_3$
2	Au	−1.10	80	7	0.1 M $KHCO_3$
3	Ag	−1.3	92.3	20	0.2 M K_2SO_4
4	Ag	−1.46	64.6	50	0.2 M K_2SO_4
5	Ag	−2.96	52.7	100	0.2 M K_2SO_4
6	Ag	−1.46	60	50	0.5 M $KHCO_3$
7	Ag	−1.56	30	50	0.5 M $KHCO_3$
8	Au	−1.91	33	100	0.5 M $KHCO_3$
9	Au/C	−2.22	64	200	0.5 M $KHCO_3$
10	Au NP	−0.4	98	6	0.5 M $KHCO_3$
11	Ag NP	−0.6	92	18	0.5 M $KHCO_3$
12	ACF/Ni[a]	−1.56	30.3	47	0.5 M $KHCO_3$
13	40 wt% Ag/TiO_2	−1.6	90	100	1 M KOH

The proposed mechanisms of electrochemical CO_2RR on metal electrodes are shown in **Figure 1.2**. The reduction of CO_2 to CO_2^- is the rate limiting step. The surface-bounded CO_2^- is reduced to CO, whereas the CO_2^- in solution is reduced to $HCOO^-$. The metal electrodes can be divided into three groups based on their abilities to bind CO_2^- and whether they can reduce CO. The metals in Group 1 can not bind CO_2^- and reduce CO. The metals in group 2 bind CO_2^-, but can not reduce CO. The Cu electrode can binds CO_2^- and reduce CO.[6]

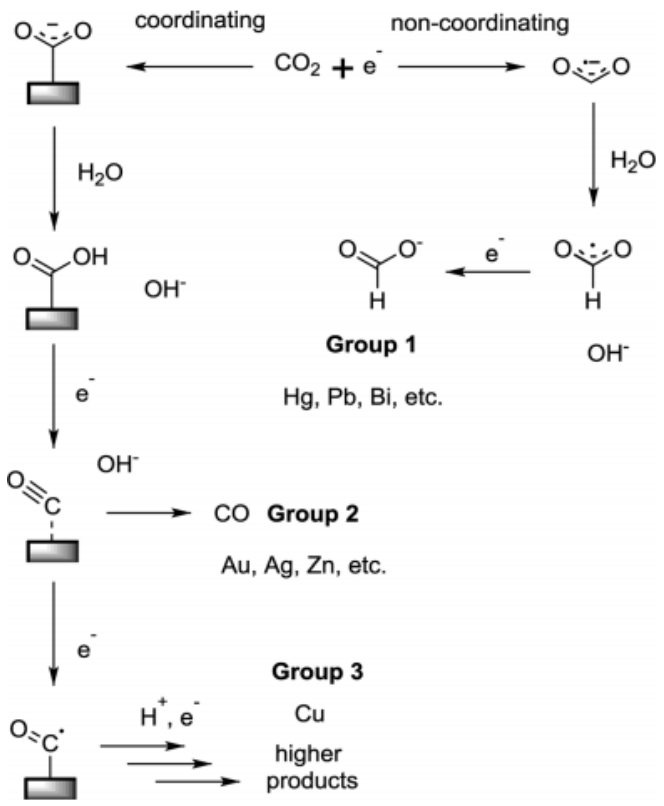

Figure 1.2. Mechanisms of electrochemical CO_2RR on metal electrodes in aqueous solutions. Reprinted with permission from J.-P. Jones, G. K. S. Prakash and G. A. Olah, *Isr. J. Chem.* 2014, 54, 1451-1466. © 2014 John Wiley and Sons.

Kuhl et al. investigated the electrocatalytic behaviors on transition metal electrodes using both experimental and computational methods (**Figure 1.3**).[12] The vertical line in **Figure 1.3** indicates the CO binding energy of reaction $CO^* = CO_{(g)} + *$, where * denotes a free site on surfaces.[13] The metals that favor adsorbed CO lie on the left side of the vertical line, whereas the metals that favor CO in gas phase lie on the right side of the vertical line.[12] Au produces CO gas in electrochemical CO_2RRs at a high current density and low overpotential. We focused on the study of Au electrodes in our research.

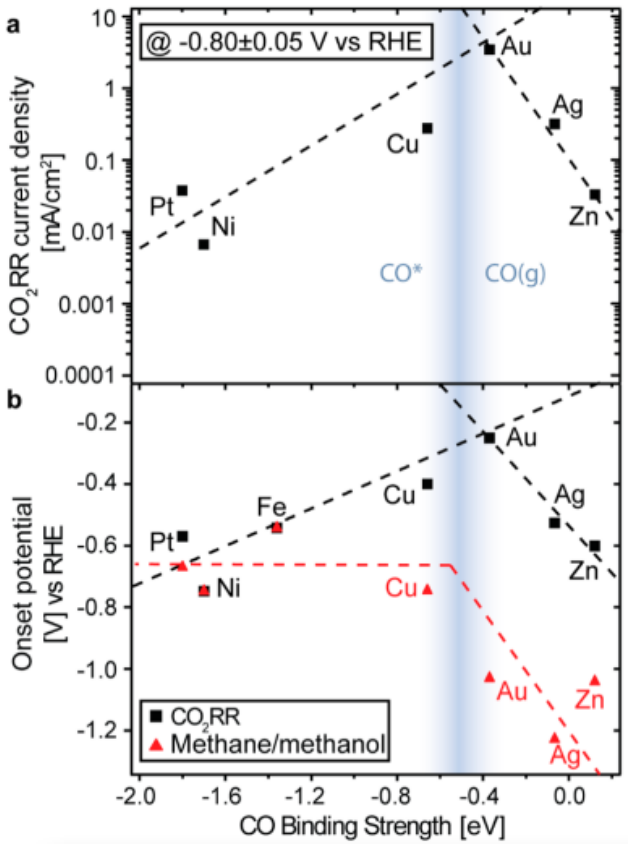

Figure 1.3. (a) Volcano plot of CO_2RR current density vs. CO binding energy at −0.8 V vs. RHE. (b) Volcano plot of onset potential vs CO binding energy. Reprinted with permission from K. P. Kuhl, T. Hatsukade, E. R. Cave, D. N. Abram, J. Kibsgaard and T. F. Jaramillo, *J. Am. Chem. Soc.* 2014, 136, 14107-14113. © 2014 American Chemical Society.

In the literature, the FE of CO evolution was found to be 91% on an Au electrode in a 0.5 M $KHCO_3$ solution at -1.1 V vs. normal hydrogen electrode (NHE). The partial current density and onset potential of the CO evolution are 3.7 mA cm^{-2} and -0.8 V vs. SHE, respectively.[11, 14, 15] The pH of phosphate buffer solution has a significant effect on the FE and current density of the CO evolution on Au electrode. The FE increased from 30% to 60% as the pH of the solution increased from 2.5 to 6.8 at -1.3 V vs. Ag/AgCl.[16] The current density of CO was dependent on the pH of the solutions in pH = 6.2 or 6.8 solution, whereas the current density of CO was not dependent on the pH of the solutions in pH = 2.5, 4.3 or 5.2 solution.[16]

To improve the catalytic activity of Au electrodes, researchers have prepared nano-sized Au catalysts for electrochemical CO_2RRs. The thiolate-stabilized Au_{25} nanoclusters converted CO_2 to CO in 0.1 M $KHCO_3$ solution with approximately 100% FE and a partial current density of 15 mA cm^{-2} at −1 V vs. reversible hydrogen electrode (RHE), and the onset potential of the CO evolution was measured to be −0.19 V vs. RHE.[17] DFT calculations showed that an oxygen atom of CO_2 interacted with sulfur atoms in the thiolate-stabilized Au_{25} nanoclusters, and the adsorption of CO_2 molecules depleted the electrons in S atoms (**Figure 1.4**).[17]

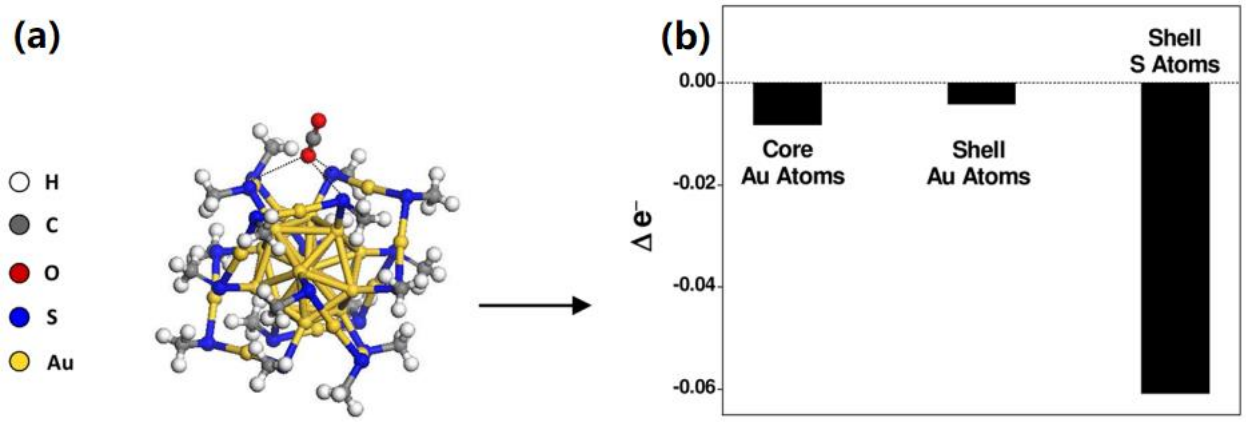

Figure 1.4. (a) DFT modeled stable geometry of CO_2 adsorption on the thiolate-stabilized Au_{25} nanoclusters. (b) The change of electrons upon CO_2 adsorption; negative values represent electron loss. Reprinted with permission from D. R. Kauffman, D. Alfonso, C. Matranga, H. Qian and R. Jin, *J. Am. Chem. Soc.* 2012, 134, 10237-10243. © 2012 American Chemical Society.

Zhu et al. reported that 8nm monodisperse Au nanoparticles reduced CO_2 in 0.5 M $KHCO_3$ with a maximum 90% FE at -0.67 V vs. RHE. The theoretical investigation of CO_2RR on Au nanoparticles showed that the edge sites stabilized the key intermediate *COOH, favoring the CO evolution over the HER. However, the corner sites on Au nanoparticles stabilized the intermediate *H, favoring the HER over the CO evolution (**Figure 1.5**).[18]

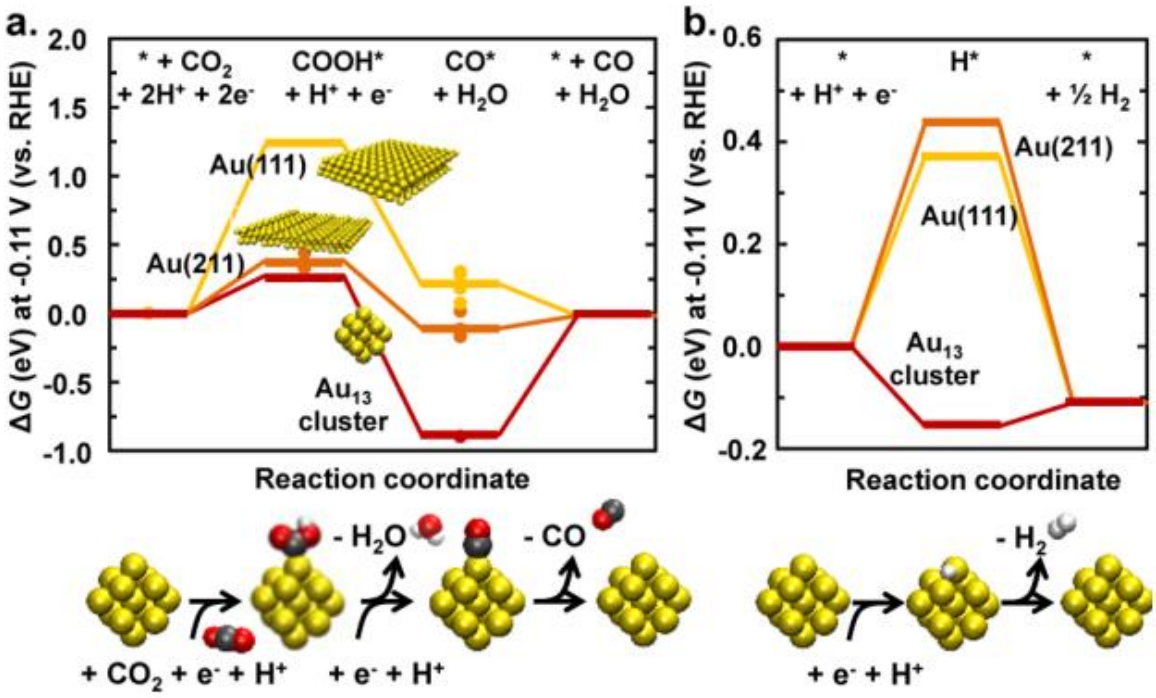

Figure 1.5. Free energy diagrams for the electrochemical (a) CO_2RR and (b) HER on Au(111), Au(211), or Au_{13} cluster at -0.11 V vs. RHE. Reprinted with permission from W. Zhu, R. Michalsky, Ö. Metin, A. A. Peterson, S. Sun et al., *J. Am. Chem. Soc.* 2013, 135, 16833-16836. © 2013 American Chemical Society.

To increase the number of edge sites on Au electrodes and improve the CO evolution, Zhu et al. synthesized ultrathin Au nanowires.[19] The edge site weight percentage on Au nanowires is larger than that on Au nanoparticles. The ultrathin Au nanowires in 0.5 M $KHCO_3$ solution exhibited a 94% FE for the CO evolution at −0.35 V vs. RHE.[19] DFT calculations showed that the CO binding is relative weak on Au nanowires, whereas the COOH binding is relative strong on Au nanowires (**Figure 1.6**). Mistry et al. investigated the size-dependent catalytic activities of 1.1–7.7 nm Au nanoparticles at −1.2 V vs. RHE, and found that the FE of the CO evolution became smaller and the FE of the HER became larger as the particle size decreased.[20] Unfortunately, the agglomeration of Au nanoparticles could reduce the surface areas of Au catalysts, causing the deactivation of the catalysts.[21]

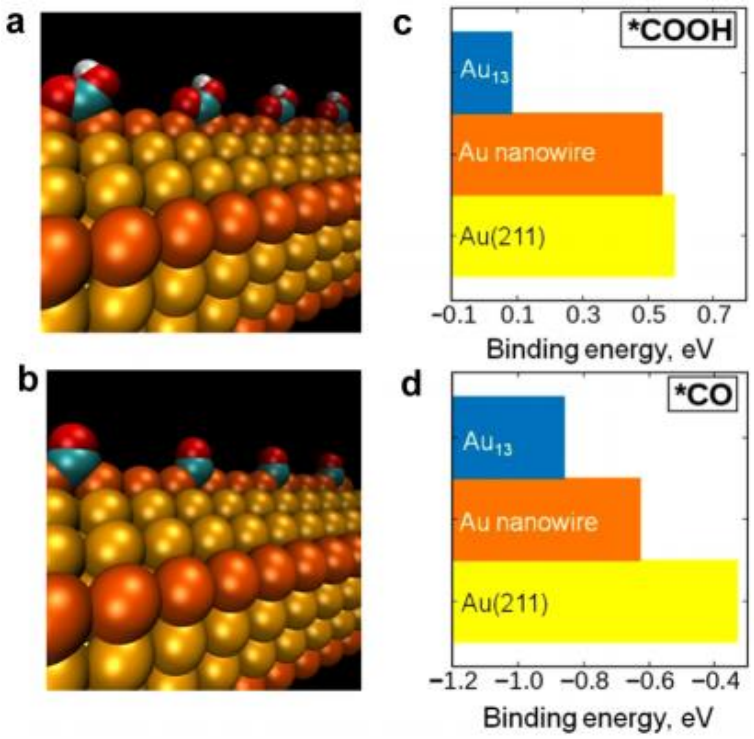

Figure 1.6. DFT calculated minimum energy geometries of (a) COOH and (b) CO on Au nanowires. The calculated binding energy of (c) COOH and (d) CO on the Au_{13} cluster, Au nanowires and Au(211). Reprinted with permission from W. Zhu, Y.-J. Zhang, H. Zhang, A. A. Peterson, S. Sun et al., *J. Am. Chem. Soc.* 2014, 136, 16132-16135. © 2014 American Chemical Society.

Alloy catalyst consists of two or more than two metals, and it shows special catalytic property for electrochemical CO_2RR. Watanabe et al. catalyzed CO_2RR using Cu alloy catalysts in 0.05 M $KHCO_3$ solutions.[22] The Cu-Ni catalyst produced CH_3OH and HCOOH selectively. Both the Cu-Sn and Cu-Pb catalysts produced HCOOH at a FE larger than 50%.[22] Rasul prepared Cu-In bimetallic electrocatalyst for CO_2RR.[23] The FEs of CO evolution and HER were 23% and 3% respectively on the Cu-In catalysts in 0.1 M $KHCO_3$ solution. The FE of CO evolution reached 90% at a potential of -0.5 V vs. RHE.[23] Christophe et al. prepared AuPd and AuCu alloys for electrochemical CO_2RRs.[24, 25] The AuPd electrodes produced H_2, CO, and $HCOO^-$ in 0.1 M $KHCO_3$ solutions, and showed higher activity and selectivity for $HCOO^-$ than

either pure Au or Pd.[24] The Au_xCu_{100-x} alloys were synthesized by melting Au and Cu metal together, where x denotes the atomic percent of gold. The electroreductions of CO_2 on AuCu alloys were conducted in the electrolyte of 0.01 M KH_2PO_4/0.1 M K_2HPO_4. Au_1Cu_{99} produced CO, CH_4, C_2H_4 and trace amount of C_2H_6. As the value of x increased, the Au_xCu_{100-x} alloys produced more CO and less CH_4.[25] Jia et al. prepared nanostructured Cu-Au alloys on a template of nanoporous Cu film (NCF).[26] The $Cu_{63.9}Au_{36.1}$/NCF in 0.5 M $KHCO_3$ produced methanol and ethanol at a FE of 15.9% and 12%, respectively. The FE of alcohols on $Cu_{63.9}Au_{36.1}$/NCF was ca. 6 times as large as that on pure Cu. Unfortunately, the dispersions of metals are hard to control in the synthesis of alloy catalysts.[27]

Andrews et al. prepared electrodes by combining Au nanoparticles and polymer binders together, and tested the electrocatalysis behavior on the prepared electrodes.[28] He used two polymer binders, porous Nafion and polyvinylidene fluoride (PVDF). The sulfonate moieties of Nafion are able to transfer protons within the porous Nafion, and chemisorb on Au surfaces.[29] PVDF is a sulfonate-free polymer. The current densities of CO_2RR on Au_{25}/PVDF, Au_{25}/Nafion, and gold foil are shown in **Figure 1.7**. The incorporation of Nafion in Au_{25} nanoparticles shifted the onset potentials of CO_2RR and HER by 190 mV anodically and 300 mV cathodically respectively, indicating Au_{25}/Nafion promoted the selectivity of electrochemical CO_2RR. On the other hand, the incorporation of (sulfonate-free) PVDF in Au_{25} nanoparticles shifted the onset potentials of CO_2RR by 110 mV anodically.

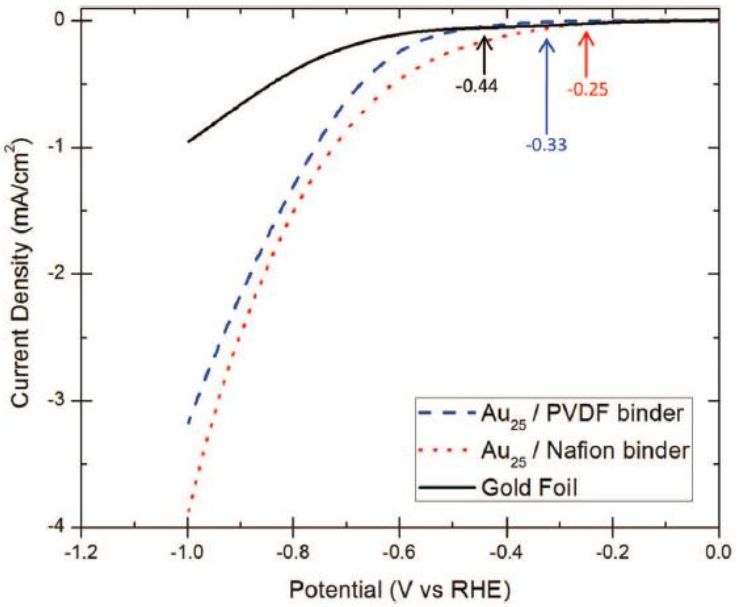

Figure 1.7. Linear voltammograms of Au_{25}/PVDF, Au_{25}/Nafion, and gold foil in CO_2 saturated 0.1 M $KHCO_3$ solutions. Reprinted with permission from E. Andrews, S. Katla, C. Kumar, M. Patterson, P. Sprunger and J. Flake, *J. Electrochem. Soc.* 2015, 162, F1373-F1378. © 2015 The Electrochemical Society.

The FE of CO_2RR on Au/polymer catalysts are shown in **Figure 1.8**. The FE of CO_2RR on Au_{25}/Nafion was measured to be almost 90% at 0.8 V vs. RHE. Nafion binder promoted both the FE and current density of electrochemical CO_2RR. The FE of CO_2RR on Au_{25} nanoparticles was higher than that on 5nm Au nanoparticles. X-ray photoelectron spectroscopy spectrum showed that sulfonate moieties altered the binding energies of key species and induced favorable reconstruction, enhancing the catalytic activities of Au nanoparticles.[28]

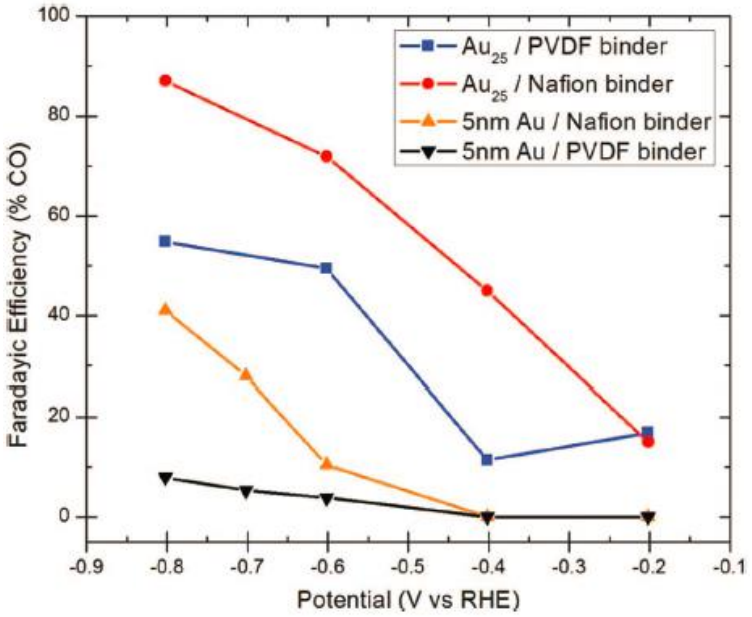

Figure 1.8. Faradayic efficiency plots of CO_2RR on Au_{25}/PVDF, Au_{25}/Nafion, 5 nm Au/Nafion, and 5 nm Au/PVDF catalysts, respectively. Reprinted with permission from E. Andrews, S. Katla, C. Kumar, M. Patterson, P. Sprunger and J. Flake, *J. Electrochem. Soc.* 2015, 162, F1373-F1378. © 2015 The Electrochemical Society.

Molecular catalysts catalyze electrochemical CO_2RRs in either homogeneous or heterogeneous reaction. Typically, the molecular catalyst reduces CO_2 at a low potential and high selectivity relative to the metal catalyst. The reductions of CO_2 using molecular catalysts are shown in **Table 1.4**. The current densities of homogeneous molecular catalytic reactions are low relative to the heterogeneous metal catalytic reactions. Thus, scientist deposited molecular catalysts on solid supports, and the solid-molecule catalysts gave high current densities. For example, the entries 3-6 in **Table 1.4**.[6]

Table 1.4. The reductions of CO_2 using molecular catalysts. Adapted with permission from J.-P. Jones, G. K. S. Prakash and G. A. Olah, *Isr. J. Chem.*, 2014, 54, 1451-1466. Copyright 2014 John Wiley and Sons.

Entry	Catalyst	E vs. SHE (V)	Current Density ($mA cm^{-2}$)	TOF (s^{-1})	Major Product	FE (%)	Notes
1	Mn(bipyridyl)CO_3Br	−1.7[a]	0.6		CO	85	0.1 M TBAP in 5% H_2O in MeCN
2	Ir-pincer	−1.41	0.6		$HCOO^-$	93	1% MeCN in 0.1 M $NaHCO_3$
3	Co-TPP	−0.90	100		CO	74.8	0.5 M $KHCO_3$
4	Co-TPP	−0.88	100		CO	97.3	20 atm CO_2, 0.5 M $KHCO_3$
5	Fe-TPP	−0.84	100		CO	42.4	0.5 M $KHCO_3$
6	Fe-TPP	−0.92	100		CO	80.9	20 atm CO_2, 0.5 M $KHCO_3$
7	Co-Tetraaza	−1.26		2.5×10^{-3}	CO	45	0.1 M KNO_3 in H_2O : MeCN 2 : 1
8	Ni-Tetraaza	−1.36		1.7×10^{-3}	CO	65	0.1 M KNO_3 in H_2O : MeCN 2 : 1
9	Polypyridyl Ru	−1.52	1.3		$CO/HCOO^-$	n/a	0.1 M nBu_4NPF_6 in MeCN
10	AgDAT/C	−1.4	34		CO	70	Flow Cell
11	FeTDHPP	−1.16	0.31	1000	CO	94	2 M H_2O in DMF
12	Ni(cyclam)	−1.21	1.8	90	CO	90	0.8 M tetrabutylammonium PF_6

[a] E vs. carbon electrode.

Bocarsly et al. reported that pyridinium ions catalyzed the reduction of CO_2 to methanol at a 30% FE on hydrogenated Pd electrodes[30], and formic acid and formaldehyde were observed as intermediates in this reaction.[31] Theoretical calculations suggested that pyridinium radicals were capable of reducing CO_2 to methanol without the metal-based electron transfer.[31] Bocarsly et al. further investigated a series of substituted pyridines for their catalytic activities in electrochemical CO_2RRs.[32] Typically, a substituted pyridine molecule with a higher basicity and LUMO energy gave more yields of CO_2 reduction.[32] Carter et al. proposed that electrode surface played a significant role in the pyridinium catalyzed CO_2RR.[33-35] Both the proton reduction and pyridinium reduction were thermodynamically unfavorable on the electrode surface, whereas the reduction of pyridine into dihydropyridine was thermodynamically favorable.[33] **Figure 1.9** shows the proposed mechanism for dihydropyridine catalyzed CO_2RR. A hydride ion and a proton are first transferred to a pyridine to produce dihydropyridine on the surface, and then transferred from the formed dihydropyridine to a CO_2 molecule to produce HCOOH molecule.

The reduction potential for converting pyridine to dihydropyridine is similar to that for converting CO_2 to reduced species.[33]

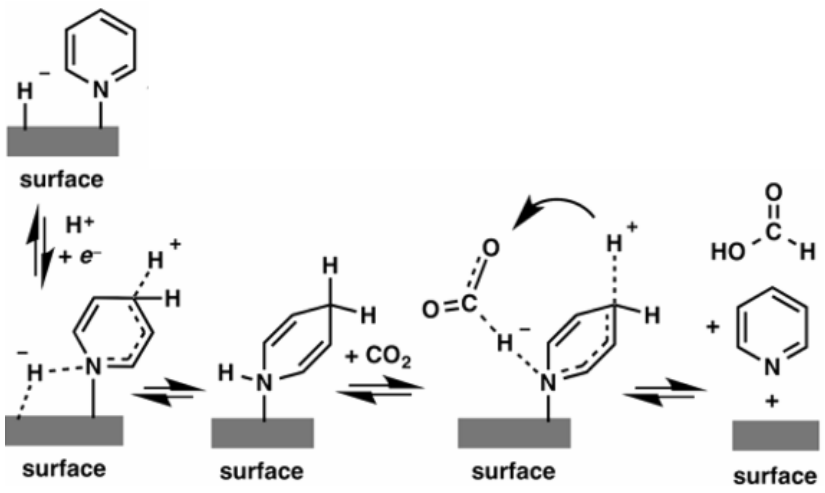

Figure 1.9. The mechanism for dihydropyridine catalyzed CO_2RR on electrode surface. Reprinted with permission from J. A. Keith and E. A. Carter, *J. Phys. Chem. Lett.* 2013, 4, 4058-4063. © 2013 American Chemical Society.

Re(bipy)$(CO)_3$Cl (bipy = 2,2′-bipyridine) and 6,7-dimethyl-4-hydroxy-2-mercaptopteridine (PTE) are homogeneous catalysts for CO_2RR.[36, 37] Re(bipy)$(CO)_3$Cl reduced CO_2 to CO in 0.1 M Et_4NCl solution at -1.25 V vs. NHE.[36] PTE catalyst gave methanol, formate and formaldehyde in 100 mM KCl solution at -0.65 V vs. Ag/AgCl.[37]

1.3. Enzyme catalyzed reduction of CO_2

Intriguingly, enzymes were found to be able to reduce CO_2. Carbon monoxide dehydrogenase (CODH) enzymes catalyzed both the oxidation of CO and the reduction of CO_2 at ambient conditions.[38-40] The CODH enzymes in Carboxydothermus hydrogenoformans and Methanosarcina barkeri were named as ChCODH II and MbCODH, respectively.[39, 41] Hansen et al. investigated the kinetic activity for CO evolution on transition metals, ChCODH II, and MbCODH respectively using computational methods (**Figure 1.10**).[42] The activities for CO

evolutions were calculated as a function of the adsorption energies of COOH (ΔE_{COOH}) and CO (ΔE_{CO}) at the pressures of p_{CO_2}= 1atm and p_{CO} = 1atm. The metals of Cu, Au and Ag showed high activities for CO evolution, with Au was the best one. The kinetic activities for CO evolutions on enzymes are higher than that on transition metals.

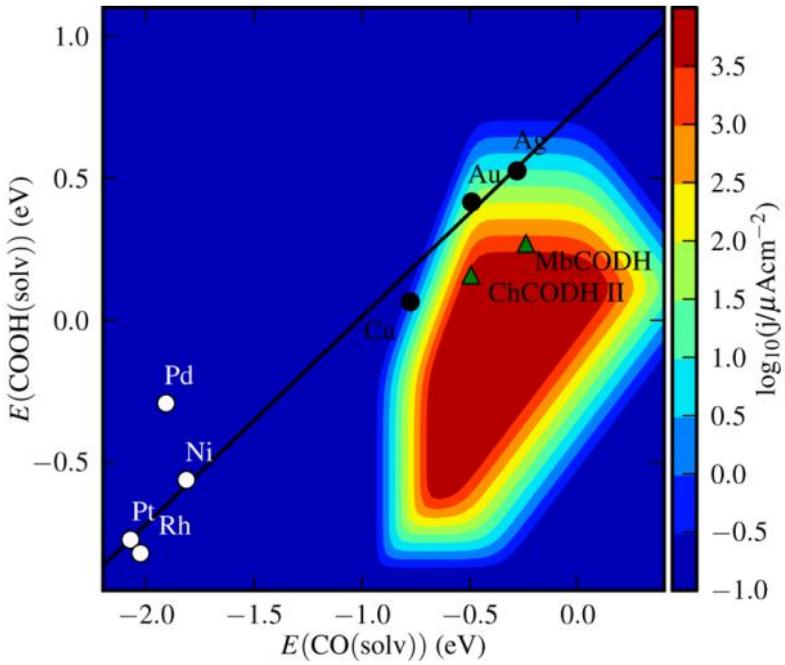

Figure 1.10. Kinetic activity for CO evolution on transition metals at a 0.35 V vs. RHE overpotential. The CO evolutions on ChCODH II and MbCODH are shown in the figure. Reprinted with permission from H. A. Hansen, J. B. Varley, A. A. Peterson and J. K. Nørskov, *J. Phys. Chem. Lett.* 2013, 4, 388-392. © 2013 American Chemical Society.

Hansen et al. modeled the adsorption of COOH on ChCODH enzyme (**Figure 1.11**)[42]. The ChCODH enzyme contains $NiFe_4S_5$ clusters and cysteine residues. The COOH molecule was coordinated to the ChCODH enzyme through both the C-Ni bond and the O-Fe bond, whereas the COOH molecule was bonded to the Au(211) only through the C-Au bond. Thus, the ΔE_{COOH} on the ChCODH enzyme is more negative than that on the Au(211).

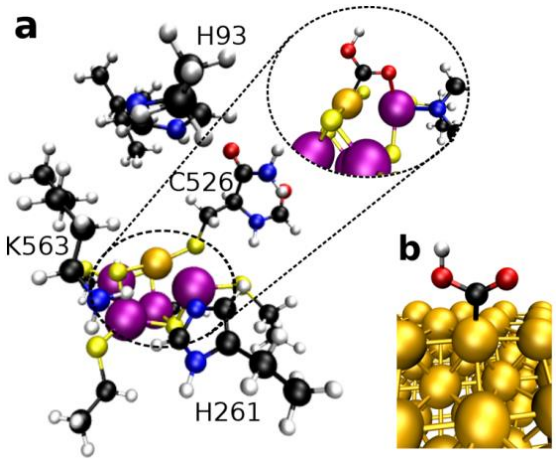

Figure 1.11. The binding geometries of COOH on (a) ChCODH and (b) Au(211). Au and Ni atoms are golden, Fe atoms are purple, C atoms are black, S atoms are yellow, O atoms are red, N atoms are blue, and H atoms are white. Reprinted with permission from H. A. Hansen, J. B. Varley, A. A. Peterson and J. K. Nørskov, *J. Phys. Chem. Lett.* 2013, 4, 388-392. © 2013 American Chemical Society.

As mentioned above: 1) Au electrodes exhibited high FE for the CO evolution at low overpotentials; 2) cysteine ligands modified $NiFe_4S_5$ clusters promoted CO_2RR by stabilizing COOH without stabilizing CO by a similar amount. Inspired by these two findings, we investigated the interaction of ligands with gold and the interaction effects on CO_2RR.

1.4. Interaction of thiols with Au

Thiol molecules are able to form stable and highly ordered SAMs spontaneously on noble metal surfaces.[43-45] Thiol SAMs modify metal surfaces with various chemical groups, such as -S, and -S-S-.[46-48] The dissociation of the thiolic H atoms from thiol molecules requires small energies of 0.3~0.4 eV,[49, 50] indicating that the dissociation takes place at ambient conditions. Scientists confirmed the formation of Au-S bonds in thiol SAMs.[51, 52]

Scientists have found that the adsorption of thiols on Au surfaces induced the reconstruction of Au surfaces.[53-57] **Figure 1.12** shows the scanning tunneling microscopy (STM)

images of MPA SAMs on Au(111). The MPA SAMs changed the morphology of Au(111). Pits and vacancy islands were formed on the reconstructed Au surfaces.[58]

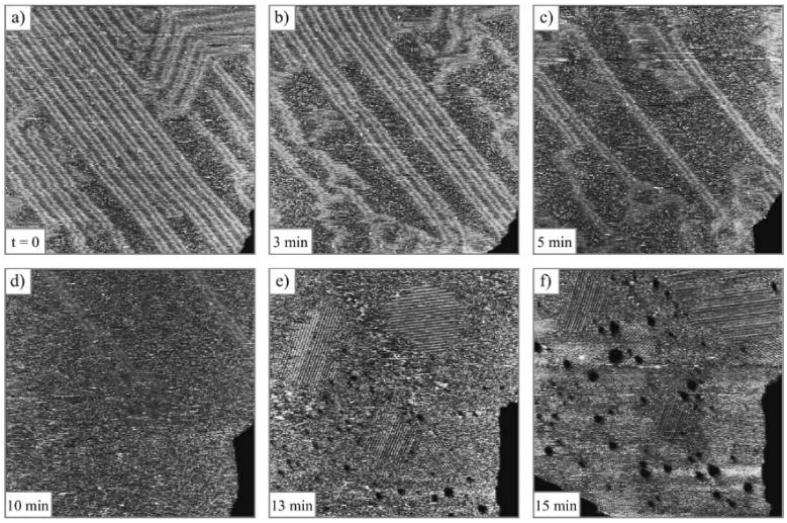

Figure 1.12. (a) The STM image of MPA SAMs on Au(111) in 0.1 M H_2SO_4 at E_{SCE} = -0.1 V. Images (b) to (f) were taken later than (a) by 3, 5, 10, 13 and 15 min, respectively. Reprinted with permission from M. Petri, D. M. Kolb, U. Memmert and H. Meyer, *Electrochim. Acta* 2003, 49, 175-182. © 2003 Elsevier.

Mobile Au adatoms were observed on thiol SAMs modified Au surfaces.[56, 57, 59] The Au adatoms were probably extracted out of the surfaces by adsorbed thiolates. Theoretical calculations demonstrated that the formation of Au-thiolate complex was thermodynamically favorable, and the complexes on reconstructed Au surfaces were more stable than that on unreconstructed Au surfaces.[60] STM images showed that two thiolates linked by one Au adatom formed a dithiolate-Au complex (the chemical formula of the dithiolate-Au complex is $(RS)_2Au$), and the complex was like a "staple" motif.[46, 57, 59] The coverage of $(RS)_2Au$ on Au flat terraces was calculated to be 1/3 monolayer (ML, the coverage is equal to the ratio of the number of S atoms to the number of Au atoms in a unit cell).[61] To the best of our knowledge, the configurations of thiolates on Au defect sites are not well understood.

Figure 1.13 shows the proposed scheme for thiolate induced reconstruction of Au(111). After we placed an Au foil into a 20 mM ethanolic solution of thiols, thiols formed SAMs on the surfaces of Au. The adsorption of thiols induced the reconstruction of Au(111) surfaces. Mobile thiolate molecules (RS) took Au atoms out of the Au(111) surfaces, generating thiolate-Au complexes (RSAu) and Au vacancies (V_{Au}). As more and more Au atoms were extracted out of the Au(111) surfaces, the V_{Au} coalesced into vacancy islands. Two RSAu reacted to produce $(RS)_2Au$, releasing one Au adatom to the surfaces. The Au adatoms then formed step edges and islands on the Au(111) surfaces.

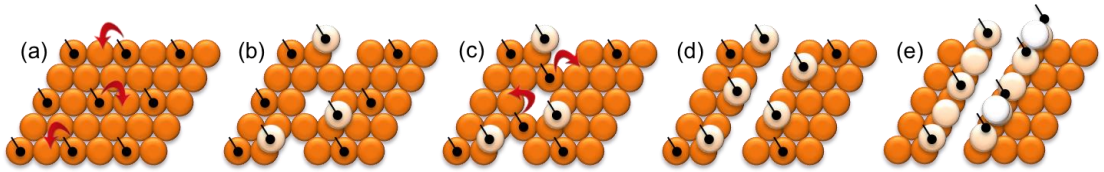

Figure 1.13. The proposed scheme of Au(111) reconstruction. (a) thiolates covered Au(111); (b) the formation of RSAu and V_{Au} on Au(111); (c) the Au atoms were extracted out of the surfaces; (d) V_{Au} coalesce into vacancy islands; (e) RS and $(RS)_2Au$ on the defect sites. Orange spheres are Au atoms, white spheres are Au adatoms, and blank dots are adsorbed ligands. Reprinted with permission from Y. Fang, X. Cheng, J. C. Flake and Y. Xu, *Catal. Sci. Technol.* 2019, 9, 2689-2701. © 2019 The Royal Society of Chemistry.

The proposed reconstruction process transformed the Au(111) surfaces into higher-index Au surfaces. The reactions in this process were written as below.

$$\left[RS\right]_{(111)} \rightarrow \left[\left(RS\right)_2 Au\right]_{(\varnothing)} + \left[RS\right]_{(\varnothing)}$$

where ($\varnothing$) represents the generated defect sites, such as Au adatoms and V_{Au}.

1.5. Stability of thiols on Au

The electrochemical stability of thiols on Au in aqueous solutions has been studied using infrared, linear sweep and cyclic voltammetry techniques. Azzaroni et al. measured the desorption potentials of various alkanethiols on Au(111) surfaces in 0.1 M NaOH solutions. The desorption

potentials of propanethiol, butanethiol, hexanethiol, dodecanethiol, and hexadecanethiol on Au(111) surfaces were determined to be -0.82, -0.86, -0.97, -1.15, and -1.22 V vs. saturated calomel electrode (SCE), respectively. The desorption potential of an alkanethiol shifted negatively as the chain length of that alkanethiol increased.[62] Munakata et al. measured the desorption potentials of ethanethiol, propanethiol, octanethiol, and decanethiol on Au(111) in 0.1 mol dm^{-3} phosphate buffer, respectively. They also found that the desorption potentials of an alkanethiol was more negative as that alkanethiol had a longer chain length (**Figure 1.14**).

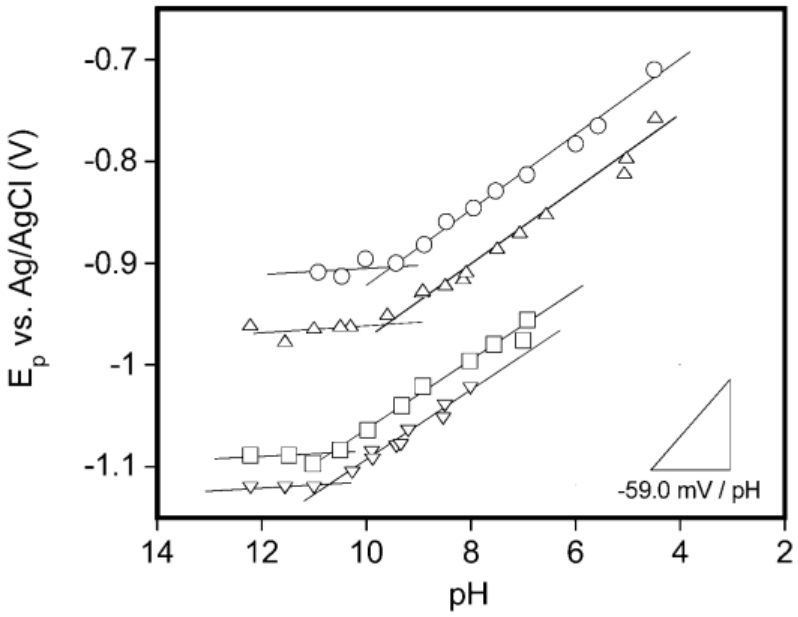

Figure 1.14. Desorption potentials of CH3-terminated alkanethiol SAMs of ethanethiol (○), propanethiol (Δ), octanethiol (□), and decanethiol (▽) on Au(111) as a function of the pH of the electrolyte solution. Voltammograms were measured at 200 mV s^{-1} in 0.1 mol dm^{-3} phosphate buffer. Reprinted with permission from H. Munakata, D. Oyamatsu and S. Kuwabata, *Langmuir*, 2004, 20, 10123-10128. © 2004 American Chemical Society.

The pH of the solution also influenced the desorption potentials. The increase of pH of the solutions made the desorption potentials of alkanethiols more negative.[63] The solubilities of alkanethiols have been studied. 1-propanethiol and 1-hexadecanethiol molecules formed

aggregates in the vicinity of Au(111) surfaces in 0.5 M KOH solutions.[64] The solubility of nonanethiol in aqueous solution reduced as the pH of the electrolyte solution decreased.[65]

The linear sweep voltammetry curve for Au-S-CH_2-C_6H_5 is shown in **Figure 1.15**. The peaks in the curve represent the desorption of the monolayer from the Au surfaces. It is noted that the curve has a sharp peak at -950 mV vs. Ag/AgCl and a broad peak at -1100 mV vs. Ag/AgCl. The appearance of two different peaks could be attributed to the desorption of two different ligand states from the Au surfaces.[66]

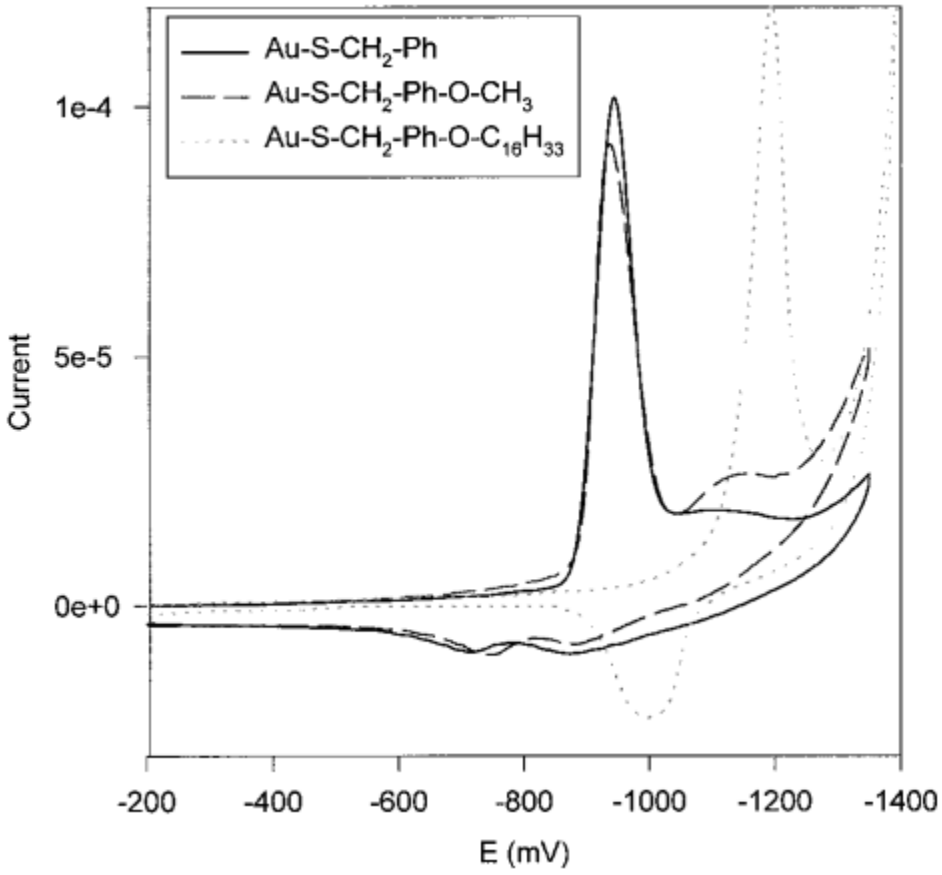

Figure 1.15. Cyclic voltammetry curves for Au-S-CH_2-C_6H_5, Au-S-CH_2-C_6H_4-O-CH_3, and Au-S-CH_2-C_6H_4-O-$C_{16}H_{33}$ monolayers on Au(111) in 0.5 M KOH solution. Reprinted with permission from Y.-T. Tao, C.-C. Wu, J.-Y. Eu, W.-L. Lin, K.-C. Wu and C.-h. Chen, *Langmuir*, 1997, 13, 4018-4023.. © 1997 American Chemical Society.

Thiophenol, phenylmethanethiol (PMT) and 2-PET belong to the class of phenyl-terminated alkanethiols. The numbers of methyl group between the aryl and the mercapto group of thiophenol, PMT, and 2-PET are 0, 1, and 2, respectively. The desorption potentials of thiophenol and PMT on Au(111) in 0.5 M KOH solution were measured to be -0.85 and -0.92 V vs. Ag/AgCl, respectively. The desorption peak potential of PMT was sharp and well-defined, indicating that PMT formed closely packed and ordered monolayers on the surface.[66] On the other hand, the peak potential of thiophenol was broad and ill-defined, indicating that thiophenol molecules formed disordered SAMs on the surface.[66, 67] The aromatic rings in thiophenol molecules were found to transfer electrons from the Au electrode to the thiophenol SAMs.[67]

The -COOH and -NH_2 groups influence the desorption potentials of alkanethiols on Au(111). The interaction between -COOH groups made alkanethiol molecules less stable on Au surfaces, which was due to the repulsive forces between carboxyl groups.[62] The desorption of HOOC-$(CH_2)_5$-SH SAMs on Au(111) surfaces took place at ca. -0.8 V vs. Ag/AgCl in 0.5 M KOH solution.[68] The adhesion force between -NH_2 groups was found to be stronger than that between -COOH groups.[69-71] The desorption of NH_2-$(CH_2)_6$-SH SAMs on an Au electrode took place at ca. -1.1 V vs. Ag/AgCl in 0.5 M KOH solution.[72] The basicity of an alkanethiol molecule could be estimated in experiments if the alkanethiol molecule has pH-sensitive groups, such as amino and carboxyl groups. The -COOH groups of adsorbed COOH-terminated alkanethiols were deprotonated in pH > 7.5 solutions, whereas the -NH_2 groups of adsorbed NH_2-terminated alkanethiols were protonated in pH < 6.4 solutions.[63] The desorbed 3-mercaptopropionic acid (3-MPA) molecule dissolved into the solutions because of the high solubility of the -COOH group.[64]

Although state-of-the-art experimental techniques have generated considerable insight into the adsorption and desorption of thiols on Au surfaces, many details remain unclear, including what the desorbing species is, and what state it originates from.

1.6. Influence of ligands on catalytic activity of metals

Adsorbed ligands on gold influence the catalytic activity of Au significantly. Liu *et al.* reported that Schiff base functionalized Au catalysts dehydrogenated formic acid to H_2 without any additives, which was attributed to Schiff base induced increase of electron density of the Au active centers and the β-hydride elimination in the Au-formate complex.[73] Rodriguez *et al.* promoted the electrocatalytic alcohols oxidation activity of Au(111) by depositing CO on the surface irreversibly, and they concluded that adsorbed CO enhanced the adsorption of OH on Au, which catalyzed beta-hydrogen elimination in the oxidation of alcohols.[74] Rao *et al.* demonstrated that DNAzyme-Au NP dual catalyst can effectively catalyze the H_2O_2-mediated oxidation of 2,2′-azino-bis(3-ethylbenzothiazoline)-6-sulfonic acid (ABTS) for the colorimetric detection of thrombin.[75] Qiu *et al.* prepared poly(allylamine hydrochloride) (PAH)/Prussian blue (PB)@Au electrode, which showed excellent electrocatalytic activity toward the reduction of hydrogen peroxide.[76]

Ligands have also been used to modify other metals. Tartaric acid modified nickel and cinchona alkaloids modified platinum catalysts are used to heterogeneous asymmetric catalyze the hydrogenation of 2-alkanones and a-ketoesters, respectively.[77] Hwang *et al.* showed that potassium-modified Ni metal was more active and selective for the water–gas shift (WGS) reaction than unmodified Ni catalysts due to potassium induced formation of active hydroxyl group.[78] Zhang *et al.* modified acetylacetone-metal catalyst with pyridinium salt, and they noted that pyridinium salt was able to withdraw electrons and accelerate the decomposition of alkyl hydroperoxide.[79] McKenna et al. found that the modification of Pd/TiO_2 catalyst using

triphenylphosphine and phenyl sulfide would enhance selectivity for acetylene hydrogenation, and they proposed that ligands induced electronic promotion and geometric effects on the catalyst.[80] Gong *et al.* demonstrated that active carbon (AC)-SO_3H modified Cu catalyst enhanced the selective hydrogenation of furfural to furfuryl alcohol, and SO_3H group was responsible for higher reduction degree of Cu, better dispersion of NPs, and stronger adsorption of furfural.[81] Sulfur modification of Ru deactivated carbonyl hydrogenation and C-C and C-O hydrogenolysis, and the electron transfer from Ru to S lead to the generation of hydroxylated Ru.[82]

1.7. Overview of research works

First of all, we investigated the Au-C bond formation on Au(111) (Chapter 3.1). Our computational calculations suggested that the strength of the Au-C bond of $Au{-}C_6H_4{-}SH$ was ca. 0.4 eV stronger than that of the Au-S bond of $Au{-}S{-}C_6H_5$ on Au(111). Since the stabilities of modified gold electrodes are very important in catalytic reactions, we expected that the formation of Au-C bonds would stabilize the modified gold electrodes in electrochemical CO_2RRs.

Secondly, we investigated the nitrogen compound (adenine) on Au (Chapter 3.2). Our DFT calculations demonstrated that adenine in upright configuration was ca. 0.2 eV more stable than that in parallel configuration. Thus, to maintain the stability of adenine modified Au electrode in electrochemical CO_2RRs, the adenine molecules should be deposited in upright configurations on the surface.

Thirdly, we investigated the electrochemical stability of 2-PET thiolate on Au (Chapter 3.3). Our calculations suggested that 2-PET thiolate molecules persisted on the Au(211) surfaces in the potential range of 0 to -1.3 V vs. RHE, indicating that 2-PET-Au was stable in electrochemical CO_2RR experiments (The CO_2RRs were conducted at -0.24 V vs. RHE in experiments[83]).

Finally, we investigated the electrochemical CO_2RR on thiolated-Au (Chapter 3.4). We selected two thiol ligands, 2-PET ($C_6H_5(CH_2)_2SH$, **Figure 1.16a**) and 2-MPA ($CH_3CHSHCOOH$, **Figure 1.16b**), to study in our research. 2-PET has a phenyl group, whereas 2-MPA has a carboxyl group.

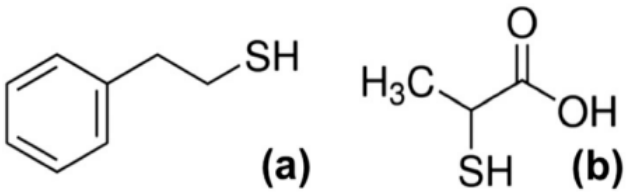

Figure 1.16. The molecular configurations of (a) 2-PET and (b) 2-MPA. Reprinted with permission from Y. Fang, X. Cheng, J. C. Flake and Y. Xu, *Catal. Sci. Technol.* 2019, 9, 2689-2701. © 2019 The Royal Society of Chemistry.

We performed DFT calculations to investigate the interactions of 2-PET or 2-MPA with gold on defect sites. The calculated results demonstrated that adsorbed ligands changed the structural and electronic properties of the defect sites, enhancing the catalytic activities of Au electrodes. The adsorbed ligands had negligible poisoning effects on the Au catalysts. Thus, the modification of Au electrodes with specific ligands is a simple and effective way to improve the catalytic activity and selectivity of electrochemical CO_2RRs.

Chapter 2. Computational Methods

All periodic DFT calculations were performed using the Vienna Ab initio Simulations Package (VASP, v.5.4)[84, 85] in the optB86b[86-88] and optB88[87] van der Waals (vdW) functionals, and the generalized gradient approximation revised Perdew-Burke-Ernzerhof (GGA-RPBE) functional[89]. Functionals were used to estimated the exchange and correlation interactions between electrons. The RPBE functional estimates the chemisorption energies of molecules accurately,[90] but it can not gain the information of the vdW interactions. On the other hand, the optB8x functionals are well known for the calculations for the vdW forces.[86] The adaptive sum method[91] combines the RPBE and optB8x functionals, improving the accuracy of DFT calculations. The delocalized charge densities of adenine and thiophenol molecules contributed to vdW interactions and covalent bonding. Thus, we used both the optB8x and RPBE functionals in our calculations.

The core electrons were described using the projector-augmented wave (PAW) method,[89] and the valence electrons [Au(*1s10d*), S(*2s4p*), O(*2s2p*), N(*2s2p*), C(*2s2p*), H(*1s*)] were expanded in Kohn-Sham one-electron orbitals up to 400-700 eV. The PAW method is a generalization of pseudopotential and linear augmented wave methods, and increases the computational efficiency of DFT calculations.[92] The Kohn-Sham equation is the one electron Schrödinger-like equation of a fictitious system of non-interacting particles that have the same density as any system of interacting particles.[93] DFT calculations have convergence problems when electron occupation is changed by small perturbations. To lessen the effect of perturbation, the electronic states were smeared with a width of 0.1 eV using the Methfessel-Paxton approach[94], and all total energies were extrapolated back to 0 K. The RPBE, optB88-vdW and optB86-vdW lattice constants for Au were determined to be 4.198, 4.177 and 4.122 Å respectively,[95] which are in close agreement with the experimental value 4.08 Å[96].

The Au surfaces were modeled with semi-infinite slabs (**Figure 2.1**) that were repeated in x, y directions, and neighboring slabs in the z direction were separated by 19-24 Å vacuum, with dipole decoupling in the z direction.[97] The top two layers and any adsorbates thereon were fully relaxed, and Au atoms that were not relaxed were held at bulk positions. All slabs were sampled on a Γ-centered Monkhorst-Pack k-point grid (k-points is 3×3×1 or 5×5×1 or 7×7×1). The Monkhorst-Pack method constructs equally spaced mesh in Brillouin zone. Geometry optimization was considered converged when the residual force in every relaxed degree of freedom in the system was lower than 0.03 eV/Å.

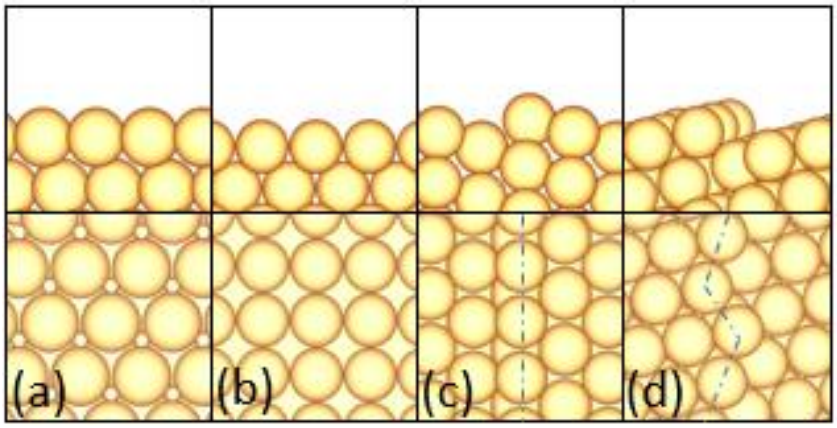

Figure 2.1. The geometries of blank Au surfaces: (a) Au(111), (b) Au(100), (c) Au(211), and (d) Au(563). The top panels are side views and the bottom panels are top views. The blue dashed lines indicate the step edges.

The total energies of the gas-phase species were calculated in an 18×18.2×18.4 $Å^3$ simulation cell. To compensate for a systematic error in RPBE, a correction of 0.45 eV was applied to the gas-phase CO_2 molecule.[42] A neutralizing background charge was added for the calculation of an isolated anion. The Gibbs free energies (G_A) of 2-PET, phenethyl disulfide and

2-PET anion (2-PET$^-$) molecules were determined by the equation (2.1),[98] assuming ideal gas behavior and standard state (1 bar and 298 K):

$$G_A = E^{DFT} + \Delta G(T, p)$$
$$= E^{DFT} + (E^{ZPE} + k_BT + E_{trans} + E_{vib} + E_{rot} - T(S_{trans} + S_{vib} + S_{rot})) \quad (2.1)$$

where E^{ZPE}, k_B and T are zero-point energy (ZPE), Boltzmann constant and temperature, respectively. E_{trans}, E_{vib}, E_{rot}, S_{trans}, S_{vib}, and S_{rot} are the translational, vibrational and rotational thermodynamic contributions to the gas-phase species (E and S stand for enthalpy and entropy, respectively). The enthalpies and entropies of molecules were calculated using statistical mechanics methods because tabulated data are not available.

The Gibbs free energies of 2-PET, phenethyl disulfide and 2-PET$^-$ molecules in aqueous phase ($G_{A(aq)}$) were determined by the equation (2.2)[99], assuming ideal solution behavior and standard state (1 M and 298 K):

$$G_{A(aq)} = G_A + \Delta G^{1bar \rightarrow 1M} + \Delta G_{sol} + k_BT \times \ln[A] \quad (2.2)$$

where $\Delta G^{1bar \rightarrow 1M}$ represents the energy for changing the standard state from 1 bar to 1M, ΔG_{sol} is the solvation energies of molecules in aqueous solutions, and [A] is the concentration of solute. ΔG_{sol} was calculated using the implicit solvation model implemented in VASPsol.[100] The implicit solvation model estimated the solvation energies of thiols adequately (the implicit solvation energies of 2-PET and phenylethyl disulfide are -0.12 and -0.17 eV, respectively), but it failed to estimate the solvation energies of thiol anions.[101] The incorporation of three explicit water molecules into the implicit solvation model stabilized the PMT anion by -0.52 eV.[101] Since the molecular structure of 2-PET is similar to that of PMT, we corrected the implicit solvation energies of 2-PET anion by -0.52 eV in our calculations. The value of $\Delta G^{1bar \rightarrow 1M}$ (0.08 eV) was taken from literature.[102]

The adsorption energy (ΔE_{ads}) of adsorbates on blank or functionalized Au slabs were calculated as:

$$\Delta E_{ads} = E_{total} - E_{slab} - E_g$$

where E_{total}, E_{slab} and E_g are the DFT total energies of the system, the energies of blank or functionalized Au slabs, and the energies of adsorbate species isolated in the gas phase, respectively.

According to previous studies[103, 104], the average adsorption energy of dithiolate-Au complex on Au surfaces was calculated as:

$$\Delta E_{ads} = \frac{1}{2}\left(E_{total} - E_{slab} - E_{Au}\right) - E_g$$

where E_{Au} is the energy of a bulk Au atom. In this study, the thiolates do not have partial pressures in the gas phase. The adsorption energies of thiolates on the surfaces can not be calculated by using the gas phase as reference state. We calculated the E_g for the comparison of the relative stabilities between different thiolate states.

The Gibbs free energy of ($H^+ + e^-$) was calculated as $G[H^+ + e^-] = \frac{1}{2}G[H_{2(g)}]$ at pH = 0 and 0 V vs. SHE.[105] When the pH of the solution is not equal to 0, the Gibbs free energy was corrected by $+k_B T \cdot \ln[H^+]$, where $[H^+]$ represents the concentration of H^+ ions.

The Gibbs free energy (ΔG_{rxn}) of the reaction $CO_{2(g)} + H^+_{(aq)} + e^- + * \rightarrow COOH^*$ was calculated as:

$$\Delta G_{rxn}^{SHE} = G[COOH^*] - G[CO_{2(g)}] - G[*] - \left(\frac{1}{2}G[H_{2(g)}] + k_B T \cdot \ln[H^+]\right)$$

where * denotes a free site, and COOH* denotes reaction intermediate COOH on surfaces.

The potential of the RHE is related to that of the SHE as $U_{RHE} = U_{SHE} + k_B T \cdot \ln[H^+]/e$. The ΔG_{rxn} on RHE was calculated as:

$$\Delta G_{rxn}^{RHE} = G\left[\mathrm{COOH}^*\right] - G\left[\mathrm{CO}_{2(g)}\right] - G\left[*\right] - \frac{1}{2}G\left[\mathrm{H}_{2(g)}\right]$$

The equilibrium potential was calculated as $U° = -\Delta G_{rxn}/e$. The protons in neutral solutions were generated from the dissociation of water molecules: $H_2O - OH^-_{(aq)} \rightarrow H^+_{(aq)}$. The energy of $(H_2O - OH^-_{(aq)})$ is identical to that of $H^+_{(aq)}$ on RHE.[106]

The Gibbs free energies (G_g) of H_2, CO_2 and CO in gas phase were calculated as[107]:

$$G_g = E + \Delta G(T,p) = E + \left(E^{ZPE} + \Delta h(T,p^\circ) - Ts(T,p^\circ) + k_B T \cdot \ln\left(p/p^\circ\right)\right) \quad (2.3)$$

where E is the DFT total energy of gas phase H_2 or CO_2 or CO, k_B is the Boltzmann constant, T is temperature, p is pressure with $p° = 1$ bar as the reference pressure, and h and s represent the enthalpy and entropy contributions to the free energies, respectively. Δh was calculated as $h(T,p^\circ) - h(0\ \mathrm{K},p^\circ)$. The values of T and p were taken as 298.15 K and 1 bar. The values of h and s for gas phase H_2, CO_2 and CO were taken from the NIST WebBook.[108] We used experimentally measured h and s of gas phase H_2, CO_2 and CO for accuracy. The statistical calculations for h and s assumes gases are in the ideal conditions, thus producing errors in the calculations.

The Gibbs free energies (G_{ads}) of adsorbates on Au surfaces were calculated as:

$$G_{ads} = E + \Delta G(T) + \Delta E_{solv} + \mu_0 \times \varepsilon = E + \left(E^{ZPE} + \Delta u(T) - Ts(T)\right) + \Delta E_{solv} + \mu_0 \times \varepsilon \quad (2.4)$$

where E is the DFT total energy of adsorbate on surface, ΔE_{solv} is the solvation energy of the system, μ_0 represents the static surface dipole moment at zero electric field, and ε represents the local electric field, Δu is the internal energetic difference between T and 0 K. The E^{ZPE} in

equations (2.1), (2.3) and (2.4), Δu and s in equation (2.4) were determined by the calculations of the vibrational normal modes and their frequencies using two-sided finite difference approximation of the dynamical matrix, with the magnitude of the displacement was 0.01 Å in each degree of freedom. The ΔE_{solv} for *COOH and *CO were taken from literature.[42] The term of $\mu_0 \cdot \varepsilon$ is the interfacial electric field effects on the energies of adsorbed species, and is approximated as the first-order Stark effect. Although the polarizability of *COOH was |0.2| eÅ^2/V or less on Ag surfaces,[109] the $\mu_0 \cdot \varepsilon$ for *COOH was significant, thus the $\mu_0 \cdot \varepsilon$ correction should be considered in our calculations.[110] The dipole moment pointed from positive to negative charges along the positive z direction in our models. The value of ε was estimated to be -1.0 V Å^{-1}.[109]

For a slab with two adsorbates on it, such as *COOH and 2-PET* on Au(211), E, ΔG, E^{ZPE} and μ_0 represent the DFT total energy, Gibbs free energy, ZPE and static surface dipole moment of the overall system, respectively. G[*] is the sum of the Gibbs free energies of adsorbed thiolate and Au slab. The initial configuration of any system was first optimized using *ab initio* molecular dynamics simulation at 300 K. Then the minimum free energy configuration from the coarse-grain optimization was further optimized using DFT methods.

Three types of desorption reactions were considered:

I) Reductive desorption with the transfer of a couple of proton and electron (RS denotes a thiolate species):

$$RS^* + H^+_{(aq)} + e^- = RSH_{(aq)}$$

II) Reductive desorption with the transfer of one electron:

$$RS^* + e^- = RS^-_{(aq)}$$

III) Thermal desorption to produce disulfide:

$$2RS^{*} = RSSR_{(aq)}$$

The total Gibbs free energy of $(H^{+}_{(aq)} + e^{-})$ was equal to that of H_2 gas at 0 V vs. SHE at standard conditions (1 bar and 298 K). At a certain proton concentration (represented by pH) or electrode potential (represented as U_{SHE}), the Gibbs free energy of a couple of proton and electron was calculated as $G(H^{+} + e^{-}) = \frac{1}{2}G_{H_{2(g)}} - eU_{SHE} - k_B T \cdot \ln(10) \cdot pH$.[105]

In the case of an electron transfer without a simultaneous proton transfer, the calculated absolute electrode potential is equal to the sum of the SHE potential and 4.3 V in aqueous electrolytes consistent with literature[111, 112], i.e., the free energy of an electron is -4.3 eV at 0 V vs. SHE. We noted that the E^{DFT} of H_2 and H^{+}, coupled with calculated and literature values for various free energy contributions, imply the absolute electrode potential to be +4.44 V_{SHE} using the optB86b-vdW functional. The application of +4.44 V_{SHE} in calculations caused a gap of 0.14 V between the redox potential of coupled proton/electron transfer and that of one electron transfer in the pH = pKa (see below) solution, which was due to the intrinsic limits of the accuracy of DFT methods as well as errors in various free energy contributions. The errors are unavoidable given the current state of theory.

The pKa of 2-PET in water was determined by[113]:

$$\text{pKa} = \frac{-(G_{2\text{-}PETt^{-}(aq)} + G_{H^{+}_{(aq)}} - G_{2\text{-}PET(aq)})}{\ln(10) \cdot RT}$$

to be 10.63. The calculated pKa of PMT is 9.86, which is similar to the experimental pKa of PMT (9.43). The pKa of various alkanethiols are in the range of 10~11[114]. The molecular structure of 2-PET is similar to the PMT, thus the calculated pKa of 10.63 was reasonable. To calculate $G_{H^{+}_{(aq)}}$ at 1 M, the Eq. 2.2 was used. $\Delta G_{solv}(H^{+})$ = -11.53 eV was taken from literatures.[102, 111, 112, 115]

Chapter 3. Results and Discussion

3.1. Au-C bond formation on Au

3.1.1. Experimental findings

Guo et al. prepared Au−C_6H_4−SH films on gold by electro-reducing of an aryl diazonium salt of 4,4′-disulfanediyldibenzenediazonium (DSBD) on a gold disk electrode. The formed monolayers (Au−Ar−S^-) were found to be more stable than the well-known SAMs of Au−S−C_6H_5, indicating that it is promising to modify Au electrodes with Au−C_6H_4−SH films in electrochemical CO_2RRs. **Scheme 3.1** shows the process for the formation of Au−Ar−S^- monolayers. The electroreduction of DSBD produced multilayers of Au−(Ar−S−S−Ar)$_n$. Then, the multilayers were further cut into monolayers of Au−Ar−S^- using electrochemical methods.

Scheme 3.1. The mechanism for the formation of Au−Ar−S^- monolayers.

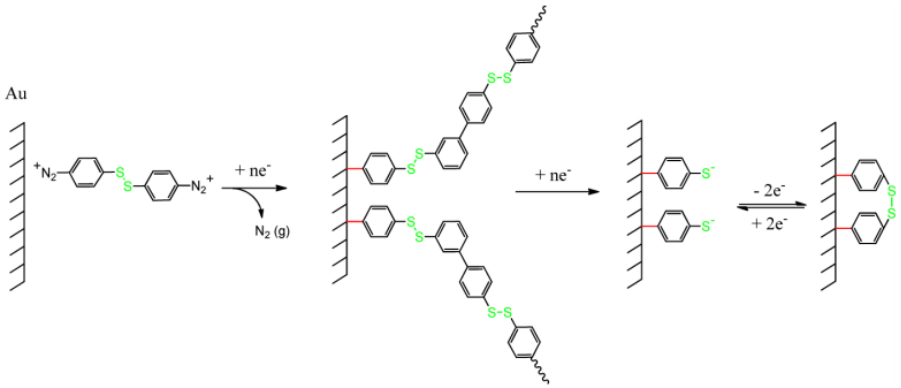

This chapter contains materials from three previous published articles: 1) L. Guo, L. Ma, Y. Zhang, X. Cheng, Y. Xu, J. Wang, E. Wang*, Z. Peng*, "Spectroscopic Identification of the Au–C Bond Formation Upon Electroreduction of an Aryl Diazonium Salt on Gold" *Langmuir* 2016, 32, 11514-11519. © 2016 American Chemical Society; 2) R.G. Acres, X. Cheng, K. Beranová, S. Bercha, S. Skála, V. Matolín, Y. Xu, K.C. Prince, N. Tsud*, "An Experimental and Theoretical Study of Adenine Adsorption on Au(111)" *Phys Chem Chem Phys* 2018, 20, 4688-4698. © 2018 The Royal Society of Chemistry; 3) Y. Fang, X. Cheng, J. Flake*, Y. Xu*, "CO_2 Electrochemical Reduction at Thiolate-Modified Bulk Au Electrodes" *Catal Sci Technol* 2019, 9, 2689-2701. © 2019 The Royal Society of Chemistry. Adapted by permission of American Chemical Society and The Royal Society of Chemistry, respectively.

Figure 3.1a shows the cyclic voltammetry spectrum of the electroreduction of DSBD on a gold electrode. The current density decreased after a few potential cycles, indicating that insulating films had been deposited on the electrode.[116] The integration of the charge on the electrode gave 1226 μC cm^{-2}, which corresponded to the formation of multilayers of $-(Ar-S-S-Ar)_n$ on the electrode.[117, 118] **Figure 3.1b** shows the in situ surface-enhanced Raman spectroscopy (SERS) spectrum of the multilayers on gold electrode and the Raman spectrum of DSBD powder. The band at 419 cm^{-1} was assigned to the vibration of Au-C bond.[119, 120]

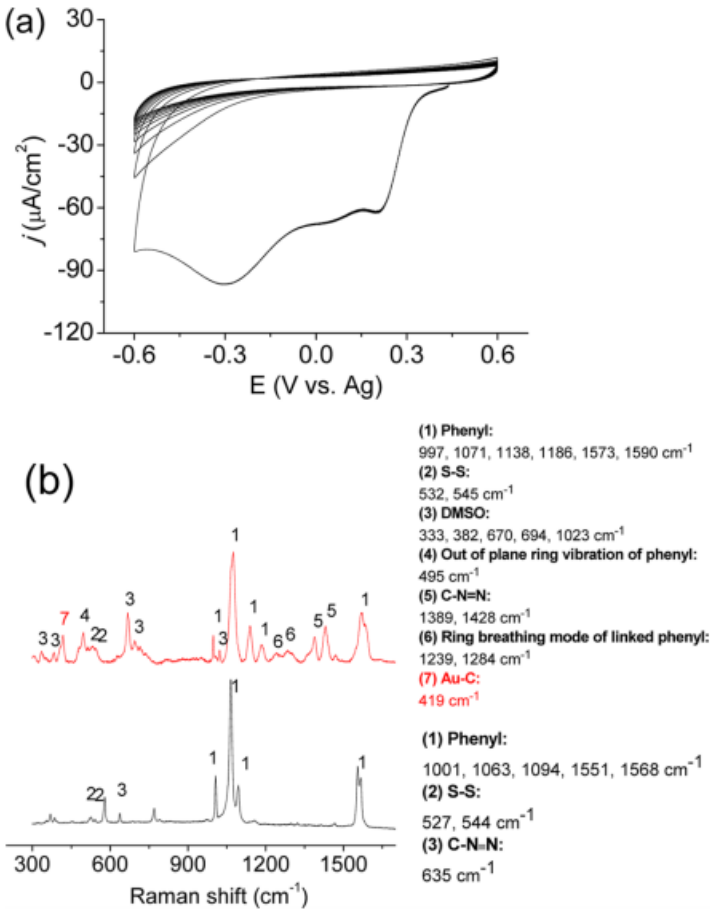

Figure 3.1. (a) Cyclic voltammetry spectrum of electroreduction of 2 mM DSBD on gold in 0.1 M $TBAClO_4$ DMSO solution at a potential scan rate of 0.1 V s^{-1}. (b) SERS spectrum of grafted multilayer on gold (red curve) and Raman spectrum of DSBD powder (black curve).

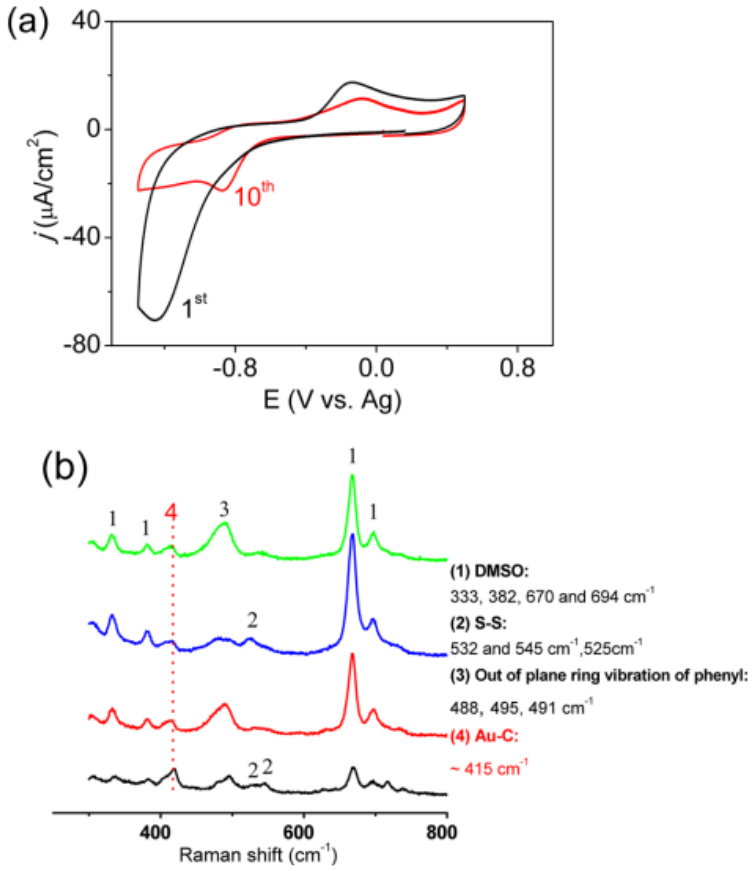

Figure 3.2. (a) 1st (black) and 10th (red) cycles of the degradation of a $-(Ar-S-S-Ar)_n$ multilayer on a gold electrode; scan rate is 0.1 V s^{-1}. (b) SERS spectra of $Au-Ar-S^-$ monolayer on a gold electrode: (green) in reduced state at −1.4 V; (blue) in oxidized state at 0.5 V. SERS spectra of $-(Ar-S-S-Ar)_n$ on a gold electrode: (red) after the degradation at −1.4 V; (black) before the degradation.

The degradation of the multilayers of $Au-(Ar-S-S-Ar)_n$ were conducted using electrochemical methods.[116] In **Figure 3.2a**, the reduction peak of the 1st (black) potential cycle corresponded to the formation of $Au-Ar-S^-$ moieties.[116] In **Figure 3.2.b**, the red curve shows the spectrum of the electrode after the degradation. The vibrational modes of S-S group[29] at 532 and 545 cm^{-1} disappeared in the red curve, indicating that the degradation broke the S−S bonds. The vibrational mode of Au-C stretching at 415 cm^{-1} was observed at both −1.4 and 0.5 V, which showed that Au-C bonds were stable on the electrode in the potential range of -1.4 to 0.5 V.

3.1.2. Theoretical results

We investigated the Au-C and Au-S bonds of the given compounds on Au(111) using DFT methods. We modeled the Au(111) facet since it is the most stable facet of Au. The DFT calculated minimum energy structures for Au−C_6H_4−SH and Au−S−C_6H_5 are shown in **Figure 3.3**. For Au−C_6H_4−SH, the H atom para to the SH group was removed from the thiophenol molecule. The ligand of −C_6H_4−SH preferred to adsorb on the top site of an Au atom in upright configuration (**Figure 3.3a**). For Au−S−C_6H_5, the H atom in the SH group was removed from the thiophenol molecule. The S headgroup were located on somewhere between a bridge site and a three-fold fcc site on the surface (**Figure 3.3b**). The C-S bond of Au−S−C_6H_5 tilted to the Au surfaces, which was in agreement with literature.[46]

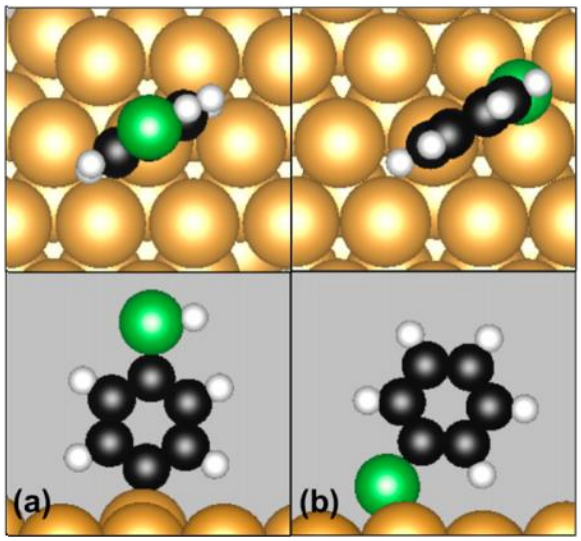

Figure 3.3. (Top) Top view and (bottom) side view of DFT-calculated minimum-energy structures for: (a) Au−C_6H_4−SH and (b) Au−S−C_6H_5 on Au(111). Gold, green, black and white spheres represent Au, S, C, and H atoms, respectively. Periodic images of the adsorbates have been removed.

The bonding sites, geometries and bonding energies for Au−S−C_6H_5 and Au−C_6H_4−SH on Au(111) are summarized in **Table 3.1**. The delocalized charge density of thiophenol

contributed to both the covalent bonding and van der Waals interactions.[121] We estimated the van der Waals interactions between thiophenol and Au(111) using the optB88-vdW functional. The calculated strength of the Au−C bond in the Au−C_6H_4−SH model was found to be ca. 0.4 eV stronger than that of the Au−S bond in the Au−S−C_6H_5 model, which demonstrated that the Au−C_6H_4−SH monolayers formed by the electroreduction were more stable than the Au−S−C_6H_5 SAMs on Au surfaces.

Table 3.1. DFT calculated bonding Sites, geometries, and bond Energies (ΔE, in eV) for Au−C_6H_4−SH and Au−S−C_6H_5 on Au(111)

			RPBE		**OptB88-vdW**	
	site	**geometry**	**ΔE, 500eV** [a]	**ΔE, 750**	**ΔE, 500 eV**	**ΔE, 750**
Au−C_6H_4−SH	atop	upright	-1.22	-1.25	-2.31	-2.34
Au−S−C_6H_5	off-bridge	tilted	-0.76	-0.81	-1.94	-1.98
		Δ(ΔE)=	0.45	0.44	0.37	0.36

[a] 500 and 750 eV denote the cutoff energies in the DFT calculations. Δ(ΔE) is the energetic difference between tilted and upright geometries. The C−H and S−H bond energies in gas phase were calculated to be 5.24 and 3.66 eV using the optB88-vdW functional, and 4.94 and 3.44 eV using the RPBE functional.

Santiago-Rodriguez et al. calculated binding energies of various molecules on Au(111) using the PW91 and RPBE functionals, respectively.[122] They found that the strength of the Au-C bond was stronger than that of the Au-S bond by ca. 0.5 eV, which is similar to our calculated number (0.4 eV) using the optB88-vdW functional. In our models, the calculated energies using a 750 eV cutoff energy and 8 × 8 × 1 k-point grid were only more negative than that using a 500 eV cutoff energy and 7 × 7 × 1 k-point grid by < 0.05 eV, indicating that the calculations using a 500 eV cutoff energy and 7 × 7 × 1 k-point grid were well converged. Our calculations are accurate enough. The calculated bond energies using the optB88-vdW functional were ca. 1.1 eV stronger than that using the RPBE functional, indicating that thiophenol molecules interacted

with gold through strong vdW forces. The calculated vibrational frequency of the Au−C bond in the Au−C_6H_4−SH model was 444 cm^{-1}, which demonstrated that the 415 cm^{-1} in **Figure 3.2b** was the characteristic band of the Au−C stretching.

3.2. Nitrogen compound on Au: Adenine

3.2.1. Experimental findings

Bocarsly et al. reported that pyridinium ions catalyzed the reduction of CO_2 to methanol in electrochemical reactions.[30-32] They proposed that the electrons for CO_2 reduction were transferred from pyridinium ions to CO_2 molecules through the N atoms in the ions.[31] Adenine molecule shares a similar molecular structure with pyridinium ion, and the number of N atoms in adenine molecule is larger than that in pyridinium ion. Thus, the modification of electrodes with adenine is likely to promote electrochemical CO_2RR.

Acres et al. prepared adenine films on Au(111) surfaces in vacuum and aqueous solution, respectively.[123] In vacuum, the adenine films were deposited by a evaporator at room temperature. In solution, the deposition of adenine on Au(111) was prepared by placing a few drops of adenine saturated solution on the surface of a gold crystal.

The near edge X-ray absorption fine structure (NEXAFS) spectra of adenine films on Au(111) are shown in **Figure 3.4**. The grazing incidence (GI) and normal incidence (NI) photon beam excited the electronic states perpendicular to the surface and the in-plane electronic states, respectively. The peaks at 399.6 (I)[124] and 401.2 (II)[125] eV reflected the π* resonances at nitrogen K-edge. The peaks at 286.8 (V)[124] and 287.4 (VI)[126] eV reflected the π* resonances at carbon K-edge. In vacuum, the peaks I, II, V and VI disappeared on the red line, indicating that adenine planes were parallel to the Au(111) surface.

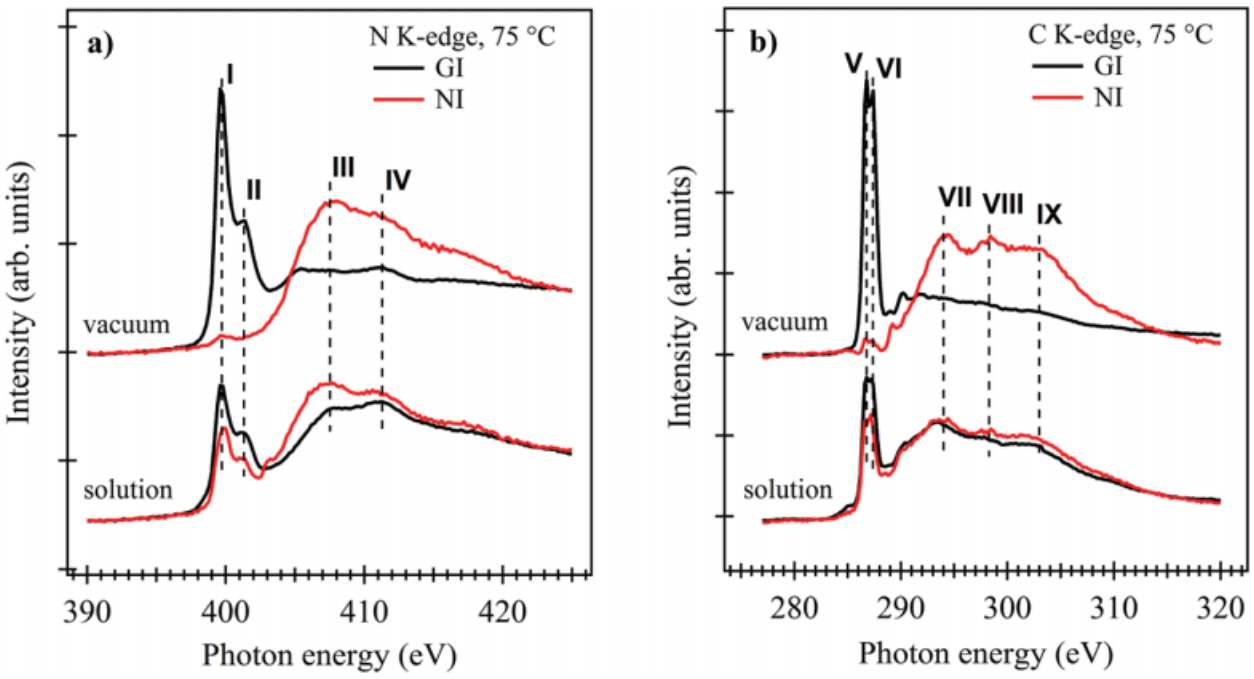

Figure 3.4. NEXAFS spectra of adenine on Au(111) in vacuum and solution at (a) N K-edge; (b) C K-edge after annealing at 75 °C. Red and black lines represent NI and GI, respectively.

The core band spectra of adenine on Au(111) are shown in **Figure 3.5**. The peaks at 400.2 (A) and 398.6 (B) eV corresponded to the binding energies of amino (-NH-, -NH_2) and imino (-N=) groups.[127] The peaks at (C), (D) and (E) showed the binding energies of five C atoms. The peaks at 286.6 (C) and 284.9 (E) eV were linked to binding energies of the C6 and C5 atoms (see **Figure 3.6** for the location of each C atom), respectively. The peak at 286.0 eV (D) corresponded to binding energies of C2, C4 and C8 atoms.[128, 129] In vacuum, all of peaks disappeared after annealing the adenine films at 125 °C, indicating that adenine molecules desorbed from the surface at 125 °C.

The deposition in solution gave residual carbon contamination on Au surfaces, which caused the appearance of peak (F) in **Figure 3.5d**. Compared to the core band spectra of adenine/Au(111) in vacuum, the core band spectra of adenine/Au(111) in solution gave higher

peaks at 125 and 150 °C, indicating that the binding of adenine films on Au(111) in solution were more stronger than that in vacuum.

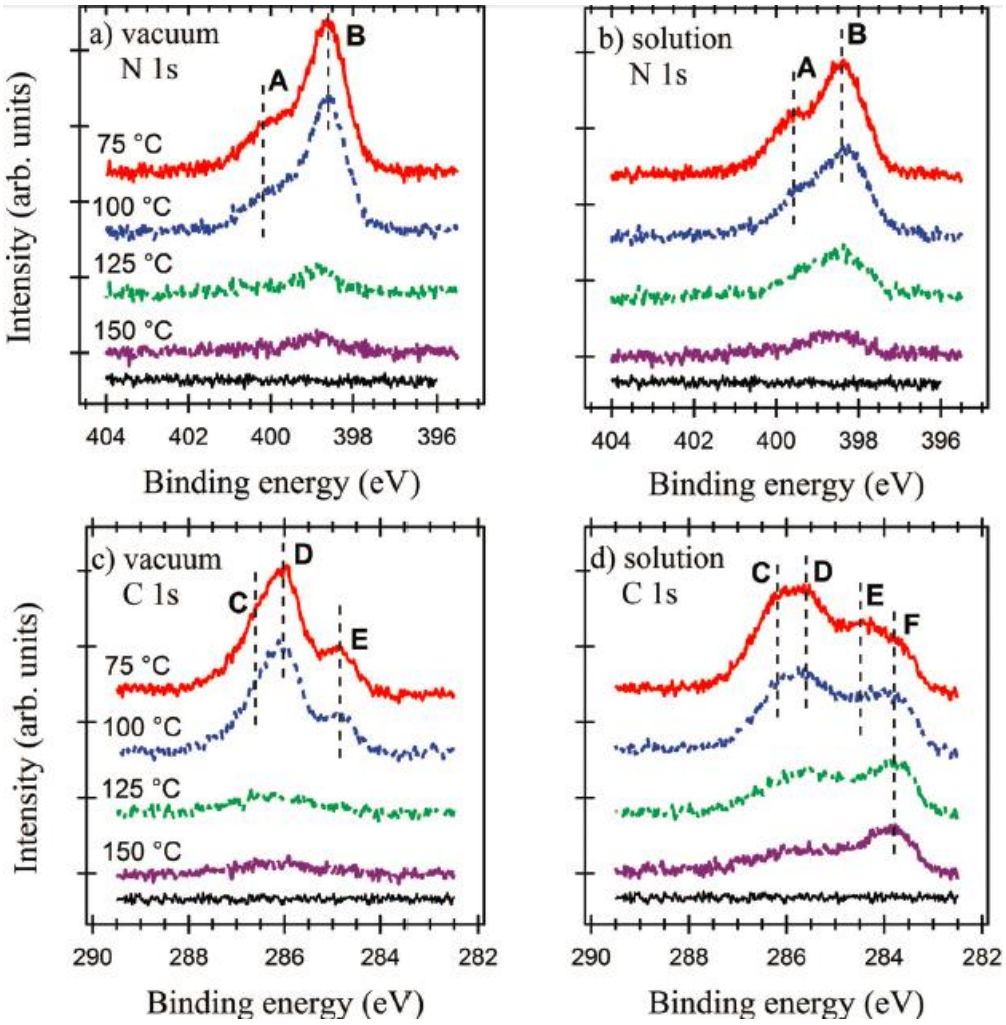

Figure 3.5. Core band spectra of adenine films on Au(111) in vacuum (a and c) and solution (b and d) after annealing at indicated temperatures. The black line is the spectrum of the clean Au(111).

In **Figure 3.4**, the peaks on the solution black line (GI) are similar to that on the solution red line (NI), indicating that the π* resonances in solution are not strongly dependent on the angle of the incidence. The adenine films were disordered in aqueous solution, and adenine planes had various orientations on the Au surfaces.

3.2.2. Theoretical results

We investigated the adsorption energies and configurations of adenine molecules on Au(111) using DFT methods. The N9H tautomer (**Figure 3.6**) was found to be the most stable form of adenine in the gas phase.[130] Thus, we modeled the N9H tautomer on Au(111) in several parallel and upright geometries. In parallel geometries, the center of the 6-member ring of the N9H tautomer was placed on high-symmetry surface sites, such as bridge, top, fcc and hcp sites. The orientations of the N9H tautomer were changed by rotating the molecule 0, 30, 60, 90, 120 and 150° clockwise.

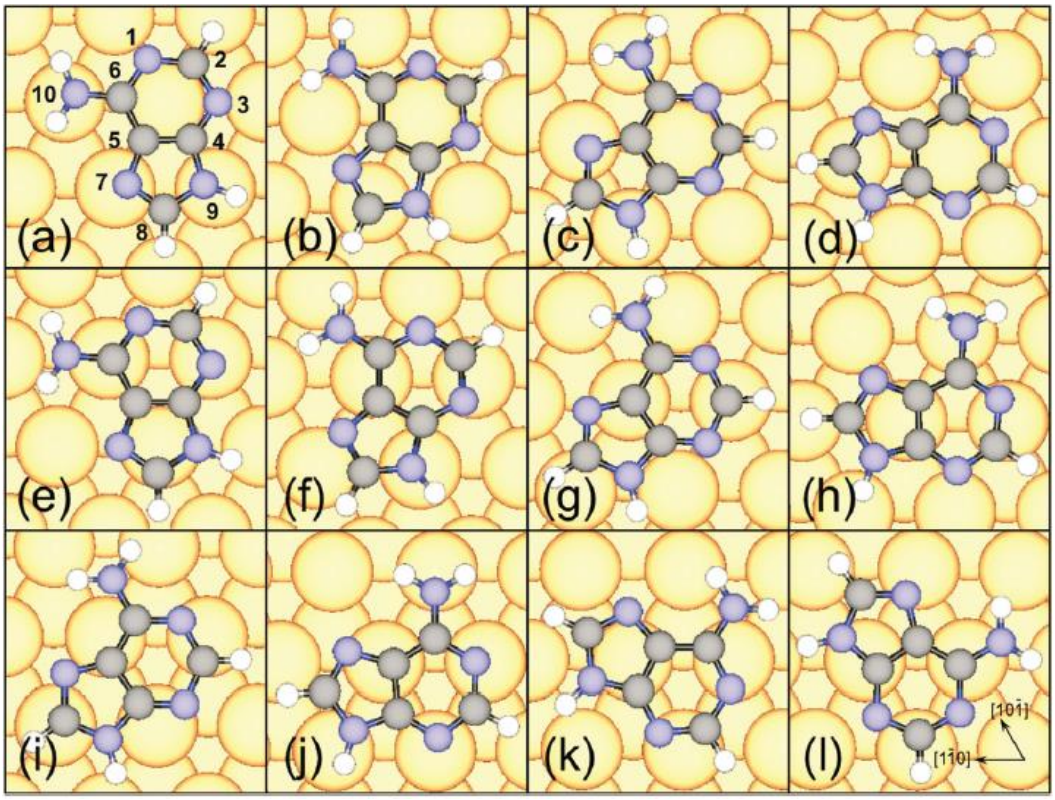

Figure 3.6. Top view of calculated minimum-energy parallel geometries of N9H adenine on Au(111): (a) top0; (b) top30; (c) top60; (d) top90; (e) br0; (f) br30; (g) br60; (h) br90; (i) fcc60; (j) fcc90; (k) fcc120; (l) fcc150. The location of each atom is shown in (a), and the surface directions are indicated in (l). Gold, black, blue and white spheres represent Au, C, N and H atoms, respectively. Periodic images of the adsorbates have been removed.

The calculated adsorption energies of adenine on Au(111) are shown in **Table 3.2**. The adsorption energies of N9H adenines in parallel geometries were calculated to be ca. 0 eV using the RPBE functional, indicating that adenines in parallel geometries interacted with the surface weakly. The orientation of N9H adenines in parallel geometries had negligible effect on the adsorption energies.

Table 3.2. Adsorption energies (ΔE_{ads}, eV) of adenine on Au(111) in various modes. The geometries of adenine molecules are indicated. Coverage is 1/9 ML except where noted.

Adsorption modes	GGA-RPBE 500 eV	GGA-RPBE 750 eV[a]	optB86b-vdW 500 eV	optB86b-vdW 750 eV[a]
N9H (parallel geometry)				
top0 (= top120)	0.00	+0.04	-1.18	-1.17
br60	−0.01	+0.02	-1.14	-1.14
fcc0 (= fcc120)	+0.01	+0.05	-1.13	-1.13
hcp0 (= hcp120)	0.00	+0.03	-1.15	-1.14
hydrogen-bonded parallel chain[b]	-0.40	-0.40	-1.66	-1.66
N9H (upright geometry)				
N1	+0.06	+0.12	-0.82	-0.76
N3	-0.12	-0.09	-1.09	-1.01
N3 (N9H dissociated)	+0.87	+1.03	-0.49	-0.28
N7	+0.06	+0.11	-0.82	-0.79
N3H (upright geometry)				
N9	+0.08	+0.15	-0.94	-0.86
N9[c]	-0.21	-0.14	-1.24	-1.16
N7H (upright geometry)				
N3,N9	+0.46	+0.51	-0.47	-0.39
N3,N9[c]	+0.14	+0.19	-0.80	-0.73

[a] The structures of adsorbates were optimized using 500 eV cutoff energy, and the optimized structures were frozen in calculations at 750 eV cutoff energy. [b] Calculated on the surface with (4 × 4) unit cell (coverage is 1/8 ML). [c] The gas phase adenine were N3H or N7H tautomer.

The ΔE_{ads} of N9H adenines in parallel geometries were calculated to be in the range of -1.13 to -1.18 eV using the optB86b-vdW functional. The calculated distance between N atoms of parallel adenine molecules and the un-relaxed Au(111) surfaces was 3.42 ± 0.11 and $3.89 \pm$

0.16 Å using the optB86b-vdW and RPBE functionals, respectively. We also modelled hydrogen-bonded adenine chains on Au(111) with a 4×4 surface unit cell (the surface coverage is 1/8 ML). The ΔE_{ads} of the adenine chains was found to be ca. 0.5 eV more stable than that of an isolated adenine molecule. In experiments, the hydrogen-bonded adenine chains were observed at a temperature lower than 25 °C using the STM technique.[131-133] At a temperature higher than 25 °C, adenine molecules are mobile on Au(111) surfaces,[132] instant intermolecular hydrogen bonding is hardly to be observed using the STM technique.

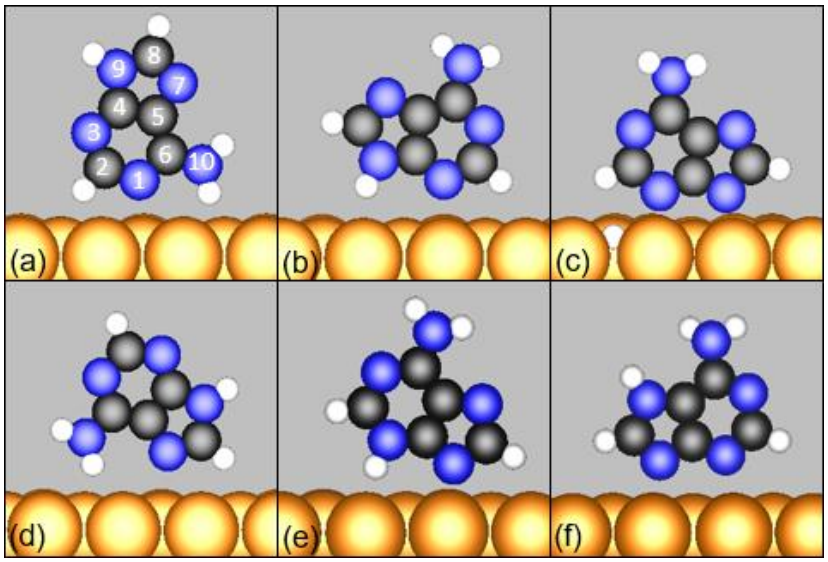

Figure 3.7. Side view of calculated minimum-energy upright geometries of adenine on Au(111): for N9H tautomer – (a) N1; (b) N3; (c) N3 with H on N9 dissociated to the surface; (d) N7; for N3H tautomer – (e) N9; for N7H tautomer – (f) N3, N9. Gold, black, blue and white spheres represent Au, C, N and H atoms, respectively. For clarity, periodic images of the adsorbates have been removed.

Adenine molecules in upright configurations adsorbed on top sites of surface Au atoms (**Figure 3.7**). The N9H tautomer bonded to the Au(111) surface through the N1, N3, and N7 atoms, respectively (**Figure 3.7a,b and d**). Among these three geometries, the N3 adsorption mode was the most stable one with a ΔE_{ads} of -1.01 and -0.09 eV using the optB86b-vdW and

RPBE functionals, respectively. **Figure 3.7c** showed the dissociation of acidic hydrogen from the N9 site of the N3 adsorption mode. The dissociation was very difficult with a reaction energy of 0.73 eV (optB86b-vdW) or 1.12 eV (RPBE).

Based on the classic analysis developed by Redhead[134] (parameters are: heating rate 10 °C s^{-1}, initial surface coverage 1/9 ML, desorption prefactor 10^{13} s^{-1}, first-order desorption reaction), a ΔE_{ads} of -1.0 to -1.2 eV meant that the desorption reactions took place at temperatures 112–147 °C, which were in agreement with the reported desorption temperatures 125-150 °C in literature.[133] The adsorption energy of the N9H tautomer (N3 adsorption mode) on Au(111) was calculated to be -1.01 eV using the adaptive sum method[91], indicating that the N9H tautomer interacted with the Au(111) surface through strong vdW forces. The ZPE contribution to adsorption energy was less than 0.02 eV in each adsorption mode, which demonstrated that ZPEs were negligible in calculations.

In the gas phase, the N3H and N7H tautomers were found to be less stable than the N9H tautomer by 0.29 and 0.32 eV using the RPBE functional, respectively. The energetic differences became 0.30 and 0.34 eV using the optB86b-vdW functional, which were consistent with the values published in literature.[130] Based on Arrhenius equation, the number of the N9H tautomer was 10 times as large as that of other tautomers at room temperature.

The adsorption of adenine on Au(111) would change the energies of adenine molecules. Thus, we calculated the adsorption energies of N3H and N7H modes (**Table 3.2**). Assuming the adenine molecules in the gas phase were the N9H tautomers, the adsorption energies of the N3H, N7H and N9H tautomer on Au(111) were calculated to be +0.15, +0.51 and -0.09 eV using the RPBE functional, respectively. The adsorption energies became -0.86, -0.39 and -1.01 eV using

the optB86b functional. The N9H tautomer was found to be the most stable adsorbed species among three tautomers.

On the other hand, Assuming the adenine molecules in the gas phase were the N3H tautomers, the adsorption energy of the N3H tautomer on Au(111) was calculated to be -0.14 and -1.16 eV using the RPBE and optB86b functionals, respectively. In that case, the adsorbed N3H tautomer would be more stable than the adsorbed N9H tautomer on Au(111).

3.3. Electrochemical stability of thiolate on Au: 2-PET

3.3.1. Theoretical analysis

Fang et al. reported that the 2-PET modified Au electrode exhibited excellent catalytic activity and selectivity for the CO evolution in electrochemical CO_2RR.[83] We would like to understand whether the 2-PET molecules were stable on the electrode or not. We investigated the stability of 2-PET on Au surfaces using DFT methods.

The thiolic S-H bonds break easily with low barriers (0.3-0.4 eV)[49, 50] and the generated H radicals react to desorb as H_2[135]. As a result, thiols adsorb on Au surfaces through strong S-Au covalent bonds at ambient conditions.[52, 136] Thus the physisorption of thiols on Au was not considered in our calculations. Three chemisorbed thiolate states of 2-PET are directly adsorbed thiolates (2-PETt), monothiolate-Au complexes ((2-PETt)Au), and dithiolate-Au complexes ((2-PETt)$_2$Au). The DFT-calculated minimum-energy geometries of these thiolate states on Au terrace (Au(111)) and step sites (Au(211)) are shown in **Figure 3.8**. Consistent with literature, we modeled both 2-PETt and (2-PETt)$_2$Au at 1/3 ML on Au(111) (coverage based on the ratio of the number of S atoms to that of surface Au atoms in a surface unit cell). 2-PETt and (2-PETt)$_2$Au were placed on the Au(211) step edge at the highest edge coverage, and neighboring S atoms were not allowed to bond to the same Au atoms. (2-PETt)Au was modeled on the same

surface unit cell as $(2\text{-PETt})_2Au$, and was regarded as the intermediate product state of the desorption of $(2\text{-PETt})_2Au$ on Au surfaces.

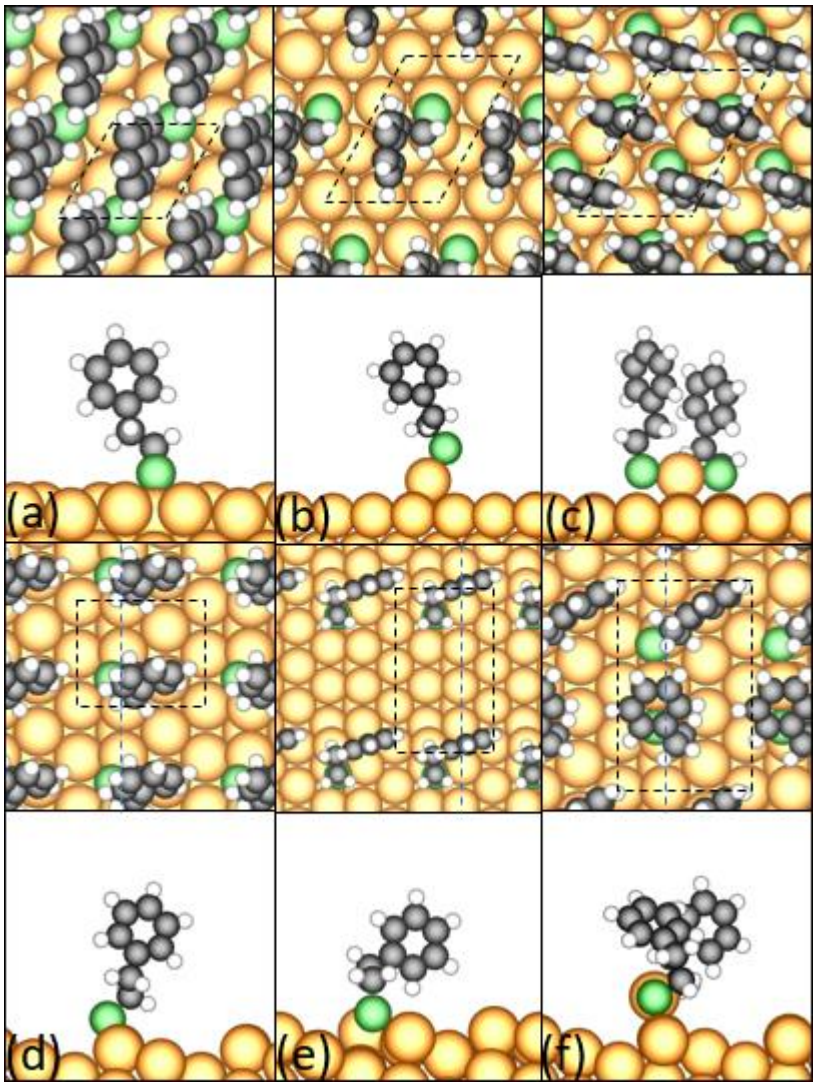

Figure 3.8. Top (top panels) and side (bottom panels) views of DFT-calculated minimum free energy geometries for, on Au(111), (a) 2-PETt on a ($\sqrt{3}\times\sqrt{3}$) R30° surface unit cell, (b) (2-PETt)Au on a (2×3) surface unit cell, and (c) $(2\text{-PETt})_2Au$ on a (2×3) surface unit cell; on Au(211), (d) 2-PETt on a (2×3) unit cell, (e) (2-PETt)Au on a (4×3) surface unit cell, and (f) $(2\text{-PETt})_2Au$ on a (4×3) surface unit cell. Yellow, green, black, and white spheres represent Au, S, C, and H atoms, respectively. Blue and black dashed lines in top views indicate step edge and surface unit cells, respectively. For clarity, periodic images of adsorbates have been removed from the side views.

Three possible desorption products were considered, i.e. the thiol (2-PET), the thiolate anion (2-PETt$^-$), and phenylethyl disulfide ($C_6H_5(CH_2)_2SS(CH_2)_2C_6H_5$). The geometries of these species as optimized in the gas phase are shown in **Figure 3.9**. The disulfide was found to be more stable in the *trans* configuration than in the *cis* configuration.

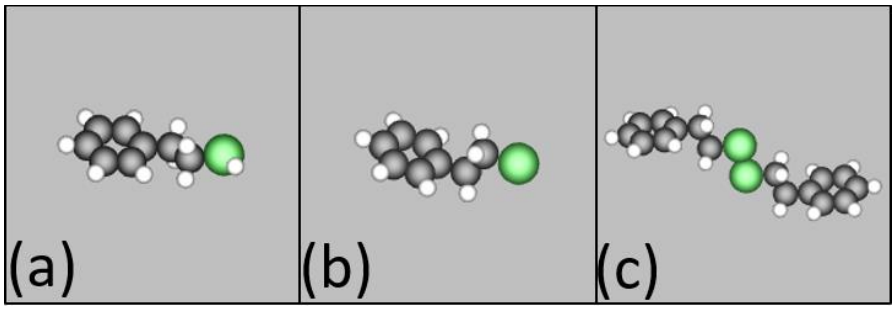

Figure 3.9. The DFT-calculated minimum-energy geometries of (a) 2-PET, (b) 2-PETt$^-$ and (c) phenethyl disulfide in gas phase with implicit solvation model. Green, black and white spheres represent S, C and H atoms, respectively.

The surface coverages of thiol species were set to be θ=1/3, 1/6 and 1/12 ML. Phenyl rings in all thiol species orient nearly vertical to the gold surfaces, which is attributed to the bent Au-S-C bond angle.[66] Two thiolate molecules linked by an Au adatom form dithiolate-Au complex (RS-Au-SR), and the "staple" motifs of dithiolate-Au complexes have been observed using STM technique.[137-139] For 2-PETt on Au(111), the S headgroups were located somewhere between the fcc-hollows and the bridge sites, which is in agreement with the literature.[61] For 2-PETt on Au(211), the S headgroups were located on the bridge sites of the step edges. For (2-PETt)Au on Au(111), the Au adatoms were located on fcc sites and the 2-PETts were on the top of the Au adatoms. For $(2\text{-PETt})_2$Au on Au(111), 2-PETts were on the top sites and Au adatoms were on the bridge sites. For (2-PETt)Au on Au(211), the Au adatoms were located on 3-fold hollow sites and the 2-PETts were on the top of the Au adatoms. For $(2\text{-PETt})_2$Au on Au(211),

the $(2\text{-PETt})_2Au$ complexes were aligned on the step edges with the S headgroups and the Au adatoms located on the top sites.

Based on these adsorbed states and desorption products, we considered the following adsorption/desorption steps:

$$2\text{-}PETt^* + H^+_{(aq)} + e^- = 2\text{-}PET_{(aq)} + * \quad (1A)$$

$$(2\text{-}PETt)_2Au^* + H^+_{(aq)} + e^- = 2\text{-}PET_{(aq)} + (2\text{-}PETt)Au^* \quad (1B)$$

$$(2\text{-}PETt)Au^* + H^+_{(aq)} + e^- = 2\text{-}PET_{(aq)} + Au^* \quad (1C)$$

$$2\text{-}PETt^* + e^- = 2\text{-}PETt^-_{(aq)} + * \quad (2A)$$

$$(2\text{-}PET)_2Au^* + e^- = 2\text{-}PETt^-_{(aq)} + (2\text{-}PETt)Au^* \quad (2B)$$

$$(2\text{-}PETt)Au^* + e^- = 2\text{-}PETt^-_{(aq)} + Au^* \quad (2C)$$

$$2(2\text{-}PETt^*) = (C_6H_5(CH_2)_2SS(CH_2)_2C_6H_5)_{(aq)} + 2* \quad (3)$$

The lines corresponding ΔG_{rxn}(U, pH)=0 eV for the steps above were plotted in **Figure 3.10**, which delineated the thermodynamically favorable and unfavorable (U, pH) phase space for each step. When there were two ΔG_{rxn}(U, pH)=0 eV lines for a given adsorbed state, the lower one showed the desorption potentials for that state. The aggregate of such boundary lines delineates the stability limit of an adsorbed state. Furthermore, since the activation barrier for electron or proton/electron transfer is small, the desorption of an adsorbed state took place without activation barrier.

Thermal desorption as disulfide (Step 3) was thermodynamically unfavorable (0.51 eV) under ambient conditions. Steps 1C and 2C of 2-PETt desorption from the monothiolate-Au complexes was found to occur at more positive potentials than 2-PETt desorption from the dithiolate-Au complexes (Steps 1B and 2B), which implied that the second thiolate in a

dithiolate-Au complex desorbed immediately after the desorption of the first thiolate in dithiolate-Au complex.

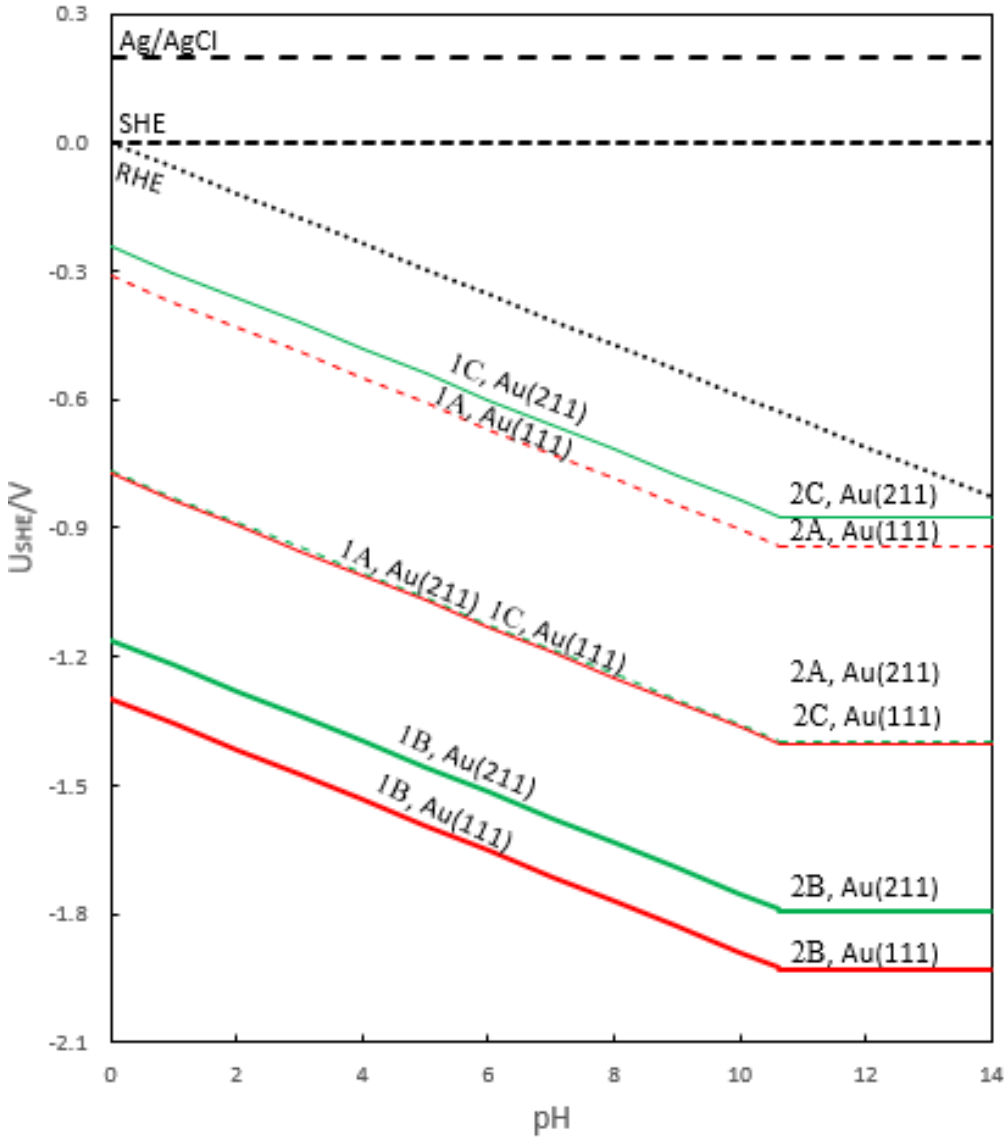

Figure 3.10. Calculated Surface Pourbaix diagram of 2-PETt on Au in aqueous solutions. The dashed lines indicate the respective reference electrodes, whereas the solid lines indicate ΔG_{rxn}(U, pH) = 0 eV for steps and Au facets as labeled.

The desorption lines for type 1 steps exhibit a slope of 59.2 mV/pH due to pH dependence at ambient temperature, whereas the desorption lines for type 2 steps are independent of pH because they do not involve proton transfer. The desorption lines for types 1 and 2 steps intersect at pH=10.65 for both 2-PETt* and $(2\text{-PETt})_2$Au, on Au(111) and Au(211), which is nearly exactly equal to the predicted pKa of 2-PET in aqueous solutions. Thus, the pKa of 2-PET demarcates the transition between desorption of 2-PET from Au as the neutral thiol and as the anionic thiolate, and determines the stability of the 2-PET/2-PET$^-$ couple in the aqueous phase.

At pH = 0, 2-PETt, 2-PETt of (2-PETt)Au complex, and 2-PETt of $(2\text{-PETt})_2$Au complex desorb from Au(111) and Au(211) surfaces at the potentials of -0.31 and -0.77 V, -0.77 and -0.92 V, and -1.3 and -1.0 V vs. SHE, respectively. At pH greater or equal to the pKa, 2-PETt, 2-PETt of (2-PETt)Au complex, and 2-PETt of $(2\text{-PETt})_2$Au complex desorb from Au(111) and Au(211) surfaces at the potentials of -0.94 and -1.40 V, -1.40 and -1.55 V, and -1.93 and -1.63 V vs. SHE, respectively. We compared the desorption potentials of step 1A on Au(111) with that of alkanethiol on Au(111) in experiments. Intriguingly, the desorption potentials of step 1A on Au(111) were similar to that of octanethiol on Au(111). The calculated desorption potentials of step 1A on Au(111) were -0.73 and -0.94 V vs. SHE at pH = 7 and 12, respectively. The experimental desorption potentials of octanethiol on Au(111) were -0.95 and -1.10 V vs. Ag/AgCl (which were equal to -0.75 and -0.90 V vs. SHE[140]) at pH = 7 and 12, respectively.[63] The experimental desorption potentials of alkanethiol on Au(111) shifted negatively and were not dependent on pH at pH < pKa and pH > pKa[63], respectively, which is similar to our simulated desorption potential line of step 1A on Au(111). The slop of the experimental

desorption potential lines at pH < pKa was estimated to be -33 mV/pH, which is different from the calculated value -59.2 mV/pH due to the corrosion of surfaces at small pH.

3.3.2. Experimental findings

The stability of thiolates on Au were examined using ex situ attenuated total reflectance infrared (ATR-IR) technique (**Figure 3.11**). In the spectra of 2-PET-Au, the shape of each peak of the post-electrolysis sample was similar to that of the fresh sample, indicating that 2-PET thiolates were stable on the surfaces during the electrochemical reactions. The peaks iii and iv (the characteristic peaks of C=C vibration in phenyl group[141]) increased in intensities and the peak i (the characteristic peak of $–CH_2–CH_2–$ vibration[142]) shifted after the electrolysis reactions at -1.1 V vs. RHE, which were due to the conformational change of the 2-PET thiolates.[143] In the spectra of 2-MPA-Au, the peak vi (the characteristic peak of C-C vibration[142]) disappeared and the peaks ii, iii and v (the characteristic peaks of -COO group vibration[144-148]) increased in intensities after the electrolysis reactions at -0.94 V vs. RHE, indicating that the -COOH group in the 2-MPA thiolate was converted to the -COO group at -0.94 V vs. RHE. The CO_3^{2-} and HCO_3^- species in the solution can not change the intensities of peaks ii, iii and v in the spectra.[149, 150] The ATR-IR spectra demonstrated that 2-PETt and 2-MPAtt were stable on Au electrodes down to -0.9 V vs. RHE, and 2-MPAtt desorbed from the surfaces at -1.0 V vs. RHE.

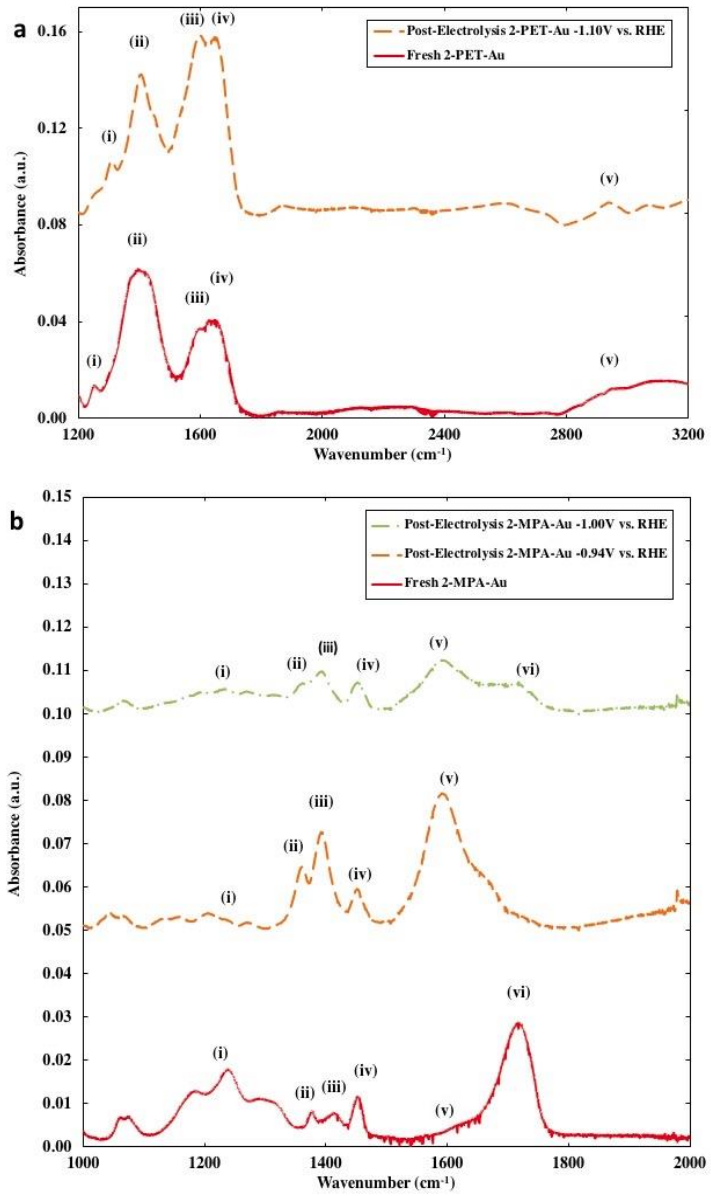

Figure 3.11. ATR-IR spectra for fresh and post-electrolysis (a) 2-PET-Au and (b) 2-MPA-Au electrodes. The electrolysis reactions were conducted in CO_2-saturated 0.1 M $KHCO_3$ solution for 15 minutes.

We postulated that voltammetry technique only measured the desorption potentials of directly adsorbed thiolate species on Au(111) surfaces, whereas the thiolate species persist on surfaces as Au-dithiolate complexes at much negative potentials, which has an effect on the catalytic activities of Au surfaces.

3.4. Electrochemical CO_2 reduction reaction on thiolated-Au

3.4.1. Experimental findings

Fang et al. prepared the thiolate-modified Au by immersing Au foils in a 20 mM ethanolic solution of thiol. The electrolysis of CO_2 was conducted in a three-electrode cell using 0.1 M $KHCO_3$ as electrolyte at room temperature and a CO_2 pressure of 1 atm. The cathode and anode were separately placed in a two-compartment glass reactor. A Nafion membrane was used to prevent the transfer of products from one compartment to another. Counter electrode was fabricated from platinum.

The onset potentials for CO_2RR and HER were determined using Tafel plots[151], and were summarized in **Table 3.3**. The onset potential of CO_2RR on blank Au was measured to be -0.33 V vs. RHE, which was in agreement with previous experimental results.[14] The onset potentials of CO_2RR on both the 2-PET-Au and 2-MPA-Au were measured to be -0.24 V vs. RHE, which were 90 mV more positive than that on the blank Au. The onset potentials of HER on the 2-MPA-Au was 160 mV more positive than that on the blank Au, whereas the onset potentials of HER on the 2-PET-Au was similar to that on the blank Au. The 2-MPA-Au and 2-PET-Au promoted HER and CO_2RR, respectively.

Table 3.3. The onset potentials (in V_{RHE}) of HER and CO_2RR on blank and functionalized Au electrodes at room temperature (Tafel plots analysis).

Electrode	HER	CO_2RR
blank Au	-0.27	-0.33
2-PET-Au	-0.26	-0.24
2-MPA-Au	-0.11	-0.24

The FE and partial current densities of CO and H_2 are shown in **Figure 3.12**. The total current density on blank Au was comparable to that on bulk Au in literature.[17] In the potential range of -0.6 to -0.9 V vs. RHE, the FE of CO on 2-PET-Au was twice as large as that on blank Au, whereas the FE of H_2 on 2-PET-Au was half of that on blank Au. At -0.9 V vs. RHE, the current density and FE of CO on 2-PET-Au were comparable to that on the anodically modified Au in literature.[12]

On the other hand, the FE of CO was suppressed and the FE of H_2 was enhanced on 2-MPA-Au in the potential range of -0.6 to -0.75 V vs. RHE. The current density of H_2 on 2-MPA-Au was larger than that on blank Au at a potential more negative than -0.9 V vs. RHE. The experimental results showed that Au electrodes were not poisoned by the adsorbed thiols at certain electrode potentials.

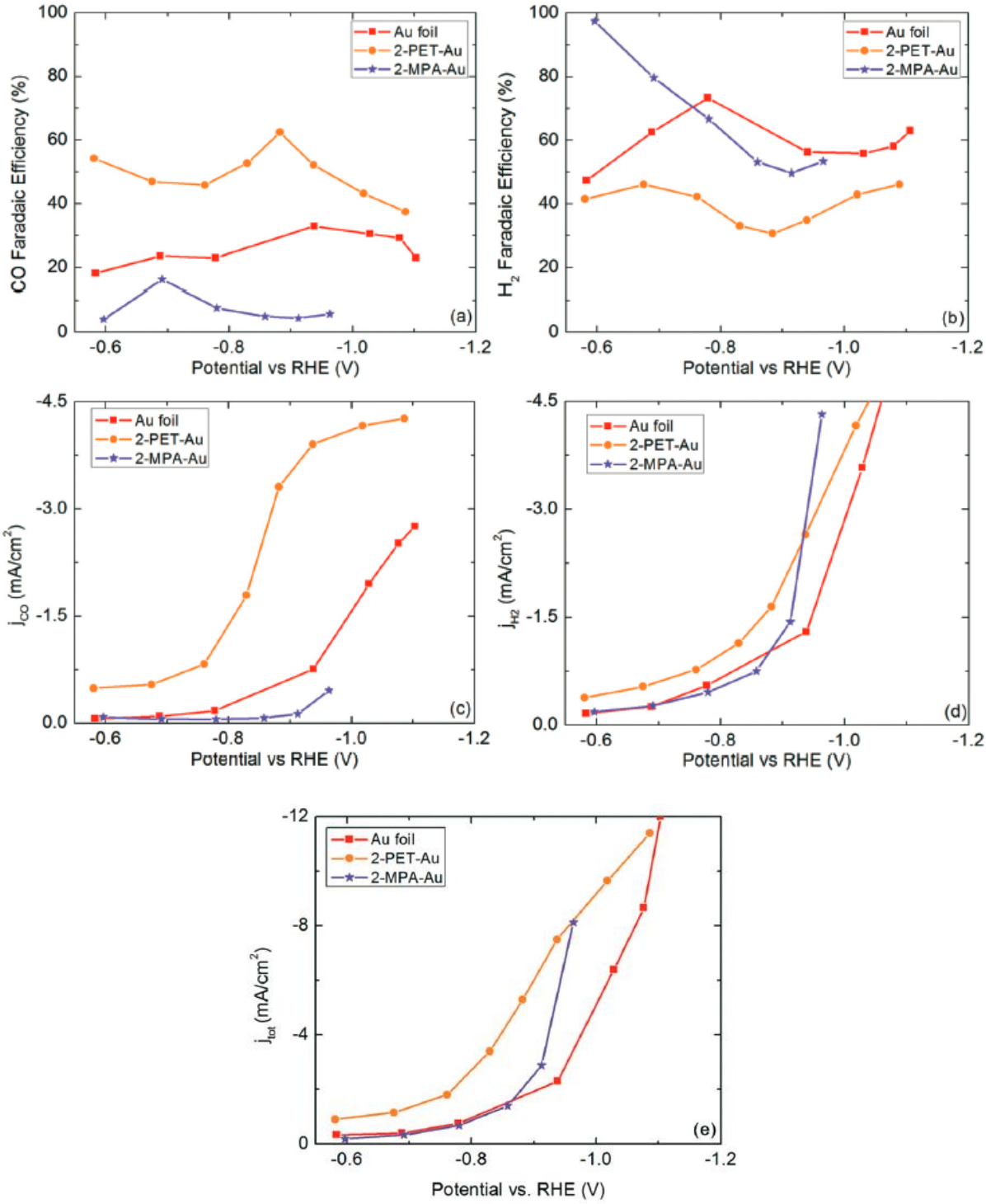

Figure 3.12. The CO_2RR and HER behavior on blank and thiol-functionalized Au electrodes in CO_2-saturated 0.1 M $KHCO_3$ solution at p_{CO_2} = 1 atm and room temperature. (a) Faradaic efficiency of CO; (b) Faradaic efficiency of H_2; (c) partial current density of CO (j_{CO}); (d) partial current density of H_2 (j_{H2}); (e) total current density (j_{tot}). To compare the partial current densities of CO and H_2, the y-axis scales are made identical in images (c) and (d).

3.4.2. Theoretical analysis of CO_2RR on blank Au

Previous research work showed that under-coordinated Au atoms were more active than high-coordinated Au atoms in catalytic reactions.[152-154] We studied the Au atoms' effects on CO_2RR and HER by investigating the catalytic activities of CO_2RR and HER on various Au sites. The model surfaces of Au(111), Au(100), Au(211), and Au(563) contain hexagonal close-packed terrace sites (coordination number is 9), square close-packed terrace sites (coordination number is 8), step edge sites (coordination number is 7) and corner sites (coordination number is 6), respectively.[155]

The reactions of CO_2RR and HER on Au surfaces were written as below[42, 156]:

$$CO_{2(g)} + H^+_{(aq)} + e^- + * \rightarrow COOH^* \quad (3.1)$$

$$COOH^* + H^+_{(aq)} + e^- \rightarrow CO^* + H_2O_{(aq)} \quad (3.2)$$

$$CO^* \leftrightarrow CO_{(g)} + * \quad (3.3)$$

$$H^+_{(aq)} + e^- + * \rightarrow H^* \quad (3.4)$$

We calculated the equilibrium potentials of the above four reactions. Among reactions (3.1), (3.2) and (3.3), the calculated lowest equilibrium potential was equal to the limiting potential of CO_2RR. The equilibrium potential of reaction (3.4) was equal to the limiting potential of HER. Many scientists have determined the limiting potential of CO_2RR and HER using equilibrium potentials.[19, 20, 157] The desorption of CO from Au surfaces (reaction (3.3)) was thermodynamically favorable below 300K in experiments[158, 159], indicating that the reaction (3.3) was not the limiting reaction. The equilibrium potentials of reaction (3.1) and (3.2) were calculated to be negative and positive, respectively. Thus, the limiting potential of CO_2RR was equal to the equilibrium potential of reaction (3.1). The transfer of a pair of proton and electron

to an oxygen atom requires a small kinetic barrier.[105, 109] The minimum free energy geometries for H, COOH and CO on Au surfaces are shown in **Figure 3.13**.

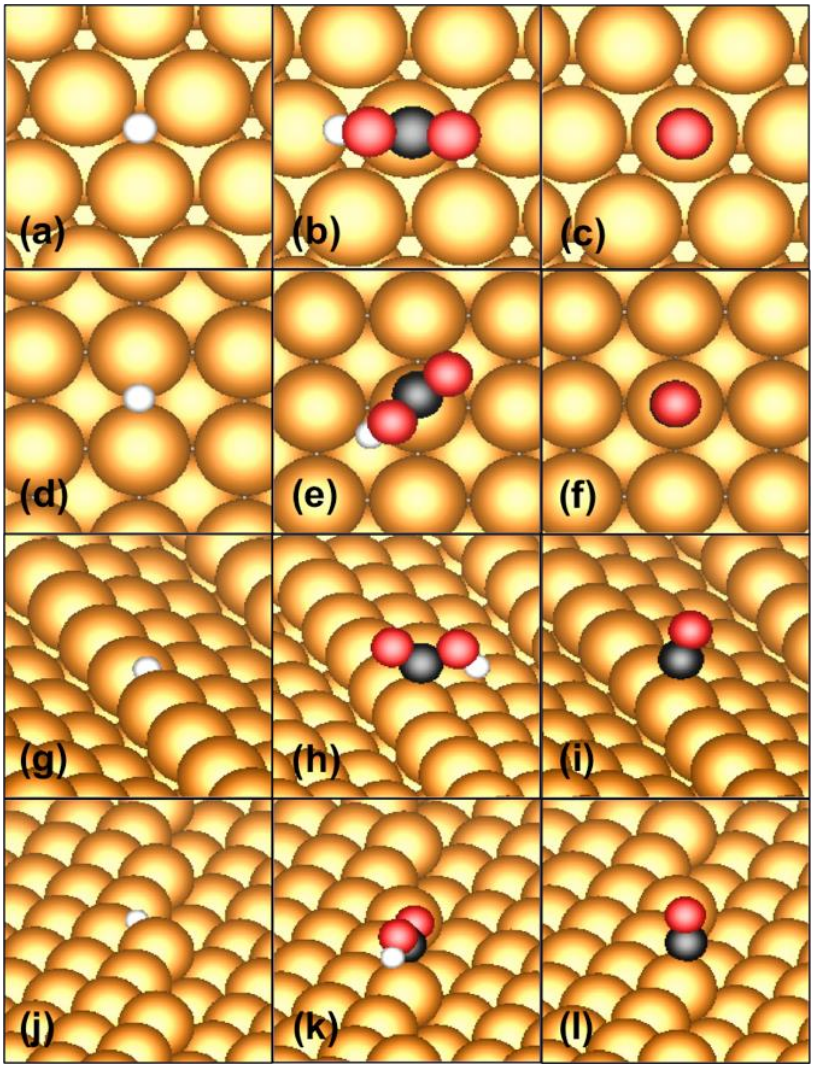

Figure 3.13. DFT-calculated minimum free energy geometries for H, COOH and CO on (a, b and c) Au(111), (d, e and f) Au(100), (g, h and i) Au(211) and (j, k and l) Au(563), respectively. Yellow, black, red and white spheres represent Au, C, O and H atoms, respectively. For clarity, periodic images of adsorbates have been removed.

CO molecules prefer to adsorb on the top sites of Au atoms.[155] The DFT total energy of COOH in cis configuration is similar to that of COOH in trans configuration. The electric field

(-1.0 V/Å[109]) on the interfaces stabilized the *COOH intermediate by -0.25 eV, and made the acidic proton of the *COOH to point toward the surfaces.

Table 3.4. The calculated limiting potentials of HER and CO_2RR on various blank Au sites. The energetic differences between CO_2RR and HER are listed.

	surface unit cell	HER	CO_2RR	diff.
Au(111)	(3×3)	-0.34	-0.66	-0.32
Au(100)	(3×3)	-0.35	-0.63	-0.28
Au(211)	(4×3)	-0.22	-0.35	-0.13
Au(563)	9 Au/layer	-0.23	-0.26	-0.03

Results are based on minimum free energy configurations for one *H or *COOH per surface unit cell.

Table 3.4 showed the calculated limiting potentials on Au(111), Au(100), Au(211), and Au(563), respectively. The calculated limiting potentials for CO evolution on Au(111) and Au(100) are ca. -0.65 V vs. RHE, whereas the limiting potentials on Au(211) and Au(563) are ca. -0.3 V vs. RHE. The calculated limiting potentials for CO evolution were consistent with the reported potentials in literature.[18, 19] We found that the energetic difference between the limiting potentials of HER and CO_2RR was only 0.03 eV on Au(563), whereas the difference was 0.32 eV on Au(111). The promotion of CO_2RR was significant on high-index Au facets.

3.4.3. Theoretical analysis of CO_2RR on thiol-modified Au

Figure 3.14 shows the DFT calculated reaction free energy diagram for CO_2RR on Au(111), Au(211), and $(2\text{-PETt})_2Au$/Au(211), respectively. The limiting potential of CO_2RR on $(2\text{-PETt})_2Au$/Au(211) is lower than that on blank Au(111).

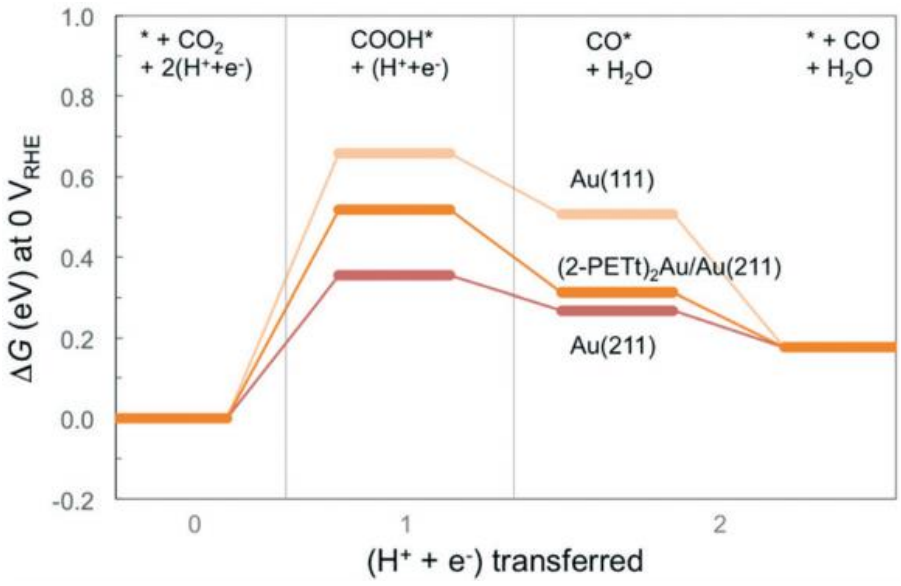

Figure 3.14. DFT calculated reaction free energy diagram for electrochemical CO_2RR on blank Au(111), blank Au(211), and $(2\text{-PETt})_2Au$/Au(211), respectively.

The calculated adsorption energies, ZPEs, Gibbs free energy contributions, solvation energies and dipole moments of thiolate species on Au surfaces are shown in **Table 3.5**. The thiolates are mobile on Au surfaces.[122, 160] The calculated results showed that RS and $(RS)_2Au$ thiolate species preferred to adsorb on the edge sites of the Au(211) rather than the terraces of the Au(111). At a negative electrode potential, thiolate species on defect sites (Au(211)) are more stable than that on terrace sites (Au(111)).

Table 3.5. DFT-calculated adsorption energies (ΔE_{ads}, eV), zero-point energies (E^{ZPE}, eV), free energies corrections ($\Delta G(T)$, eV, T = 298.15 K, p = 1 bar), solvation energies (ΔE_{solv}, eV), and dipole moments at zero fields (μ_0, eÅ) for various species.

Species			ΔE_{ads}	E^{ZPE}	$\Delta G(T)$	ΔE_{solv}	μ_0
H_2	gas phase			0.27	-0.05		
CO_2	gas phase			0.31	-0.30		
H	Au(111)	(3×3)	-2.08	0.13	0.13		0.00
	Au(100)	(3×3)	-2.06	0.16	0.15		+0.04
	Au(211)	(4×3)	-2.19	0.15	0.15		+0.02
	Au(563)	9/layer	-2.16	0.16	0.15		+0.04
COOH	Au(111)	(3×3)	-1.17	0.61	0.47	-0.25 [a]	+0.25
	Au(100)	(3×3)	-1.15	0.61	0.47	-0.25 [a]	+0.30
	Au(211)	(4×3)	-1.42	0.61	0.48	-0.25 [a]	+0.31
	Au(563)	9/layer	-1.50	0.61	0.47	-0.25 [a]	+0.33
2PETt, $C_6H_5(CH_2)_2S$	Au(111)	(2×2)	-1.38	3.96	3.71		-0.18
	Au(211)	(4×3)	-2.02	3.95	3.67		-0.27
	Au(211)	(2×3)	-1.91	3.95	3.65		-0.23
$(2PETt)_2Au$	Au(211)	(4×3)	-1.91 [b]	3.97 [b]	3.65 [b]		-0.45
	Au(211)	(3×3)	-1.71 [b]	3.98 [b]	3.66 [b]		-0.37
2MPAtt, $CH_3CHSCOO$	Au(111)	(2×2)	+0.19 [c]	1.83	1.60		+0.12
	Au(211)	(4×3)	-0.34 [c]	1.84	1.62		+0.32
	Au(211)	(2×3)	-0.21 [c]	1.84	1.62		+0.21
$(2MPAtt)_2Au$	Au(211)	(5×3)	-0.40 [b,c]	1.87 [b]	1.62 [b]		+0.31
	Au(211)	(4×3)	-0.37 [b,c]	1.86 [b]	1.60 [b]		+0.22

[a] The solvation energies of adsorbed COOH and CO are taken from Ref. [42] .

[b] Average energy of each thiolate.

[c] With respect to gas-phase CO_2 and CH_3CHS because $CH_3CHSCOO$ spontaneously dissociate into CO_2 and CH_3CHS in gas phase.

We named the directly adsorbed thiolates as 2-PETt and 2-MPAtt (the chemical formula of 2-MPAtt is $CH_3CHSCOO$); and the adsorbed dithiolate–Au complexes as $(2\text{-PETt})_2Au$ and $(2\text{-MPAtt})_2Au$. The thiolate coverage effects on the limiting potentials were considered. The coverage (θ) of thiolate species on Au surface was equal to the ratio of the number of thiolate-occupied Au edge atoms (an Au atom is occupied if it forms Au-S bond with thiolates) to the number of Au edge atoms in a unit cell. The calculated minimum free energy geometries of thiolate species on Au(211) are shown in **Figure 3.15**. The directly adsorbed thiolates preferred to adsorb on the bridge sites of step edges. The dithiolate-Au complexes were aligned on the step edges with the S headgroups and the Au adatoms located on the top sites, and the two thiolates were linked by the Au adatom. The adsorbed 2-PETt molecules tilted to the surfaces. The adsorbed 2-MPAtt molecules were bonded to the surfaces through both S and O atoms.

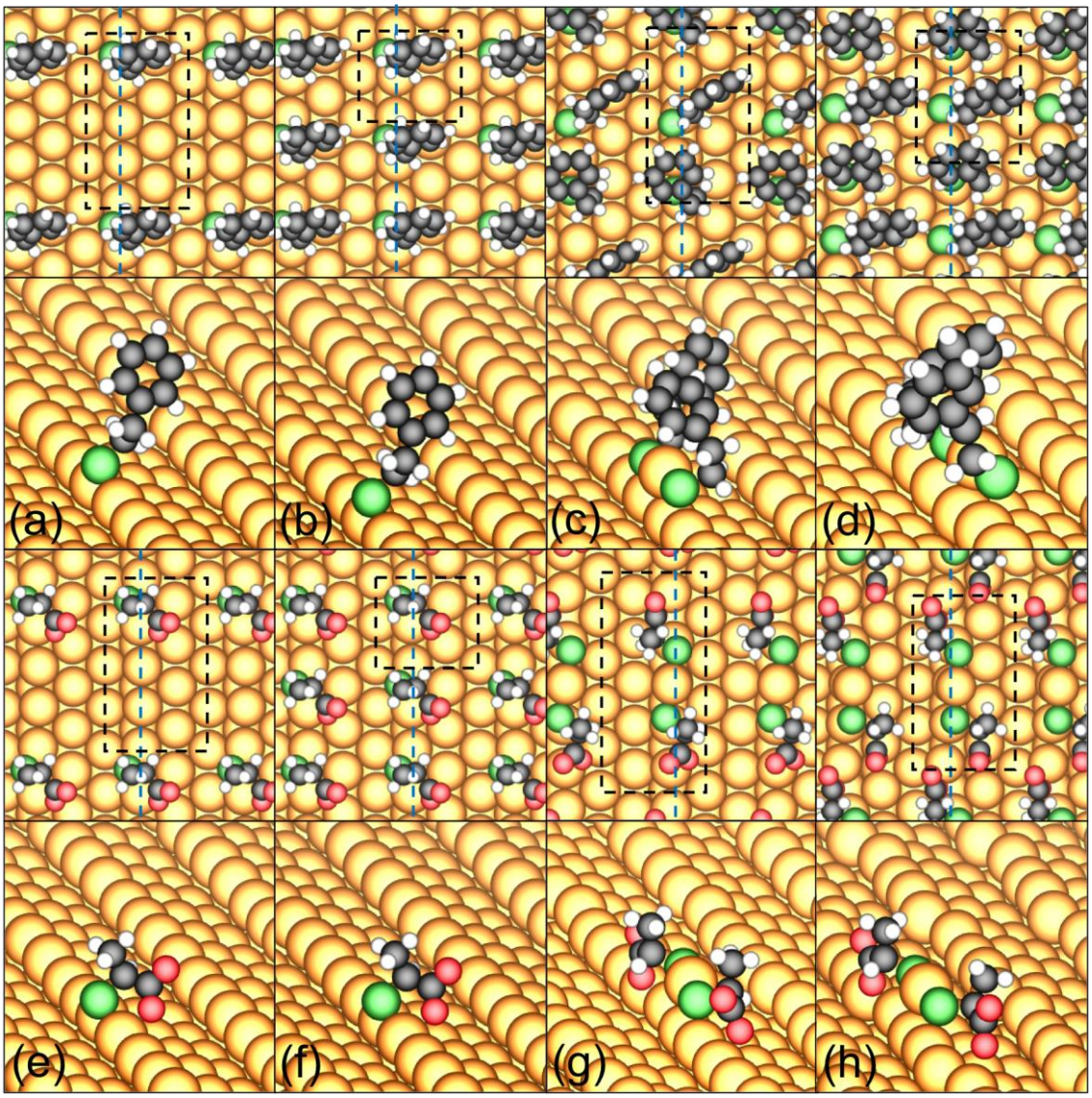

Figure 3.15. Top (top panels) and tilted side (bottom panels) views of DFT-calculated minimum free energy geometries of (a and b) 2-PETt on (4 × 3) and (2 × 3) unit cells; (c and d) (2-PETt)$_2$Au on (4 × 3) and (3 × 3) unit cells; (e and f) 2-MPAtt on (4 × 3) and (2 × 3) unit cells; (g and h) (2-MPAtt)$_2$Au on (5 × 3) and (4 × 3) unit cells, on step edges of Au(211) surfaces. Yellow, green, black, red and white spheres represent Au, S, C, O, and H atoms, respectively. Black and blue dashed lines indicate surface unit cells and step edges, respectively. For clarity, periodic images of adsorbates have been removed from the side views.

The calculated limiting potentials of CO_2RR and HER on thiolate-modified Au(211) were summarized in **Table 3.6**. The limiting potentials on thiolate-modified Au(211) were more negative than that on blank Au(211), which is due to the thiolate-induced destabilization of the intermediates *H and *COOH. The limiting potential of CO_2RR was below −1.0 V vs. RHE at the surface coverage of $\theta = 1$. The high surface coverage of 2-PETt would lead to the covalent interactions and Pauli repulsion[161-163] between atoms, and the lack of available edge sites for *COOH to adsorb on. At a $\theta=2/4$ surface coverage of 2-PETt, the limiting potential of CO_2RR on 2-PETt modified Au(211) was calculated to be -0.50 V vs. RHE, which was only 150 mV more negative than that on blank Au(211). At a $\theta=3/4$ surface coverage of $(2\text{-PETt})_2Au$, the limiting potential of CO_2RR on $(2\text{-PETt})_2Au$ modified Au(211) was calculated to be -0.52 V vs. RHE, which was only 170 mV more negative than that on blank Au(211). The limiting potentials of CO_2RR and HER on 2-MPAtt/Au(211) were more negative than that on 2-PETt/Au(211), which is due to the -COO group induced strong repulsion effects on the intermediates *H and *COOH.

Table 3.6. Calculated limiting potentials of HER and CO_2RR, energetic differences (in V_{RHE}) between CO_2RR and HER, sizes of surface unit cells, edge coverage (θ), chemical potentials of thiolates (μ, eV/RS), numbers of RS and Au edge atoms per unit cell (n_{RS}, n_{Au}), and the Boltzmann distribution (P, %, calculated at T=298.15 K and ε=-1.0 V/Å) for the various thiolate states on thiolate-functionalized Au(211) step edges.

	HER	CO_2RR	diff.	surface unit cell	θ	μ	n_{RS}, n_{Au}	P
2-PETt/Au(211)	**-0.31**	**-0.50**	-0.19	(4×3)	2/4	-0.59	1, 4	0
	-0.70	-1.80	-1.10	(2×3)	1	-0.54	1, 2	39
$(2\text{-PETt})_2Au$/Au(211)	-0.40	**-0.52**	-0.12	(4×3)	3/4	-0.55	2, 4	43
	-0.63	-1.21	-0.58	(3×3)	1	-0.38	2, 3	18
2-MPAtt/Au(211)	**-0.27**	**-0.65**	-0.38	(4×3)	2/4	-0.71	1, 4	1
	-0.75	-1.92	-1.17	(2×3)	1	-0.47	1, 2	14
$(2\text{-MPAtt})_2Au$/Au(211)	-0.62	-0.92	-0.30	(5×3)	4/5	-0.78	2, 5	18
	-0.69	-	-	(4×3)	1	-0.66	2, 4	67

Results are based on minimum free energy configurations of one thiolate species and one $^*H$ or $^*COOH$ per surface unit cell. Limiting potentials in bold are more positive than or equal to the limiting potentials on blank Au(111) from **Table 3.4**. "-" indicates $^*COOH$ is not stable on that surface.

In **Table 3.6**, the limiting potentials that are more positive than or equal to the limiting potentials on blank Au(111) were marked in bold. The probabilities of various thiolate species on Au(211) were calculated using the Boltzmann distribution equation ($P_i \propto e^{-\frac{\bar{g}_i}{kT}}$).

The average edge free energy $\bar{g}$ was calculated as below:

$$\gamma(T,e) = \left(\Delta E_{ads}^{211} + \Delta G(T)^{211} + \gamma_0^{211}\cdot e\right) - \left(\Delta E_{ads}^{111} + \Delta G(T)^{111} + \gamma_0^{111}\cdot e\right)$$

$$\bar{g}(T,e) = \frac{n_{RS}}{n_{Au}}\gamma$$

where ΔE_{ads}, $\Delta G(T)$ and μ_0 were obtained from **Table 3.5**. In **Table 3.6**, $(2\text{-PETt})_2Au$ is the only thiolate species that promotes the CO_2RR at high surface coverages. The calculated minimum free energy geometries for intermediates on thiolate modified Au(211) are shown in **Figure 3.16**.

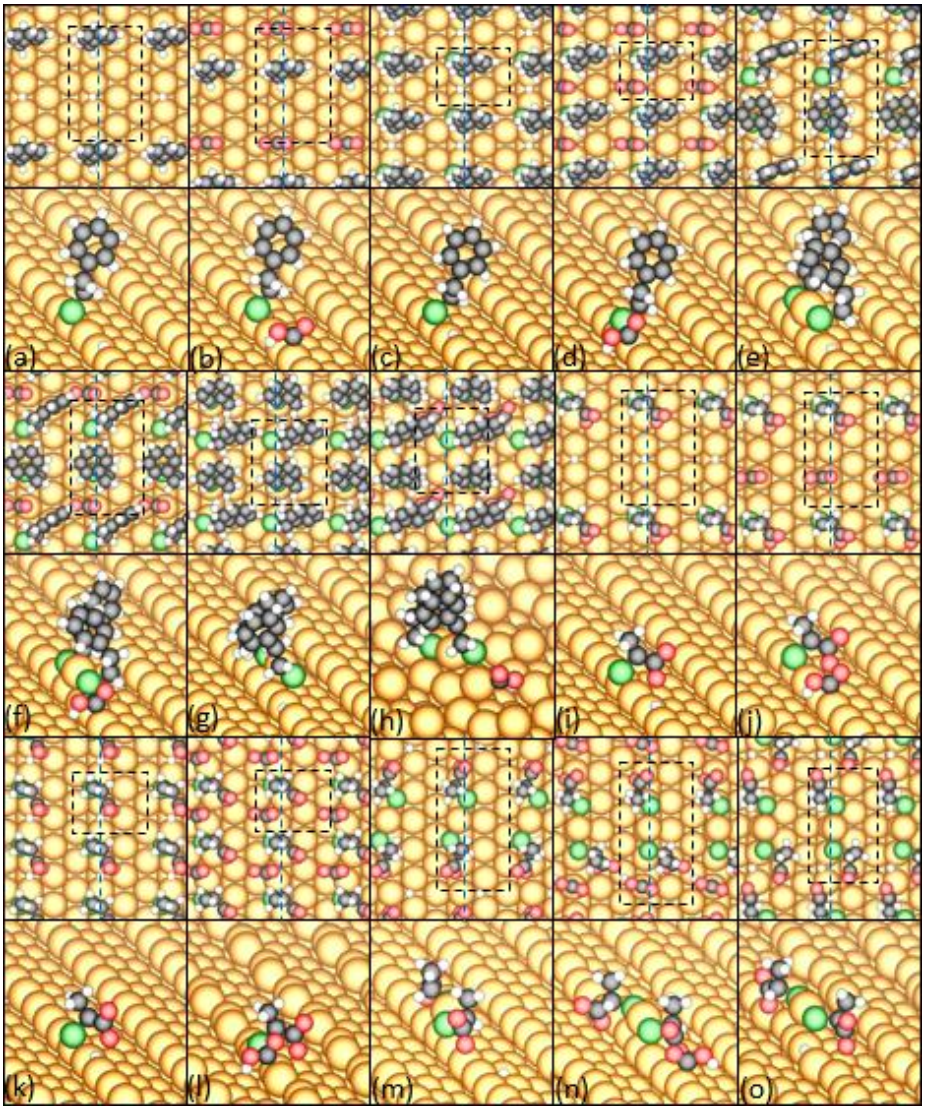

Figure 3.16. Top (top panels) and tilted side (bottom panels) views of DFT-calculated minimum free energy geometries of (a, b, c and d) intermediates on 2-PETt/Au(211); (e, f, g and h) intermediates on $(2\text{-PETt})_2Au$/Au(211); (i, j, k and l) intermediates on 2-MPAtt/Au(211); (m, n and o) intermediates on $(2\text{-MPAtt})_2Au$/Au(211). Yellow, green, black, red and white spheres represent Au, S, C, O and H atoms, respectively. Black and blue dashed lines indicate surface unit cells and step edges, respectively. For clarity, periodic images of adsorbates have been removed from the side views.

The catalytic activities of CO_2RR on various Au sites are in the order: defect sites on blank Au surfaces (ca. -0.3 V vs. RHE) > defect sites on 2-PETt modified Au surfaces (ca. -0.5 V vs. RHE) > terrace sites on blank Au surfaces (ca. -0.6 V vs. RHE) > defect sites on 2-MPAtt modified surfaces (ca. -0.9 V vs. RHE). The calculated limiting potential of CO_2RR on 2-PETt modified Au(211) is more positive than that on blank Au(111). The current density of CO on 2-PETt modified Au surfaces is larger than that on blank Au surfaces, and the current density of HER on 2-MPAtt modified Au surfaces is larger than that on blank Au surfaces. Thus, the adsorbed thiolate species had negligible poisoning effect on the catalytic activities of Au electrodes in electrochemical CO_2RR.

The differences between 2-PET-Au and 2-MPAtt-Au in electrochemical CO_2RR are: 1) 2-PET thiolate species generated negative dipole moments on Au surfaces, stabilizing the intermediate $^*COOH$ (the dipole moments of $^*COOH$ on Au surfaces are positive). However, 2-MPAtt species generated positive dipole moments on Au surfaces, destabilizing the intermediate $^*COOH$ (**Table 3.5**); 2) the -COO groups of 2-MPAtt species induced strong repulsion effects on the intermediate $^*COOH$ and *H, whereas 2-PETt species induced weak repulsion effects on the intermediates.

In literature, thiolate-modified Au nanoclusters did not promote the CO_2RR since the exterior Au atoms were fully occupied by thiolates.[157, 164, 165] The desorption of thiolates from Au surfaces would expose active Au atoms for the CO_2RR. In **Figure 3.12e**, the total current density on 2-MPA-Au rose rapidly in the potential range of -0.9 to -1.0V vs. RHE because the 2-MPAtt species desorbed from the surfaces at -0.9 vs. RHE.

In addition, the interfacial environment on the thiolate modified Au surfaces tuned the selectivity of CO_2RR and HER. The -COO group of 2-MPAtt transfers the protons from the

solutions to the vicinity of the electrode surfaces, whereas the phenyl group in 2-PET would push protons away from the surfaces since the phenyl group is hydrophobicity. The concentration of protons near the electrode has an effect on the selectivity of electrochemical CO_2RRs.[166-168]

Chapter 4. Summary

We investigated the orientations of ligands on Au surfaces. We found that $-C_6H_4-SH$ and $-S-C_6H_5$ adsorbed on Au(111) surfaces in upright and tilt configurations through Au-C and Au-S bonds, respectively. Adenine molecule has various orientations on Au(111) surfaces. In vacuum, the plane of adenine is parallel to the surfaces and adenine adsorbs on Au(111) with an adsorption energy of ca. -1.1 eV (calculated using optB86b functional), whereas the plane of adenine might be upright on the surfaces in solution and the adsorption energy of upright adenine on Au(111) surfaces was calculated to be ca. -1.3 eV (optB86b functional). 2-PET thiolate molecule is tilt on Au surfaces due to the sp^3 hybridization in the sulfur atom. Therefore, the orientation of adsorbed ligand on Au is controlled by the strength of the Au-ligand bond, the environmental conditions, and the electronic structure of the ligand.

We studied the adsorption sites of ligands on Au surfaces. We demonstrated that the ligand of $-C_6H_4-SH$ preferred to adsorb on the top site of a surface Au atom on Au(111), whereas the ligand of $-S-C_6H_5$ preferred to adsorb on somewhere between a bridge and a fcc site on Au(111). Adenine adsorbs on top sites of Au(111) surfaces through N-Au bonds. For 2-PETt on Au surfaces, the S head group is located on fcc hollow and bridge sites on Au(111) and Au(211), respectively. For $(2\text{-PETt})_2Au$ on Au surfaces, the S head groups are on the top sites of surface Au atoms. Thus, ligands are able to adsorb on three different sites, top, bridge, and 3-fold hollow, on Au surfaces through various head groups.

We also studied the stability of ligands on Au surfaces. The Au-C bond of $Au-C_6H_4-SH$ was found to be ca. 0.4 eV (optB88 functional) stronger than the Au-S bond of $Au-S-C_6H_5$, which explained the excellent stability of the Au-C bond at a wide range of potentials in experiments. The Au-N bond of upright adenine on Au(111) is stronger than that of parallel

adenine on Au(111). The $(2\text{-PETt})_2$Au complex was found to be stable on Au(111) surfaces at a potential range of 0 to -1.3 V vs. RHE.

In addition, we studied the adsorption states and desorption species of ligands on Au surfaces. The calculated vibrational frequency of the Au-C stretching was observed in the Raman spectra of Au-Ar-S^{-} monolayers on Au(111), indicating that prepared monolayers formed Au-C bond on Au(111). The N9H tautomer of adenine was found to be the most stable tautomer on Au(111) surfaces, and it adsorbed on Au(111) surfaces through N1, N3, or N7 atom, with N3 mode the most stable one. The dissociation of acidic N9 hydrogen of N3 mode was thermodynamically unfavorable. The calculated desorption temperatures of adenine on Au(111) surfaces were in agreement with the measured desorption temperatures in experiments. If the interconversion between tautomers is inhibited, the desorption temperature of N3H tautomer on Au(111) surfaces is higher than that of N9H tautomer on Au(111) surfaces. 2-PET molecules form 2-PETt, (2-PETt)Au and $(2\text{-PETt})_2$Au complexes on Au surfaces. The thermal desorption to produce phenylethyl disulfide is thermodynamically unfavorable with a reaction energy of 0.51 eV (optB86b functional). The pKa of 2-PET was calculated to be 10.65 which was consistent with the pKa value in literature. 2-PET thiolate species on Au surfaces desorb as 2-PET molecules and 2-PET anions at pH < pKa and pH > pKa, respectively. The stability order of 2-PET thiolate states on Au surfaces is: $(2\text{-PETt})_2$Au/Au(111) > $(2\text{-PETt})_2$Au/Au(211) > (2-PETt)Au/Au(211) > 2-PETt/Au(211) = (2-PETt)Au/Au(111) > 2-PETt/Au(111). The calculated desorption potentials of 2-PET thiolate states shifted negatively as the pH of solutions increased at pH < pKa, whereas the calculated desorption potentials of 2-PET thiolate species on Au surfaces were not dependent on pH at pH > pKa.

Finally, we investigated the catalytic activities of ligands modified Au electrodes in electrochemical CO_2RR using DFT methods. The limiting potential of CO evolution on (2-PETt)$_2$Au/Au(211) was found to be 0.14 eV (RPBE functional) more positive than that on blank Au(111), whereas the limiting potential of CO evolution on (2-MPAtt)$_2$Au was found to be 0.26 eV (RPBE functional) more negative than that on blank Au(111). Our calculated results were in agreement with the experimental evidences that 2-PET and 2-MPA promoted the CO evolution and HER respectively on Au electrodes. (2-PETt)$_2$Au complexes were predicted to be prevalent on Au(211) surfaces, and was the only thiolate state that promoted CO_2RR at high edge coverage (θ=3/4). We demonstrated that 2-PETt molecules induced negative dipole moments on Au electrodes, which stabilized the intermediate *COOH species (the dipole moment of *COOH was positive). The -COO groups of 2-MPAtt molecules generated repulsive forces on Au electrodes, pushing the intermediate *COOH away from the surfaces. The hydrophobicity of the phenyl groups of 2-PETt molecules and the hydrophilism of the -COO groups of 2-MPAtt molecules changed the proton concentrations in the vicinity of the electrode surfaces. The modification of Au electrodes with certain ligands is an effective and simple way to promote the catalytic activity and selectivity of electrochemical CO_2RR.

To provide guidelines for rational selection of ligands to modify metallic catalysts, many systematic studies on the interaction of ligands with metals should be carried out in the future. Literatures have shown that several ligands, such as chemisorbed oxygen[169], graphene[170], and atomic nitrogen[171] induced the surface reconstructions of Cu surfaces. Ag and Pd surfaces were reconstructed by chemisorbed oxygen[172] and CO[173], respectively. The kinetics of different ligands reconstructing different metals could be investigated using climbing image nudged elastic band (CI-NEB) method.[174, 175] The nudged elastic band method is used to find minimum

energy paths and saddle points between known reactants and products, and the climbing image method is used to find an accurate saddle point with a few images. Ligand is promising to create more active sites on metal catalysts if it is able to reconstruct metal surfaces.

Another systematic study is different functional groups' effects on the selectivity of electrochemical CO_2RR. Fang and co-workers have reported that the formation of $HCOO^-$ and CO on Au electrodes using ligands which possessing pyridine and NH_2 functional groups respectively in the same electrochemical conditions.[176] The mechanisms of those reactions could be investigated using theoretical methods.

Appendix. Copyright Information

American Chemical Society:

For figure on page 6
Logged in as: XUN CHENG
Account #: 3001531572
Title: Electrocatalytic Conversion of Carbon Dioxide to Methane and Methanol on Transition Metal Surfaces
Author: Kendra P. Kuhl, Toru Hatsukade, Etosha R. Cave, et al
Publication: Journal of the American Chemical Society
Publisher: American Chemical Society Date: Oct 1, 2014

PERMISSION/LICENSE IS GRANTED FOR YOUR ORDER AT NO CHARGE

This type of permission/license, instead of the standard Terms & Conditions, is sent to you because no fee is being charged for your order. Please note the following:

- Permission is granted for your request in both print and electronic formats, and translations.
- If figures and/or tables were requested, they may be adapted or used in part.
- Please print this page for your records and send a copy of it to your publisher/graduate school.
- Appropriate credit for the requested material should be given as follows: "Reprinted (adapted) with permission from (COMPLETE REFERENCE CITATION). Copyright (YEAR) American Chemical Society." Insert appropriate information in place of the capitalized words.
- One-time permission is granted only for the use specified in your request. No additional uses are granted (such as derivative works or other editions). For any other uses, please submit a new request.

For figure on page 7
Logged in as: XUN CHENG
Account #: 3001531572
Title: Experimental and Computational Investigation of Au25 Clusters and CO2: A Unique Interaction and Enhanced Electrocatalytic Activity
Author: Douglas R. Kauffman, Dominic Alfonso, Christopher Matranga, et al
Publication: Journal of the American Chemical Society
Publisher: American Chemical Society Date: Jun 1, 2012

PERMISSION/LICENSE IS GRANTED FOR YOUR ORDER AT NO CHARGE

This type of permission/license, instead of the standard Terms & Conditions, is sent to you because no fee is being charged for your order. Please note the following:

- Permission is granted for your request in both print and electronic formats, and translations.
- If figures and/or tables were requested, they may be adapted or used in part.
- Please print this page for your records and send a copy of it to your publisher/graduate school.
- Appropriate credit for the requested material should be given as follows: "Reprinted (adapted) with permission from (COMPLETE REFERENCE CITATION). Copyright (YEAR) American Chemical Society." Insert appropriate information in place of the capitalized words.
- One-time permission is granted only for the use specified in your request. No additional uses are granted (such as derivative works or other editions). For any other uses, please submit a new request.

For figure on page 8
Logged in as: XUN CHENG
Account #: 3001531572
Title: Monodisperse Au Nanoparticles for Selective Electrocatalytic Reduction of CO2 to CO
Author: Wenlei Zhu, Ronald Michalsky, Önder Metin, et al
Publication: Journal of the American Chemical Society
Publisher: American Chemical Society
Date: Nov 1, 2013

PERMISSION/LICENSE IS GRANTED FOR YOUR ORDER AT NO CHARGE

This type of permission/license, instead of the standard Terms & Conditions, is sent to you because no fee is being charged for your order. Please note the following:

- Permission is granted for your request in both print and electronic formats, and translations.
- If figures and/or tables were requested, they may be adapted or used in part.
- Please print this page for your records and send a copy of it to your publisher/graduate school.
- Appropriate credit for the requested material should be given as follows: "Reprinted (adapted) with permission from (COMPLETE REFERENCE CITATION). Copyright (YEAR) American Chemical Society." Insert appropriate information in place of the capitalized words.
- One-time permission is granted only for the use specified in your request. No additional uses are granted (such as derivative works or other editions). For any other uses, please submit a new request.

For figure on page 9
Logged in as: XUN CHENG
Account #: 3001531572
Title: Active and Selective Conversion of CO2 to CO on Ultrathin Au Nanowires
Author: Wenlei Zhu, Yin-Jia Zhang, Hongyi Zhang, et al
Publication: Journal of the American Chemical Society
Publisher: American Chemical Society
Date: Nov 1, 2014

PERMISSION/LICENSE IS GRANTED FOR YOUR ORDER AT NO CHARGE

This type of permission/license, instead of the standard Terms & Conditions, is sent to you because no fee is being charged for your order. Please note the following:

- Permission is granted for your request in both print and electronic formats, and translations.
- If figures and/or tables were requested, they may be adapted or used in part.
- Please print this page for your records and send a copy of it to your publisher/graduate school.
- Appropriate credit for the requested material should be given as follows: "Reprinted (adapted) with permission from (COMPLETE REFERENCE CITATION). Copyright (YEAR) American Chemical Society." Insert appropriate information in place of the capitalized words.
- One-time permission is granted only for the use specified in your request. No additional uses are granted (such as derivative works or other editions). For any other uses, please submit a new request.

For figure on page 14
Logged in as: XUN CHENG
Account #: 3001531572
Title: Theoretical Insights into Electrochemical CO2 Reduction Mechanisms Catalyzed by Surface-Bound Nitrogen Heterocycles
Author: John A. Keith, Emily A. Carter
Publication: Journal of Physical Chemistry Letters
Publisher: American Chemical Society
Date: Dec 1, 2013

PERMISSION/LICENSE IS GRANTED FOR YOUR ORDER AT NO CHARGE

This type of permission/license, instead of the standard Terms & Conditions, is sent to you because no fee is being charged for your order. Please note the following:

- Permission is granted for your request in both print and electronic formats, and translations.
- If figures and/or tables were requested, they may be adapted or used in part.
- Please print this page for your records and send a copy of it to your publisher/graduate school.
- Appropriate credit for the requested material should be given as follows: "Reprinted (adapted) with permission from (COMPLETE REFERENCE CITATION). Copyright (YEAR) American Chemical Society." Insert appropriate information in place of the capitalized words.
- One-time permission is granted only for the use specified in your request. No additional uses are granted (such as derivative works or other editions). For any other uses, please submit a new request.

For figure on page 15 and 16
Logged in as: XUN CHENG
Account #: 3001531572
Title: Understanding Trends in the Electrocatalytic Activity of Metals and Enzymes for CO2 Reduction to CO
Author: Heine A. Hansen, Joel B. Varley, Andrew A. Peterson, et al
Publication: Journal of Physical Chemistry Letters
Publisher: American Chemical Society
Date: Feb 1, 2013

PERMISSION/LICENSE IS GRANTED FOR YOUR ORDER AT NO CHARGE

This type of permission/license, instead of the standard Terms & Conditions, is sent to you because no fee is being charged for your order. Please note the following:

- Permission is granted for your request in both print and electronic formats, and translations.
- If figures and/or tables were requested, they may be adapted or used in part.
- Please print this page for your records and send a copy of it to your publisher/graduate school.
- Appropriate credit for the requested material should be given as follows: "Reprinted (adapted) with permission from (COMPLETE REFERENCE CITATION). Copyright (YEAR) American Chemical Society." Insert appropriate information in place of the capitalized words.
- One-time permission is granted only for the use specified in your request. No additional uses are granted (such as derivative works or other editions). For any other uses, please submit a new request.

For figure on page 19
Logged in as: XUN CHENG
Account #: 3001531572
Title: Effects of ω-Functional Groups on pH-Dependent Reductive Desorption of Alkanethiol SelfAssembled Monolayers
Author: Hirokazu Munakata, Daisuke Oyamatsu, Susumu Kuwabata
Publication: Langmuir
Publisher: American Chemical Society
Date: Nov 1, 2004

PERMISSION/LICENSE IS GRANTED FOR YOUR ORDER AT NO CHARGE

This type of permission/license, instead of the standard Terms & Conditions, is sent to you because no fee is being charged for your order. Please note the following:

- Permission is granted for your request in both print and electronic formats, and translations.
- If figures and/or tables were requested, they may be adapted or used in part.
- Please print this page for your records and send a copy of it to your publisher/graduate school.
- Appropriate credit for the requested material should be given as follows: "Reprinted (adapted) with permission from (COMPLETE REFERENCE CITATION). Copyright (YEAR) American Chemical Society." Insert appropriate information in place of the capitalized words.
- One-time permission is granted only for the use specified in your request. No additional uses are granted (such as derivative works or other editions). For any other uses, please submit a new request.

For figure on page 20
Logged in as: XUN CHENG
Account #: 3001531572
Title: Structure Evolution of Aromatic-Derivatized Thiol Monolayers on Evaporated Gold
Author: Yu-Tai Tao, Chien-Ching Wu, Ji-Yang Eu, et al
Publication: Langmuir
Publisher: American Chemical Society
Date: Jul 1, 1997

PERMISSION/LICENSE IS GRANTED FOR YOUR ORDER AT NO CHARGE

This type of permission/license, instead of the standard Terms & Conditions, is sent to you because no fee is being charged for your order. Please note the following:

- Permission is granted for your request in both print and electronic formats, and translations.
- If figures and/or tables were requested, they may be adapted or used in part.
- Please print this page for your records and send a copy of it to your publisher/graduate school.
- Appropriate credit for the requested material should be given as follows: "Reprinted (adapted) with permission from (COMPLETE REFERENCE CITATION). Copyright (YEAR) American Chemical Society." Insert appropriate information in place of the capitalized words.
- One-time permission is granted only for the use specified in your request. No additional uses are granted (such as derivative works or other editions). For any other uses, please submit a new request.

For content in Chapter 3.1
Logged in as: XUN CHENG
Account #: 3001531572
Title: Spectroscopic Identification of the Au–C Bond Formation upon Electroreduction of an Aryl Diazonium Salt on Gold
Author: Limin Guo, Lipo Ma, Yelong Zhang, et al
Publication: Langmuir
Publisher: American Chemical Society
Date: Nov 1, 2016

PERMISSION/LICENSE IS GRANTED FOR YOUR ORDER AT NO CHARGE

This type of permission/license, instead of the standard Terms & Conditions, is sent to you because no fee is being charged for your order. Please note the following:

- Permission is granted for your request in both print and electronic formats, and translations.
- If figures and/or tables were requested, they may be adapted or used in part.
- Please print this page for your records and send a copy of it to your publisher/graduate school.
- Appropriate credit for the requested material should be given as follows: "Reprinted (adapted) with permission from (COMPLETE REFERENCE CITATION). Copyright (YEAR) American Chemical Society." Insert appropriate information in place of the capitalized words.
- One-time permission is granted only for the use specified in your request. No additional uses are granted (such as derivative works or other editions). For any other uses, please submit a new request.

The Royal Society of Chemistry:

For figure on page 18 and 24, and content in Chapter 3.3
Title: CO2 electrochemical reduction at thiolate-modified bulk Au electrode

Author: Y. Fang, X. Cheng, J. C. Flake and Y. Xu, *Catal. Sci. Technol.*, 2019, 9, 2689
DOI: 10.1039/C9CY00506D

If you are the author of this article you do not need to formally request permission to reproduce figures, diagrams etc. contained in this article in third party publications or in a thesis or dissertation provided that the correct acknowledgement is given with the reproduced material.

Reproduced material should be attributed as follows:

- For reproduction of material from NJC:

  [Original citation] - Reproduced by permission of The Royal Society of Chemistry (RSC) on behalf of the Centre National de la Recherche Scientifique (CNRS) and the RSC
- For reproduction of material from PCCP:

  [Original citation] - Reproduced by permission of the PCCP Owner Societies
- For reproduction of material from PPS:

  [Original citation] - Reproduced by permission of The Royal Society of Chemistry (RSC) on behalf of the European Society for Photobiology, the European Photochemistry Association, and RSC
- For reproduction of material from all other RSC journals:

  [Original citation] - Reproduced by permission of The Royal Society of Chemistry

If you are the author of this article you still need to obtain permission to reproduce the whole article in a third party publication with the exception of reproduction of the whole article in a thesis or dissertation.

For content in Chapter 3.2
Title: An experimental and theoretical study of adenine adsorption on Au(111)

Author: R. G. Acres, X. Cheng, K. Beranová, S. Bercha, T. Skála, V. Matolín, Y. Xu, K. C. Prince and N. Tsud, *Phys. Chem. Chem. Phys.*, 2018, **20**, 4688
DOI: 10.1039/C7CP08102B

Elsevier:

For figure on page 17

License Number 4684511103993

License date Oct 08, 2019

Licensed Content Publisher Elsevier

Licensed Content Publication Electrochimica Acta

Licensed Content Title Adsorption of mercaptopropionic acid onto Au(1 1 1) Part I. Adlayer formation, structure and electrochemistry

Licensed Content Author Marc Petri,Dieter M. Kolb,Ulrich Memmert,Heinrich Meyer

Licensed Content Date Dec 30, 2003

Licensed Content Volume 49

Licensed Content Issue 1

Licensed Content Pages 8

Type of Use reuse in a thesis/dissertation

Portion figures/tables/illustrations

Number of figures/tables/illustrations 1

Format both print and electronic

Are you the author of this Elsevier article? No

Will you be translating? No

Original figure numbers figure 3

Title of your thesis/dissertation FIRST-PRINCIPLE STUDY ON INTERACTION OF LIGANDS WITH GOLD AND EFFECTS ON CATALYTIC ACTIVITIES

Expected completion date May 2020

Estimated size (number of pages) 80

For figure on page 2 and 3

License Number 4684010661588

License date Oct 08, 2019

Licensed Content Publisher Elsevier

Licensed Content Publication Nano Energy

Licensed Content Title Electrochemical CO2 reduction: Electrocatalyst, reaction mechanism, and process engineering

Licensed Content Author Qi Lu,Feng Jiao

Licensed Content Date Nov 1, 2016

Licensed Content Volume 29

Licensed Content Issue n/a

Licensed Content Pages 18

Type of Use reuse in a thesis/dissertation Portion figures/tables/illustrations

Number of figures/tables/illustrations 2

Format both print and electronic

Are you the author of this Elsevier article? No

Will you be translating? No

Original figure numbers Fig 2 and Table 1

Title of your thesis/dissertation FIRST-PRINCIPLE STUDY ON INTERACTION OF LIGANDS WITH GOLD AND EFFECTS ON CATALYTIC ACTIVITIES

Expected completion date May 2020

Estimated size (number of pages) 80

John Wiley and Sons:

For figure on page 4, 5 and 13

License Number 4684301057455

License date Oct 08, 2019

Licensed Content Publisher John Wiley and Sons

Licensed Content Publication Israel Journal of Chemistry

Licensed Content Title Electrochemical CO2 Reduction: Recent Advances and Current Trends

Licensed Content Author George A. Olah, G. K. Surya Prakash, John-Paul Jones

Licensed Content Date Sep 9, 2014

Licensed Content Volume 54

Licensed Content Issue 10

Licensed Content Pages 16

Type of use Dissertation/Thesis

Requestor type University/Academic

Format Print and electronic

Portion Figure/table

Number of figures/tables 4

Original Wiley figure/table number(s) scheme 1, table 1, table 2 and table 6

Will you be translating? No

Title of your thesis / dissertation FIRST-PRINCIPLE STUDY ON INTERACTION OF LIGANDS WITH GOLD AND EFFECTS ON CATALYTIC ACTIVITIES

Expected completion date May 2020

Expected size (number of pages) 80

The Electrochemical Society:

For figure on page 11 and 12

Title: Electrocatalytic Reduction of CO2 at Au Nanoparticle Electrodes: Effects of Interfacial Chemistry on Reduction Behavior

Author: Evan Andrews, Sai Katla, Challa Kumar, et al

Publication: Journal of The Electrochemical Society

Permission Status: Granted

Permission type: Republish or display content

Type of use: Republish in a thesis/dissertation

Requestor type Not-for-profit entity

Format Print, Electronic

Portion image/photo

Number of images/photos requested 2

The requesting person/organization XUN CHENG

Title of the article or chapter the portion is from Electrocatalytic Reduction of CO2 at Au Nanoparticle Electrodes: Effects of Interfacial Chemistry on Reduction Behavior

Editor of portion(s) N/A

Author of portion(s) XUN CHENG

Volume of serial or monograph N/A

Page range of portion 17-18

Publication date of portion MAY 2020

Rights for Main product

Duration of use Life of current edition

Creation of copies for the disabled no

With minor editing privileges no

For distribution to United States

In the following language(s) Original language of publication

With incidental promotional use no

Lifetime unit quantity of new product Up to 499

Title FIRST-PRINCIPLE STUDY ON INTERACTION OF LIGANDS WITH GOLD AND EFFECTS ON CATALYTIC ACTIVITIES

Expected presentation date May 2020

References

1. *Earth System Research Laboratory. NOAA.*

2. D. M. Etheridge, L. P. Steele, R. L. Langenfelds, R. J. Francey, J. M. Barnola and V. I. Morgan, *J. Geophys. Res. Atmos.*, 1996, **101**, 4115-4128.

3. B. Hu, C. Guild and S. L. Suib, *J. CO2 Util.*, 2013, **1**, 18-27.

4. D. Lüthi, M. Le Floch, B. Bereiter, T. Blunier, J.-M. Barnola, U. Siegenthaler, D. Raynaud, J. Jouzel, H. Fischer, K. Kawamura and T. F. Stocker, *Nature*, 2008, **453**, 379-382.

5. A. Goeppert, M. Czaun, R. B. May, G. K. S. Prakash, G. A. Olah and S. R. Narayanan, *J. Am. Chem. Soc.*, 2011, **133**, 20164-20167.

6. J.-P. Jones, G. K. S. Prakash and G. A. Olah, *Isr. J. Chem.*, 2014, **54**, 1451-1466.

7. S. Back, H. Kim and Y. Jung, *ACS Catal.*, 2015, **5**, 965-971.

8. Q. Lu and F. Jiao, *Nano Energy*, 2016, **29**, 439-456.

9. S. Ringe, E. L. Clark, J. Resasco, A. Walton, B. Seger, A. T. Bell and K. Chan, *Energ. Environ. Sci.*, 2019, **12**, 3001-3014.

10. S. Lee and J. Lee, *ChemSusChem*, 2016, **9**, 333-344.

11. Y. Hori, K. Kikuchi and S. Suzuki, *Chem. Lett.*, 1985, **14**, 1695-1698.

12. K. P. Kuhl, T. Hatsukade, E. R. Cave, D. N. Abram, J. Kibsgaard and T. F. Jaramillo, *J. Am. Chem. Soc.*, 2014, **136**, 14107-14113.

13. A. A. Peterson and J. K. Nørskov, *J. Phys. Chem. Lett.*, 2012, **3**, 251-258.

14. Y. Hori, in *Mod. Aspect. Electroc.*, eds. C. G. Vayenas, R. E. White and M. E. Gamboa-Aldeco, Springer New York, New York, NY, 2008, DOI: 10.1007/978-0-387-49489-0_3, pp. 89-189.

15. Y. Hori, A. Murata, K. Kikuchi and S. Suzuki, *J. Chem. Soc., Chem. Commun.*, 1987, 728-729.

16. H. Noda, S. Ikeda, A. Yamamoto, H. Einaga and K. Ito, *Bull. Chem. Soc. Jpn.*, 1995, **68**, 1889-1895.

17. D. R. Kauffman, D. Alfonso, C. Matranga, H. Qian and R. Jin, *J. Am. Chem. Soc.*, 2012, **134**, 10237-10243.

18. W. Zhu, R. Michalsky, Ö. Metin, H. Lv, S. Guo, C. J. Wright, X. Sun, A. A. Peterson and S. Sun, *J. Am. Chem. Soc.*, 2013, **135**, 16833-16836.

19. W. Zhu, Y.-J. Zhang, H. Zhang, H. Lv, Q. Li, R. Michalsky, A. A. Peterson and S. Sun, *J. Am. Chem. Soc.*, 2014, **136**, 16132-16135.

20. H. Mistry, R. Reske, Z. Zeng, Z.-J. Zhao, J. Greeley, P. Strasser and B. R. Cuenya, *J. Am. Chem. Soc.*, 2014, **136**, 16473-16476.

21. I. Gosens, J. A. Post, L. J. J. de la Fonteyne, E. H. J. M. Jansen, J. W. Geus, F. R. Cassee and W. H. de Jong, *Part. Fibre Toxicol.*, 2010, **7**, 37.

22. M. Watanabe, M. Shibata, A. Kato, M. Azuma and T. Sakata, *J. Electrochem. Soc.*, 1991, **138**, 3382-3389.

23. S. Rasul, D. H. Anjum, A. Jedidi, Y. Minenkov, L. Cavallo and K. Takanabe, *Angew. Chem. Int. Ed.*, 2015, **54**, 2146-2150.

24. C. Hahn, D. N. Abram, H. A. Hansen, T. Hatsukade, A. Jackson, N. C. Johnson, T. R. Hellstern, K. P. Kuhl, E. R. Cave, J. T. Feaster and T. F. Jaramillo, *J. Mater. Chem. A*, 2015, **3**, 20185-20194.

25. J. Christophe, T. Doneux and C. Buess-Herman, *Electrocatalysis*, 2012, **3**, 139-146.

26. F. Jia, X. Yu and L. Zhang, *J. Power Sources*, 2014, **252**, 85-89.

27. H. Wang, D. Liu and C. Xu, *Catal. Sci. Technol.*, 2016, **6**, 7137-7150.

28. E. Andrews, S. Katla, C. Kumar, M. Patterson, P. Sprunger and J. Flake, *J. Electrochem. Soc.*, 2015, **162**, F1373-F1378.

29. R. L. Garrell, J. E. Chadwick, D. L. Severance, N. A. McDonald and D. C. Myles, *J. Am. Chem. Soc.*, 1995, **117**, 11563-11571.

30. G. Seshadri, C. Lin and A. B. Bocarsly, *J. Electroanal. Chem.*, 1994, **372**, 145-150.

31. E. Barton Cole, P. S. Lakkaraju, D. M. Rampulla, A. J. Morris, E. Abelev and A. B. Bocarsly, *J. Am. Chem. Soc.*, 2010, **132**, 11539-11551.

32. E. E. Barton Cole, M. F. Baruch, R. P. L'Esperance, M. T. Kelly, P. S. Lakkaraju, E. L. Zeitler and A. B. Bocarsly, *Top. Catal.*, 2015, **58**, 15-22.

33. J. A. Keith and E. A. Carter, *J. Phys. Chem. Lett.*, 2013, **4**, 4058-4063.

34. M. Lessio and E. A. Carter, *J. Am. Chem. Soc.*, 2015, **137**, 13248-13251.

35. J. A. Keith and E. A. Carter, *J. Am. Chem. Soc.*, 2012, **134**, 7580-7583.

36. J. Hawecker, J.-M. Lehn and R. Ziessel, *J. Chem. Soc., Chem. Commun.*, 1984, 328-330.

37. D. Xiang, D. Magana and R. B. Dyer, *J. Am. Chem. Soc.*, 2014, **136**, 14007-14010.

38. J. Heo, C. R. Staples and P. W. Ludden, *Biochemistry*, 2001, **40**, 7604-7611.

39. J.-H. Jeoung and H. Dobbek, *Science*, 2007, **318**, 1461.

40. H. Dobbek, L. Gremer, O. Meyer and R. Huber, *Proc. Natl. Acad. Sci.*, 1999, **96**, 8884.

41. W. Gong, B. Hao, Z. Wei, D. J. Ferguson, T. Tallant, J. A. Krzycki and M. K. Chan, *Proc. Natl. Acad. Sci.*, 2008, **105**, 9558-9563.

42. H. A. Hansen, J. B. Varley, A. A. Peterson and J. K. Nørskov, *J. Phys. Chem. Lett.*, 2013, **4**, 388-392.

43. A. Ulman, *Chem. Rev.*, 1996, **96**, 1533-1554.

44. R. K. Smith, P. A. Lewis and P. S. Weiss, *Prog. Surf. Sci.*, 2004, **75**, 1-68.

45. J. C. Love, L. A. Estroff, J. K. Kriebel, R. G. Nuzzo and G. M. Whitesides, *Chem. Rev.*, 2005, **105**, 1103-1170.

46. P. Maksymovych, O. Voznyy, D. B. Dougherty, D. C. Sorescu and J. T. Yates, *Prog. Surf. Sci.*, 2010, **85**, 206-240.

47. G. Yang and G.-y. Liu, *J. Phys. Chem. B*, 2003, **107**, 8746-8759.

48. S. T. Marshall, M. O'Brien, B. Oetter, A. Corpuz, R. M. Richards, D. K. Schwartz and J. W. Medlin, *Nat. Mater.*, 2010, **9**, 853.

49. P. G. Lustemberg, M. L. Martiarena, A. E. Martínez and H. F. Busnengo, *Langmuir*, 2008, **24**, 3274-3279.

50. F. Tielens and E. Santos, *J. Phys. Chem. C*, 2010, **114**, 9444-9452.

51. Y. W. Yang and L. J. Fan, *Langmuir*, 2002, **18**, 1157-1164.

52. M.-C. Bourg, A. Badia and R. B. Lennox, *J. Phys. Chem. B*, 2000, **104**, 6562-6567.

53. J. V. Barth, H. Brune, G. Ertl and R. J. Behm, *Phys. Rev. B*, 1990, **42**, 9307-9318.

54. B. K. Min, A. R. Alemozafar, M. M. Biener, J. Biener and C. M. Friend, *Top. Catal.*, 2005, **36**, 77-90.

55. G. Dodero, L. De Michieli, O. Cavalleri, R. Rolandi, L. Oliveri, A. Daccà and R. Parodi, *Colloids Surf. A*, 2000, **175**, 121-128.

56. G. E. Poirier, *Chem. Rev.*, 1997, **97**, 1117-1128.

57. N. A. Kautz and S. A. Kandel, *J. Am. Chem. Soc.*, 2008, **130**, 6908-6909.

58. M. Petri, D. M. Kolb, U. Memmert and H. Meyer, *Electrochim. Acta*, 2003, **49**, 175-182.

59. D. C. Sheppard, G. S. Parkinson, A. Hentz, A. J. Window, P. D. Quinn, D. P. Woodruff, P. Bailey and T. C. Q. Noakes, *Surf. Sci.*, 2011, **605**, 138-145.

60. L. M. Molina and B. Hammer, *Chem. Phys. Lett.*, 2002, **360**, 264-271.

61. C. Vericat, M. E. Vela, G. Benitez, P. Carro and R. C. Salvarezza, *Chem. Soc. Rev.*, 2010, **39**, 1805-1834.

62. O. Azzaroni, M. E. Vela, H. Martin, A. Hernández Creus, G. Andreasen and R. C. Salvarezza, *Langmuir*, 2001, **17**, 6647-6654.

63. H. Munakata, D. Oyamatsu and S. Kuwabata, *Langmuir*, 2004, **20**, 10123-10128.

64. D. Hobara, K. Miyake, S.-i. Imabayashi, K. Niki and T. Kakiuchi, *Langmuir*, 1998, **14**, 3590-3596.

65. D. F. Yang, C. P. Wilde and M. Morin, *Langmuir*, 1996, **12**, 6570-6577.

66. Y.-T. Tao, C.-C. Wu, J.-Y. Eu, W.-L. Lin, K.-C. Wu and C.-h. Chen, *Langmuir*, 1997, **13**, 4018-4023.

67. H. Kang and J. Noh, *Bull. Korean Chem. Soc.*, 2013, **34**, 1383-1387.

68. S.-i. Imabayashi, M. Iida, D. Hobara, Z. Q. Feng, K. Niki and T. Kakiuchi, *J. Electroanal. Chem.*, 1997, **428**, 33-38.

69. E. W. van der Vegte and G. Hadziioannou, *J. Phys. Chem. B*, 1997, **101**, 9563-9569.

70. D. V. Vezenov, A. Noy, L. F. Rozsnyai and C. M. Lieber, *J. Am. Chem. Soc.*, 1997, **119**, 2006-2015.

71. M. L. Wallwork, D. A. Smith, J. Zhang, J. Kirkham and C. Robinson, *Langmuir*, 2001, **17**, 1126-1131.

72. W. A. Marmisollé, D. A. Capdevila, E. de la Llave, F. J. Williams and D. H. Murgida, *Langmuir*, 2013, **29**, 5351-5359.

73. Q. Liu, X. Yang, Y. Huang, S. Xu, X. Su, X. Pan, J. Xu, A. Wang, C. Liang, X. Wang and T. Zhang, *Energy Environ. Sci.*, 2015, **8**, 3204-3207.

74. P. Rodriguez, Y. Kwon and M. T. M. Koper, *Nat. Chem.*, 2012, **4**, 177-182.

75. X.-y. Rao, J.-j. Zhang, J. Cui, Y. Hu, T. Liu, J.-f. Chai, G.-f. Cheng, P.-g. He and Y.-z. Fang, *Chem. Res. Chinese U.*, 2013, **29**, 868-873.

76. J.-D. Qiu, H.-Z. Peng, R.-P. Liang, J. Li and X.-H. Xia, *Langmuir*, 2007, **23**, 2133-2137.

77. A. Baiker, *J. Mol. Catal. A Chem.*, 1997, **115**, 473-493.

78. K.-R. Hwang, C.-B. Lee and J.-S. Park, *J. Power Sources*, 2011, **196**, 1349-1352.

79. P. Zhang, C. Wang, Z. Chen and H. Li, *Catal. Sci. Technol.*, 2011, **1**, 1133-1137.

80. F.-M. McKenna, R. P. K. Wells and J. A. Anderson, *Chem. Comm.*, 2011, **47**, 2351-2353.

81. W. Gong, C. Chen, Y. Zhang, H. Zhou, H. Wang, H. Zhang, Y. Zhang, G. Wang and H. Zhao, *ACS Sustain. Chem. Eng.*, 2017, **5**, 2172-2180.

82. C. Montassier, J. C. Ménézo, L. C. Hoang, C. Renaud and J. Barbier, *J. Mol. Catal.* , 1991, **70**, 99-110.

83. Y. Fang, X. Cheng, J. C. Flake and Y. Xu, *Catal. Sci. Technol.*, 2019, **9**, 2689-2701.

84. G. Kresse and J. Furthmüller, *Phys. Rev. B*, 1996, **54**, 11169-11186.

85. G. Kresse and D. Joubert, *Phys. Rev. B*, 1999, **59**, 1758-1775.

86. M. Dion, H. Rydberg, E. Schröder, D. C. Langreth and B. I. Lundqvist, *Phys. Rev. Lett.*, 2004, **92**, 246401.

87. J. Klimeš, D. R. Bowler and A. Michaelides, *J. Phys. Condens. Matter*, 2010, **22**, 074203.

88. J. Klimeš, D. R. Bowler and A. Michaelides, *Phys. Rev. B*, 2011, **83**, 195131.

89. B. Hammer, L. B. Hansen and J. K. Nørskov, *Phys. Rev. B*, 1999, **59**, 7413-7421.

90. J. Wellendorff, T. L. Silbaugh, D. Garcia-Pintos, J. K. Nørskov, T. Bligaard, F. Studt and C. T. Campbell, *Surf. Sci.*, 2015, **640**, 36-44.

91. A. J. R. Hensley, K. Ghale, C. Rieg, T. Dang, E. Anderst, F. Studt, C. T. Campbell, J.-S. McEwen and Y. Xu, *J. Phys. Chem. C*, 2017, **121**, 4937-4945.

92. P. E. Blöchl, *Phys. Rev. B*, 1994, **50**, 17953-17979.

93. W. Kohn and L. J. Sham, *Phys. Rev.* , 1965, **140**, A1133-A1138.

94. M. Methfessel and A. T. Paxton, *Phys. Rev. B*, 1989, **40**, 3616-3621.

95. Y. Zhang, X. Zhang, J. Wang, W. C. McKee, Y. Xu and Z. Peng, *J. Phys. Chem. C*, 2016, **120**, 3690-3698.

96. N. W. Ashcroft and N. D. Mermin, *Solid state physics*, Saunders college, Philadelphia, Pa., 1976.

97. J. Neugebauer and M. Scheffler, *Phys. Rev. B*, 1992, **46**, 16067-16080.

98. D. A. McQuarrie and J. D. Simon, *Molecular thermodynamics*, University Science Books, Sausalito (California), 1999.

99. I. S. P. Savizi and M. J. Janik, *Electrochim. Acta*, 2011, **56**, 3996-4006.

100. K. Mathew, R. Sundararaman, K. Letchworth-Weaver, T. A. Arias and R. G. Hennig, *J. Chem. Phys.*, 2014, **140**, 084106.

101. B. Thapa and H. B. Schlegel, *J. Phys. Chem. A*, 2016, **120**, 5726-5735.

102. C. P. Kelly, C. J. Cramer and D. G. Truhlar, *J. Phys. Chem. B*, 2006, **110**, 16066-16081.

103. R. Mazzarello, A. Cossaro, A. Verdini, R. Rousseau, L. Casalis, M. F. Danisman, L. Floreano, S. Scandolo, A. Morgante and G. Scoles, *Phys. Rev. Lett.*, 2007, **98**, 016102.

104. G. Hu, R. Jin and D.-e. Jiang, *Nanoscale*, 2016, **8**, 20103-20110.

105. J. K. Nørskov, J. Rossmeisl, A. Logadottir, L. Lindqvist, J. R. Kitchin, T. Bligaard and H. Jónsson, *J. Phys. Chem. B*, 2004, **108**, 17886-17892.

106. J. Rosen, G. S. Hutchings, Q. Lu, S. Rivera, Y. Zhou, D. G. Vlachos and F. Jiao, *ACS Catal.*, 2015, **5**, 4293-4299.

107. M. V. Bollinger, K. W. Jacobsen and J. K. Nørskov, *Phys. Rev. B*, 2003, **67**, 085410.

108. R. Sander, *NIST Standard Reference Database Number 69.*

109. L. D. Chen, M. Urushihara, K. Chan and J. K. Nørskov, *ACS Catal.*, 2016, **6**, 7133-7139.

110. S. H. Rawal, W. C. McKee and Y. Xu, *Phys. Chem. Chem. Phys.*, 2017, **19**, 32626-32635.

111. A. A. Isse and A. Gennaro, *J. Phys. Chem. B*, 2010, **114**, 7894-7899.

112. A. V. Marenich, J. Ho, M. L. Coote, C. J. Cramer and D. G. Truhlar, *Phys. Chem. Chem. Phys.*, 2014, **16**, 15068-15106.

113. J. Ho and M. L. Coote, *Theor. Chem. Acc.*, 2009, **125**, 3.

114. W. M. Haynes, D. R. Lide and T. J. Bruno, *CRC handbook of chemistry and physics*, 2016, pp. 5–89.

115. D. M. Camaioni and C. A. Schwerdtfeger, *J. Phys. Chem. A*, 2005, **109**, 10795-10797.

116. L. T. Nielsen, K. H. Vase, M. Dong, F. Besenbacher, S. U. Pedersen and K. Daasbjerg, *J. Am. Chem. Soc.*, 2007, **129**, 1888-1889.

117. A. J. Bard and L. R. Faulkner, *Electrochemical Methods: Fundamentals and Applications, 2nd ed*, 2001.

118. C. Gómez-Anquela, M. Revenga-Parra, J. M. Abad, A. G. Marín, J. L. Pau, F. Pariente, J. Piqueras and E. Lorenzo, *Electrochim. Acta*, 2014, **116**, 59-68.

119. L. Laurentius, S. R. Stoyanov, S. Gusarov, A. Kovalenko, R. Du, G. P. Lopinski and M. T. McDermott, *ACS Nano*, 2011, **5**, 4219-4227.

120. S. Kesavan, A. Prabhakaran and S. A. John, *RSC Adv.*, 2014, **4**, 30896-30905.

121. M. P. Andersson, *J. Theor. Chem.*, 2013, **2013**, 9.

122. Y. Santiago-Rodríguez, J. A. Herron, M. C. Curet-Arana and M. Mavrikakis, *Surf. Sci.*, 2014, **627**, 57-69.

123. R. G. Acres, X. Cheng, K. Beranová, S. Bercha, T. Skála, V. Matolín, Y. Xu, K. C. Prince and N. Tsud, *Phys. Chem. Chem. Phys.*, 2018, **20**, 4688-4698.

124. D. Y. Petrovykh, H. Kimura-Suda, L. J. Whitman and M. J. Tarlov, *J. Am. Chem. Soc.*, 2003, **125**, 5219-5226.

125. D. N. Kelly, C. P. Schwartz, J. S. Uejio, A. M. Duffin, A. H. England and R. J. Saykally, *J. Chem. Phys.*, 2010, **133**, 101103.

126. Z. Peng, A. H. Holm, L. T. Nielsen, S. U. Pedersen and K. Daasbjerg, *Chem. Mater.*, 2008, **20**, 6068-6075.

127. M. Furukawa, T. Yamada, S. Katano, M. Kawai, H. Ogasawara and A. Nilsson, *Surf. Sci.*, 2007, **601**, 5433-5440.

128. N. Tsud, S. Bercha, K. Ševčíková, R. G. Acres, K. C. Prince and V. Matolín, *J. Chem. Phys.*, 2015, **143**, 174704.

129. S. Seifert, G. N. Gavrila, D. R. T. Zahn and W. Braun, *Surf. Sci.*, 2007, **601**, 2291-2296.

130. M. Hanus, M. Kabeláč, J. Rejnek, F. Ryjáček and P. Hobza, *J. Phys. Chem. B*, 2004, **108**, 2087-2097.

131. R. Otero, W. Xu, M. Lukas, R. E. A. Kelly, E. Lægsgaard, I. Stensgaard, J. Kjems, L. N. Kantorovich and F. Besenbacher, *Angew. Chem. Int. Ed.*, 2008, **47**, 9673-9676.

132. R. E. A. Kelly, W. Xu, M. Lukas, R. Otero, M. Mura, Y.-J. Lee, E. Lægsgaard, I. Stensgaard, L. N. Kantorovich and F. Besenbacher, *Small*, 2008, **4**, 1494-1500.

133. M. Lukas, R. E. A. Kelly, L. N. Kantorovich, R. Otero, W. Xu, E. Laegsgaard, I. Stensgaard and F. Besenbacher, *J. Chem. Phys.*, 2009, **130**, 024705.

134. P. A. Redhead, *Vacuum*, 1962, **12**, 203-211.

135. L. Kankate, A. Turchanin and A. Gölzhäuser, *Langmuir*, 2009, **25**, 10435-10438.

136. X. Torrelles, C. Vericat, M. E. Vela, M. H. Fonticelli, M. A. Daza Millone, R. Felici, T.-L. Lee, J. Zegenhagen, G. Muñoz, J. A. Martín-Gago and R. C. Salvarezza, *J. Phys. Chem. B*, 2006, **110**, 5586-5594.

137. F. Li, L. Tang, O. Voznyy, J. Gao and Q. Guo, *J. Chem. Phys.*, 2013, **138**, 194707.

138. J. Gao, F. Li and Q. Guo, *J. Phys. Chem. C*, 2013, **117**, 24985-24990.

139. P. Maksymovych and J. T. Yates, *J. Am. Chem. Soc.*, 2008, **130**, 7518-7519.

140. R. G. Bates and J. B. MacAskill, *Pure Appl. Chem.*, **50**, 1701–1706.

141. H. M. Badawi, *Spectrochim. Acta A Mol. Biomol. Spectrosc.*, 2011, **82**, 63-68.

142. G. Socrates, *Infrared and Raman characteristic group frequencies: Tables and charts*, 2004.

143. G. M. Marshall, F. Bensebaa and J. J. Dubowski, *J. Appl. Phys.*, 2009, **105**, 094310.

144. C. J. Houtman, N. F. Brown and M. A. Barteau, *J. Catal.*, 1994, **145**, 37-53.

145. A. R. Garcia, J. L. da Silva and L. M. Ilharco, *Surf. Sci.*, 1998, **415**, 183-193.

146. W. S. Sim, P. Gardner and D. A. King, *J. Phys. Chem.* , 1996, **100**, 12509-12516.

147. W. O. Gordon, Y. Xu, D. R. Mullins and S. H. Overbury, *Phys. Chem. Chem. Phys.*, 2009, **11**, 11171-11183.

148. F. C. Calaza, T.-L. Chen, D. R. Mullins, Y. Xu and S. H. Overbury, *Catal. Today*, 2015, **253**, 65-76.

149. M. Dunwell, Q. Lu, J. M. Heyes, J. Rosen, J. G. Chen, Y. Yan, F. Jiao and B. Xu, *J. Am. Chem. Soc.*, 2017, **139**, 3774-3783.

150. K. Arihara, F. Kitamura, T. Ohsaka and K. Tokuda, *J. Electroanal. Chem.*, 2001, **510**, 128-135.

151. Y. Yan, X. Ge, Z. Liu, J.-Y. Wang, J.-M. Lee and X. Wang, *Nanoscale*, 2013, **5**, 7768-7771.

152. N. Lopez, T. V. W. Janssens, B. S. Clausen, Y. Xu, M. Mavrikakis, T. Bligaard and J. K. Nørskov, *J. Catal.*, 2004, **223**, 232-235.

153. R. Meyer, C. Lemire, S. K. Shaikhutdinov and H. J. Freund, *Gold Bull.*, 2004, **37**, 72-124.

154. S. A. C. Carabineiro and B. E. Nieuwenhuys, *Gold Bull.*, 2009, **42**, 288-301.

155. Z. Zeng and J. Greeley, *Catal. Commun.*, 2014, **52**, 78-83.

156. H. Shin, Y. Ha and H. Kim, *J. Phys. Chem. Lett.*, 2016, **7**, 4124-4129.

157. N. Austin, S. Zhao, J. R. McKone, R. Jin and G. Mpourmpakis, *Catal. Sci. Technol.*, 2018, **8**, 3795-3805.

158. S. K. Shaikhutdinov, R. Meyer, M. Naschitzki, M. Bäumer and H. J. Freund, *Catal. Lett.*, 2003, **86**, 211-219.

159. W. C. McKee, M. C. Patterson, D. Huang, J. R. Frick, R. L. Kurtz, P. T. Sprunger, L. Liu and Y. Xu, *J. Phys. Chem. C*, 2016, **120**, 10909-10918.

160. D.-e. Jiang and S. Dai, *J. Phys. Chem. C*, 2009, **113**, 3763-3766.

161. P. Forzatti and L. Lietti, *Catal. Today*, 1999, **52**, 165-181.

162. J. J. Mortensen, B. Hammer and J. K. Nørskovi, *Surf. Sci.*, 1998, **414**, 315-329.

163. F. Abild-Pedersen, O. Lytken, J. Engbæk, G. Nielsen, I. Chorkendorff and J. K. Nørskov, *Surf. Sci.*, 2005, **590**, 127-137.

164. D. R. Alfonso, D. Kauffman and C. Matranga, *J. Chem. Phys.*, 2016, **144**, 184705.

165. S. Zhao, N. Austin, M. Li, Y. Song, S. D. House, S. Bernhard, J. C. Yang, G. Mpourmpakis and R. Jin, *ACS Catal.*, 2018, **8**, 4996-5001.

166. C. J. Barile, E. C. M. Tse, Y. Li, T. B. Sobyra, S. C. Zimmerman, A. Hosseini and A. A. Gewirth, *Nat. Mater.*, 2014, **13**, 619.

167. J. Wu, F. G. Risalvato, P. P. Sharma, P. J. Pellechia, F.-S. Ke and X.-D. Zhou, *J. Electrochem. Soc.*, 2013, **160**, F953-F957.

168. Z. Peng, Y. Chen, P. G. Bruce and Y. Xu, *Angew. Chem. Int. Ed.*, 2015, **54**, 8165-8168.

169. H. Niehus, *Surf. Sci.*, 1983, **130**, 41-49.

170. J. Tian, H. Cao, W. Wu, Q. Yu, N. P. Guisinger and Y. P. Chen, *Nano Lett.*, 2012, **12**, 3893-3899.

171. D. Heskett, A. Baddorf and E. W. Plummer, *Surf. Sci.*, 1988, **195**, 94-102.

172. S. Reiff and J. H. Block, *Surf. Sci.*, 1996, **345**, 281-289.

173. R. Raval, S. Haq, M. A. Harrison, G. Blyholder and D. A. King, *Chem. Phys. Lett.*, 1990, **167**, 391-398.

174. G. Henkelman, B. P. Uberuaga and H. Jónsson, *J. Chem. Phys.*, 2000, **113**, 9901-9904.

175. S. Smidstrup, A. Pedersen, K. Stokbro and H. Jónsson, *J. Chem. Phys.*, 2014, **140**, 214106.

176. Y. Fang and J. C. Flake, *J. Am. Chem. Soc.*, 2017, **139**, 3399-3405.

Vita

Xun Cheng was born in Tianjin, China. He graduated from Yaohua High School in Tianjin. He entered Nankai University where he received his Bachelor of Science degree. After graduation, he came to the U.S.. He received Master of Science degree in Chemical Engineering from Carnegie Mellon University. He entered the Department of Chemical Engineering at Louisiana State University to do theoretical research in the fields of surface science and electrochemistry. Upon completion of his doctoral degree, he would like to work in the field of renewable energy.